#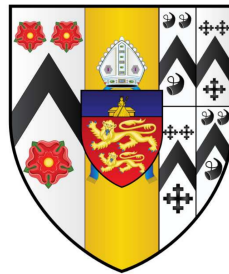 Magnetic Distortion Calibration for the LHCb Ring Imaging Cherenkov (RICH) Detector, and the Search for $\mathcal{CP}$ Violation in $\mathrm{D}^{*+} \to \mathrm{D}^0(\mathrm{K}^-\mathrm{K}^+)\pi^+$ Decays

Funai Xing
Brasenose College, University of Oxford

Thesis submitted in fulfilment of the requirements for the degree of MSc at the University of Oxford

Trinity Term, 2014

Abstract

The asymmetry under simultaneous charge and parity transformation ($\mathcal{CP}$ violation) has driven the understanding of electroweak interactions since its discovery in the kaon system. $\mathcal{CP}$ violation was subsequently discovered in the B system. Charmed mesons form the only heavy neutral meson system in which $\mathcal{CP}$ violation has yet to be observed unambiguously.

A study of indirect $\mathcal{CP}$ violation in D mesons through the determination of the parameter A_Γ is presented using a data sample of pp collisions, corresponding to an integrated luminosity of 37.7 pb^{-1}, collected with the LHCb detector and recorded at the centre-of-mass energy of 7 TeV at the LHC. The parameter A_Γ is the asymmetry of the effective lifetimes measured in decays of D^0 and $\overline{D}^0$ mesons to the $\mathcal{CP}$ eigenstates K^+K^-. A_Γ is sensitive to both the $\mathcal{CP}$ violation parameters $|q/p|$ and ϕ. Fits to the data sample yield $A_\Gamma(KK) = (0.39 \pm 0.55 \pm 0.24)\%$, where the first uncertainty is statistical and the second systematic. This result is consistent with no $\mathcal{CP}$ violation.

Critical for this analysis is the particle identification provided by the LHCb Ring Imaging Cherenkov (RICH) system. To ensure good performance, a proper calibration of the RICH photon detectors response is necessary. A system for the calibration of the magnetic distortion induced by the LHCb dipole magnet on the photon detectors is described. The system currently provides the calibration parameters used in the LHCb event reconstruction software and allows for a significant improvement in the overall particle identification performance.

Declaration

The work presented in Chapters 3 and 5 of this thesis has been carried out by the author, except when explicit references are made to other works. This thesis has not been submitted for another qualification to this or any other university.

"You know more than you think you know, just as you know less than you want to know."
– Oscar Wilde (1854-1900)

Acknowledgements

Contents

List of Figures

List of Tables

Chapter 1

Introduction

This thesis contains work carried out on the LHCb experiment in the years 2009-2011.

The first part of the thesis describes work on the calibration of the Ring Imaging CHerenkov (RICH-1) system. The particle identification provided by the LHCb RICH system is critical for many measurements. To ensure the integrity of the RICH data, a proper calibration of the RICH photon detectors response is necessary. A system for the calibration of the magnetic distortion induced by the LHCb dipole magnet on the photon detectors, MDCS, is described. Chapter 2 presents an overview of the LHCb detector. The MDCS hardware design, along with the software control and calibration algorithm, is presented in Chapter 3. The system currently provides the calibration parameters used in the LHCb event reconstruction software and allows for a significant improvement in the overall particle identification performance. The MDCS performance on collision data is presented at the end of Chapter 3.

The second part of the thesis presents a study of indirect $\mathcal{CP}$ violation in D mesons through the determination of the parameter A_Γ, using a data sample of pp collisions corresponding to an integrated luminosity of 37.7 pb^{-1}, collected with the LHCb detector and recorded at the centre-of-mass energy of 7 TeV at the LHC. The parameter A_Γ is the asymmetry of the effective lifetimes measured in decays of D^0 and $\bar{D}^0$ mesons to the $\mathcal{CP}$ eigenstates K^+K^-. The decay chain $D^{*+} \to D^0\pi^+$ is used as it provides the advantage of flavour tag-

ging for the D^0, through the sign of the pion and that the difference in the invariant mass of D^* and D^0 is a valuable background discriminating variable. A_Γ is sensitive to both the $\mathcal{CP}$ violation parameters $|q/p|$ and ϕ, which will be explained in detail in Chapter 4.

Chapter 5 presents a measurement of the D^0 $\mathcal{CP}$ violation parameter A_Γ. Trigger configurations were changed during the 2010 data taking to adapt to the running scenarios from the LHC. The LHC's increase in luminosity was achieved only with a limited number of bunches in the machine, which led to significant pileup different from the $n = 1$ scenario that was envisaged. It was decided that LHCb would record all the luminosity available, and this meant continual changes needed to be implemented into the trigger, in response to changing luminosity and beam configurations of the LHC. For this reason, the physics analysis presented in this thesis spans several trigger configurations. Each group of data taken under different trigger configurations was analysed individually.

A summary and outlook is presented in Chapter 6.

Chapter 2

LHCb Detector

2.1   The Large Hadron Collider

The Large Hadron Collider (LHC) is a superconducting proton-proton accelerator and collider installed in a 26.7 km underground tunnel at CERN. The goal of the LHC is to search for the missing components in the Standard Model (SM) and to probe physics beyond the SM. The key physics spans from searching for the Higgs particle, Supersymmetry (SUSY) and dark matter, to explaining the asymmetry between matter and anti-matter.

The LHC consists of two rings of counter-rotating beams travelling in ultra-high vacuum, to minimise the amount of gas present and avoid collisions with gas molecules in the beam. It is designed to provide pp collisions at centre-of-mass energies of up to 14 TeV. Radio frequency (RF) cavities and electric fields are used to provide particle acceleration to this unprecedented high energy [1].

The proton beams are guided around the accelerator ring by a strong magnetic field, achieved using superconducting electromagnets. This requires cooling the magnets to about -271° - a temperature colder than that of outer space. For this reason, much of the accelerator is connected to a distribution system of liquid helium which cools the magnets, as well as to other supply services. Thousands of magnets of different varieties and sizes are used to direct

CROSS SECTION OF LHC DIPOLE
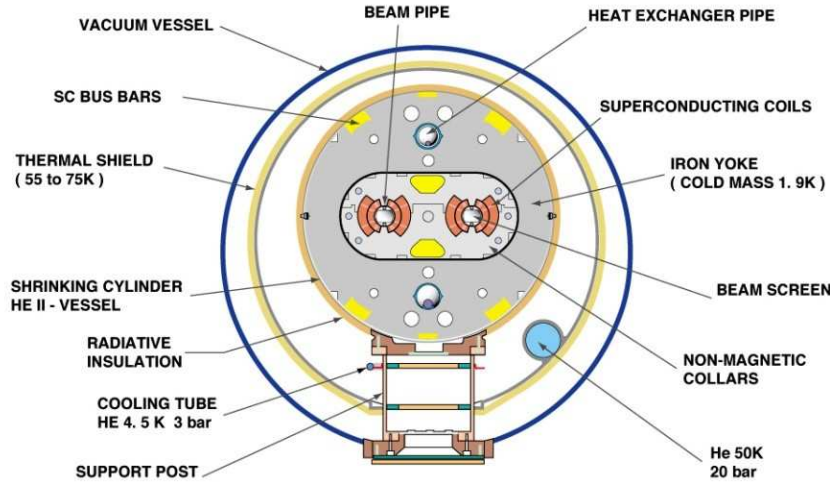
Figure 2.1:   LHC dipole cross section.

the beams around the accelerator. These include 1,232 dipole magnets (Figure 2.1) of 15 m length which are used to bend the beams, and 392 quadrupole magnets, each 5-7 m long, to focus the beams. Immediately prior to collision, quadrupole triplets (series of quadrupoles) are used to squeeze the particles closer together to increase the chances of collisions.

The nominal luminosity of the LHC is $L = 10^{34}\text{cm}^{-2}\text{s}^{-1}$, which requires 2,808 bunches in each proton beam, with a bunch spacing of 25 ns. In 2010, the first year of operation, the LHC began providing particle beams at a centre-of-mass energy of 450 GeV. Towards the end of the year, the collision energy gradually increased to 7 TeV, or half of the nominal energy. With 344 colliding bunches, the maximum instantaneous luminosity recorded in LHCb was $L = 170 \times 10^{30}\text{cm}^{-2}\text{s}^{-1}$. Figure 2.2 shows the evolution of integrated luminosity at LHCb over time during 2010 data taking.

CERN's accelerator complex is a succession of particle accelerators that can reach increasingly higher energies. (Figure 2.3) Each accelerator boosts the energy of a beam of particles, before injecting it into the next one in the sequence. Protons are obtained by removing electrons from hydrogen atoms. They are injected from the linear accelerator (LINAC) into the
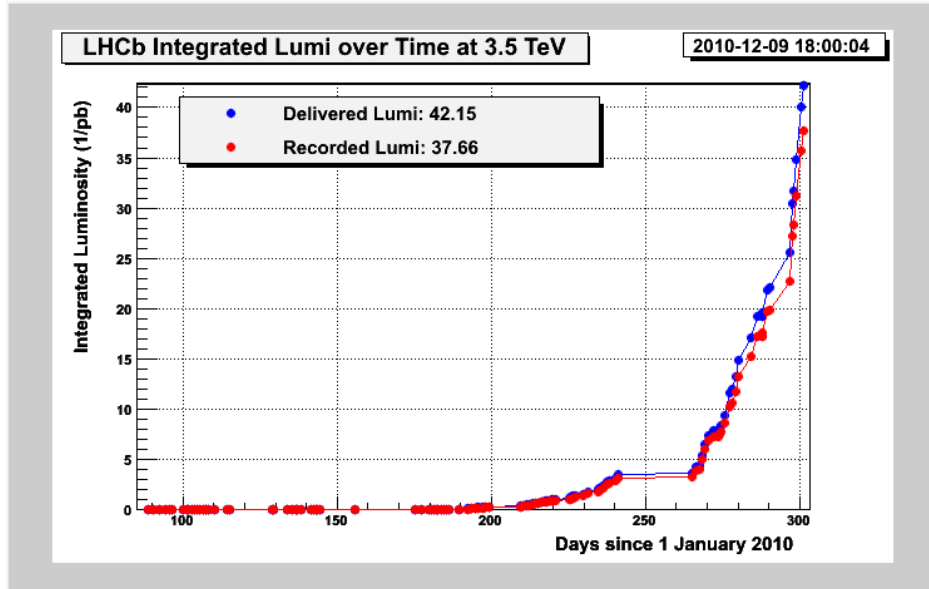
Figure 2.2: Delivered and recorded integrated luminosities at LHCb during 2010.

PS Booster, then the Proton Synchrotron (PS), followed by the Super Proton Synchrotron (SPS), before finally reaching the Large Hadron Collider (LHC). Protons will circulate in the LHC for 20 minutes before reaching the maximum speed and energy.

There are four major particle physics experiments at the LHC. The two large experiments, ATLAS and CMS, are based on general-purpose detectors to analyse the myriad of particles produced by the collisions in the accelerator. They are designed to investigate the largest range of physics possible, with emphasis on Higgs boson studies and the searches for Supersymmetry elements. Having two independently designed detectors is vital for cross-confirmation of any new discoveries made. The other two experiments, ALICE and LHCb, are specialised detectors for analysing the LHC collisions in relation to specific phenomena. Alice is a dedicated heavy-ion collision experiment, while LHCb is designed for heavy flavour physics studies.

2.2 LHCb Design

With the large $b\bar{b}$ and $c\bar{c}$ production cross section at 288 μb [2] and 1415 μb [3] at 7 TeV, the LHC is the most abundant source of B and D hadrons ever produced in the world.
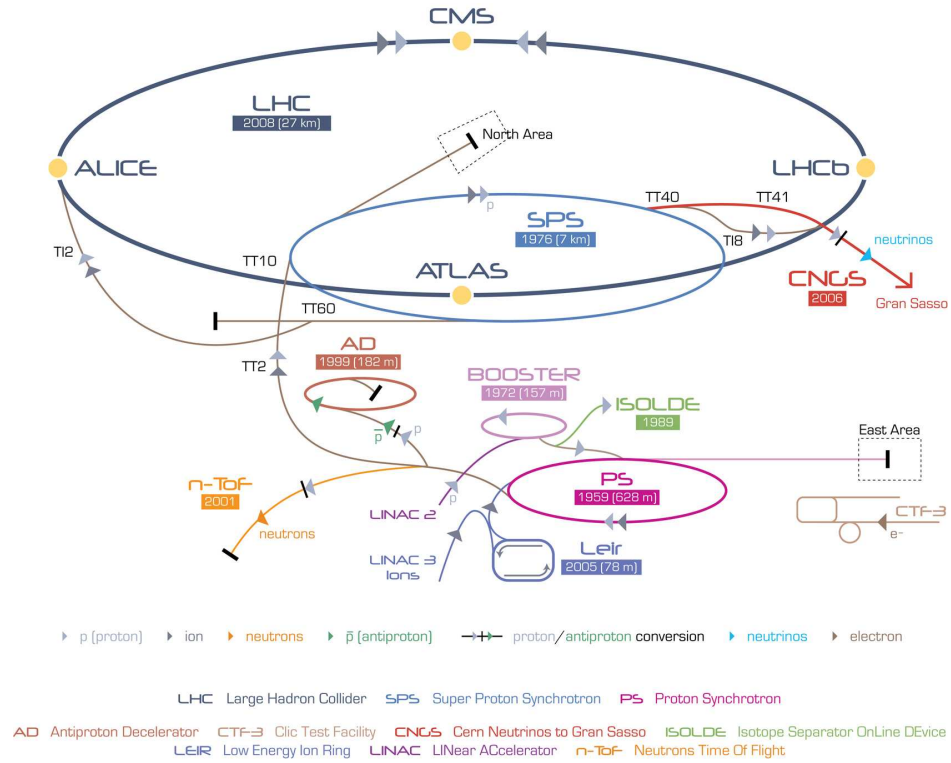
Figure 2.3:   LHC accelerator complex.

Compared with the e^+e^- B-factories, LHC can produce much heavier B mesons such as the B_s^0 and B_c^+, as well as B baryons, which allows for a very diverse physics programme. LHCb aims to search for evidence of new physics through precise measurements in the flavour sector. Measurements of particular importance are as follows:

1. Measuring $\mathcal{CP}$-violation in the interference between decay and mixing of $B_s^0 \to J/\Psi\phi$;

2. Searching for the very rare decay $B_s^0 \to \mu^+\mu^-$;

3. Measuring the angular distributions in the decay $B_d^0 \to K^*\mu^+\mu^-$;

4. Precision measurement of γ angle in both tree and loop processes. This involves the reconstruction of channels such as $B^+ \to D^0K^+$ and $B_s^0 \to hh'(h, h' = \pi, K)$ respectively;

5. Photon polarisation measurements in $B_s^0 \to \phi\gamma$ and $B_s^0 \to K^*\gamma$;

6. Mixing and $\mathcal{CP}$-violation measurements in the D-meson system.
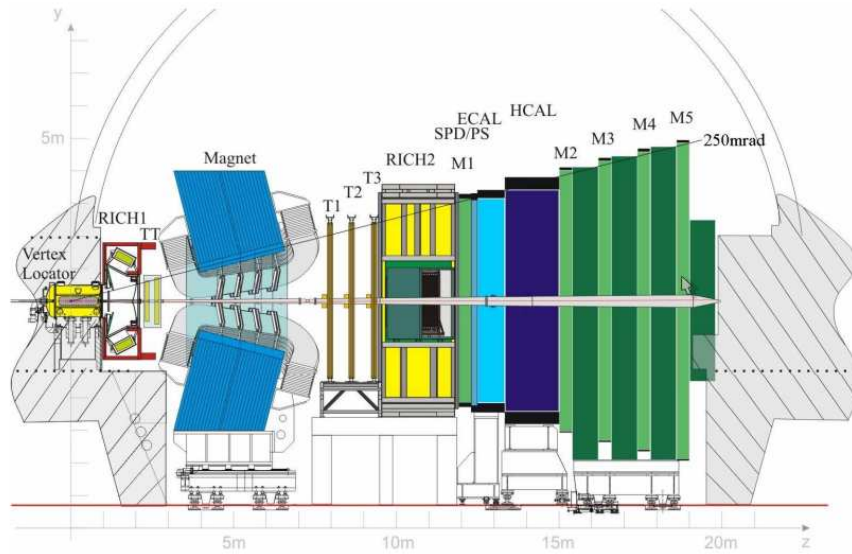
Figure 2.4: LHCb detector layout.

In order for LHCb to exploit this large number of b- and c-hadrons requires an efficient, robust and flexible trigger which can cope with the harsh hadronic environment. The trigger system must be efficient to many different final states. Excellent vertex and momentum resolution are essential for the good proper-time resolution necessary to study the rapidly oscillating B_s^0 meson systems and also for the good invariant mass resolution. Separation between pions, kaons and protons is crucial to reconstruct the different final states of b- and c-hadron decays correctly. Some physics channels also require excellent electron, muon, and photon identification. Finally, a data acquisition system with high bandwidth and powerful online data processing capability is essential for optimum data taking.

To accommodate the physics requirements above, the LHCb detector consists of a vertex detector (VELO), a dipole magnet, two Ring Imaging Cherenkov detectors (RICH), a tracking system, a calorimeter system and a muon detector, as illustrated in Figure 2.4.

LHCb is a single-arm spectrometer with angular coverage from 10 mrad to 300 (250) mrad in the bending (non-bending) plane. This geometry is chosen because at high energies $b\bar{b}$ pair production will be boosted along the same direction, at small angles with respect to the beam line.
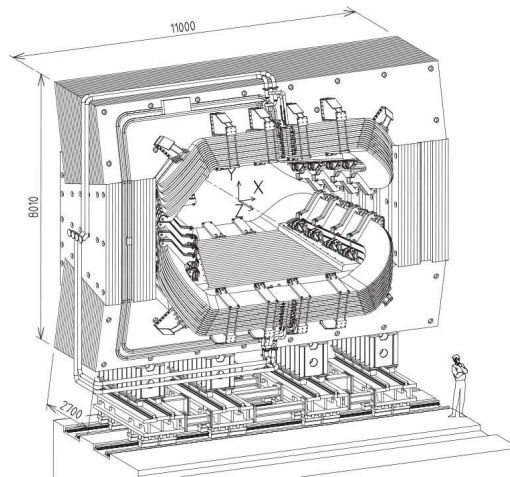
Figure 2.5: LHCb magnet, viewed from downstream of the interaction point.

2.3   Magnet

The LHCb detector is designed around a dipole magnet [4], which is used to measure the momentum of charge particles via the bending of the charged tracks. The dipole magnet is placed close to the interaction region in order to minimise its dimension, as well as exerting a strong bending power. The magnet is located behind VELO and RICH 1, with the intention to keep the VELO in a region of low magnetic field for fast track fitting in the trigger. The design also takes into account that the RICH 1 detector has to operate in a region of low magnetic field.

A conventional magnet is chosen, designed to provide an integrated magnetic field of 4 Tm for tracks of 10 m length. A diagram may be seen in Figure 2.5. The field is oriented vertically, with a maximum value of 1.1 T. The polarity of the field can be flipped periodically to reduce systematic errors in any measurements that could result from detector asymmetry. An iron shielding is placed upstream of the magnet, to reduces the unwanted field in the vicinity of the VELO and of RICH1.

2.4   VELO

Good tracking measurements are essential for the reconstruction of decay vertices, particle momentum and invariant mass. The vertex locator (VELO) [5] is the first element of the LHCb tracking system and it closely surrounds the interaction point.

The proper time of the b- or c-hadron is a necessary observable quantity in many heavy flavour measurements, such as time-dependent analyses of $\mathcal{CP}$ violation, as well as being an interesting measurement in its own right. B and D physics require the precise reconstruction of both the primary (production) and secondary (decay) vertices, which allows the proper time of the B and D hadrons to be reconstructed. The vertex resolution and the impact parameter, that is the distance of the closest approach of a particle to the primary vertex, of a track is determined by the VELO.

The VELO is shown in Figure 2.7. It consists of 21 tracking stations each with 2 layers of half-circle silicon detectors. Each sensor has a minimum radius of 8 mm and an azimuthal coverage of 182 degrees, giving a small overlap between the two halves for alignment purposes. Each semi-circular silicon plane is made up of two 220 μm thick silicon microstrip sensors. One disc has semi-annular strips to measure the radial distance from the beam axis and the other has radial strips to measure the azimuthal angle. The former is referred to as an "r sensor" and the latter a "ϕ sensor", as shown in Figure 2.6.

The layout of the detector is chosen to provide the best resolution for those hits closest to the interaction point and a uniformly low occupancy of 1% across the sensor. The r sensor has four 45 degree sections in ϕ, each consisting of 512 concentric circular strips. The strip pitch is 40 μm at the inner 8mm radius and increases to 100 μm at the outer 42 mm radius. The ϕ sensor is divided into an inner and outer region of 683 and 1365 radial strips respectively, with a strip pitch that varies from 36 μm at the innermost regions to 100 μm at the outer radii. The r-ϕ geometry is particularly well suited for the trigger system, since high impact parameter tracks can be easily identified using just the r sensors alone, thereby saving valuable computational time.
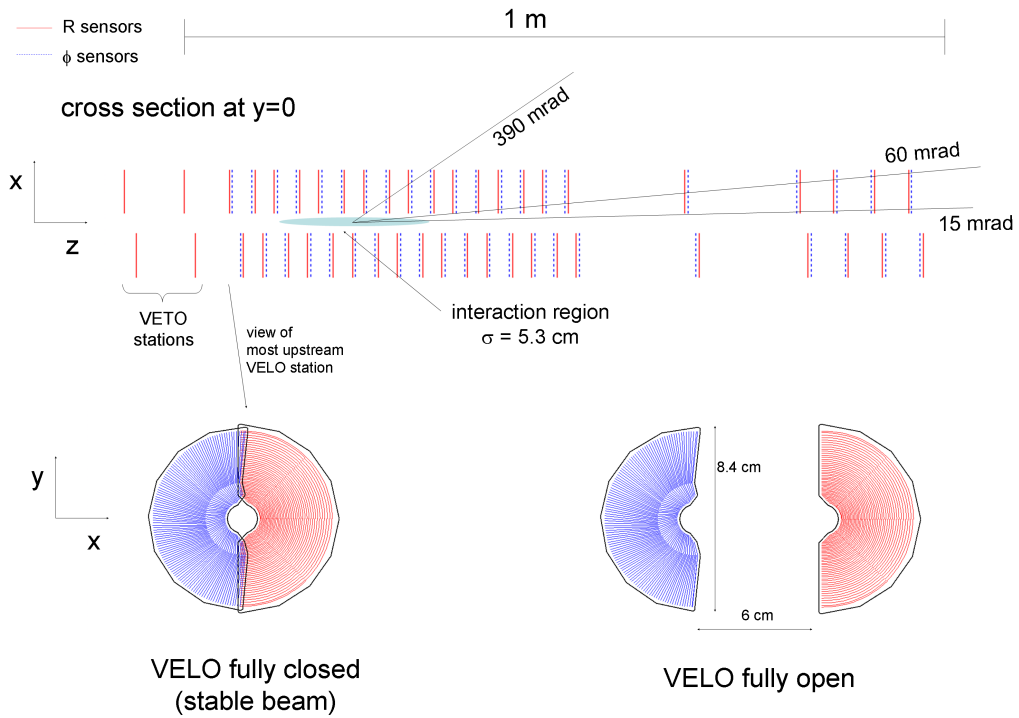
Figure 2.6: VELO sensors. Each semi-circular silicon plane is made up of two silicon microstrip sensors. One disc to measure the radial distance from the beam axis (r sensor)and the other to measure the azimuthal angle (ϕ sensor).
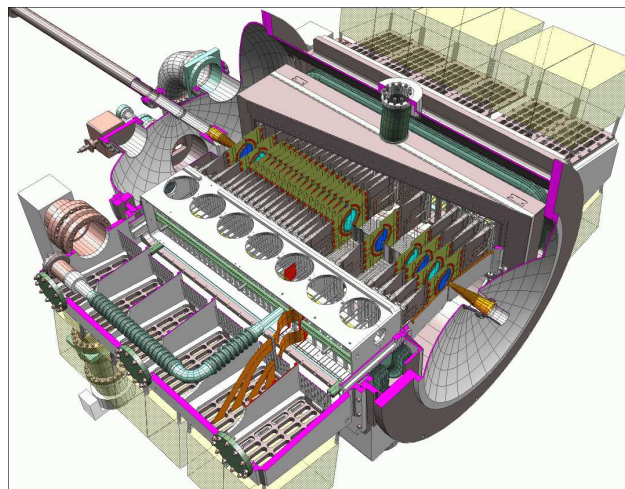
Figure 2.7: VELO layout. The sensors can be seen inside the vacuum chamber.
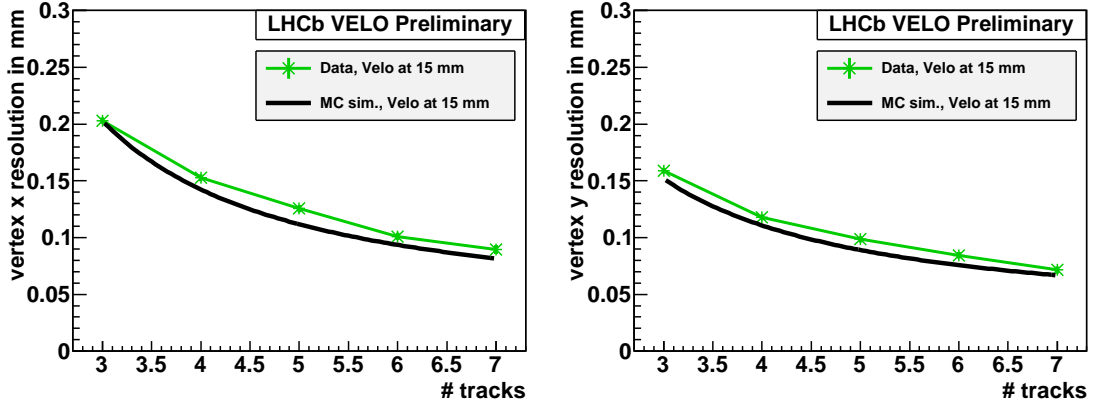
Figure 2.8: VELO vertex resolution. The results from data show good agreement with Monte-Carlo simulations.

The VELO primary vacuum system, along with the LHCb beam pipe, is designed as part of the LHC vacuum. The silicon sensors and readout electronics are separated from the LHC vacuum by a 300 μm thick aluminium alloy foil. The foil protects the LHC vacuum from mechanical failures of the VELO detector and protects the sensors from the RF currents induced by the beam. The foil has a corrugated design to minimise the material traversed by particles and to dissipate the induced RF currents.

The designed primary vertex resolution is 42 μm in the z direction, 10 μm in the x-y plane (Figure 2.8). The precision on decay lengths ranges from 220 μm to 375 μm, which leads to a typical proper time resolution of 40 fs in a typical B or D meson decay channel.

The impact parameter resolution in the x-y plane is shown in Figure 2.9. As can be seen the discrepancy between data and MC simulation is larger at the low P_T range. This is primarily due to an imperfect description of the material, particularly in the RF foil, in the MC simulations.

2.5 Tracking Stations

The tracking system, consisting of the Trigger Tracker (TT) and tracking stations T1-T3, is designed to measure charged particle tracks in the region between VELO and the calorimeters and hence determine their momenta, also allowing association with muon chamber hits,
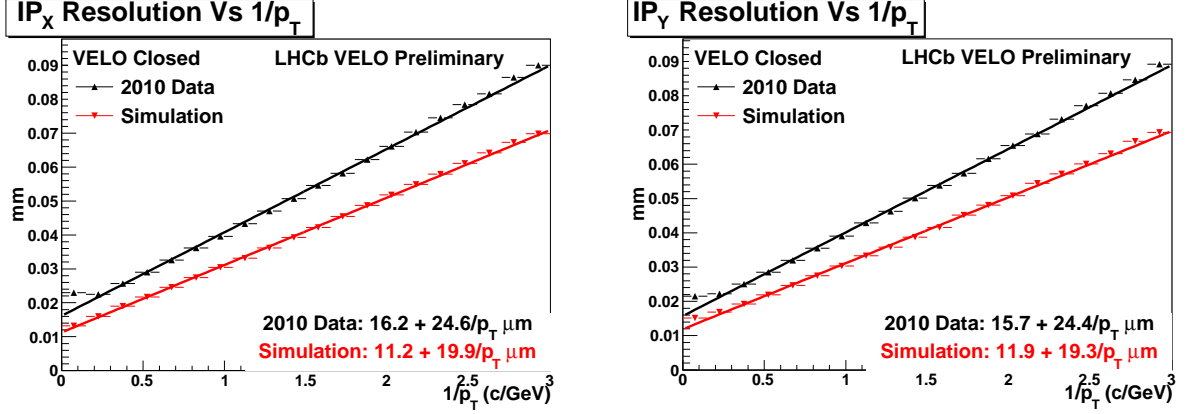
Figure 2.9: VELO impact parameter resolution. Data and simulation discrepancy due to imperfect material description in simulation.

calorimeter clusters and downstream RICH rings. The TT is so named because it was once planned to contribute to the trigger decisions but does not take part in the trigger in the actual running.

The TT is placed in front of the magnet and directly behind RICH 1. It consists of four planes of silicon strip detectors. The three stations T1-T3 are located downstream of the magnet. They are further divided into an Inner Tracker (IT) [6] with small channel pitch that covers the regions closest to the beam-pipe, and a coarser grained Outer Tracker (OT) [7] that covers most of the acceptance where particle fluxes are relatively lower. Every IT station consists of four layers, each rotated at 5 degrees with respect to each other. The layers are covered by silicon micro-strip detectors. The OT is a gas-filled straw tubes detector. Each station consists of four layers that are made of modules housing two staggered monolayers of 64 tubes each.

Combined with the VELO, the Tracking System provides a resolution on secondary vertices of $\sigma_z \sim 170 \mu m$, a resolution on proper time σ_t at around 40 fs and a momentum resolution less than 0.5% for particles with momenta up to 200 GeV/c. This performance leads to a typical B/D mass resolution better than 15 MeV/c^2 for decays into charged particle final states.
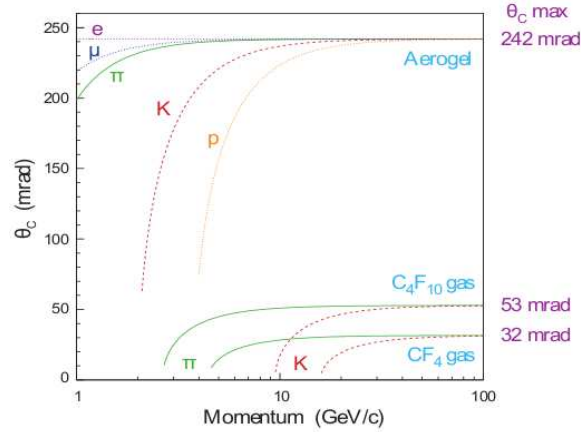
Figure 2.10:   Effective momentum range of the radiators.

2.6   RICH

Hadron identification in LHCb is achieved by the use of Ring Imaging Cherenkov (RICH) detectors [8]. The ability to distinguish between pions, kaons and protons in a variety of final states is crucial for the physics programme of the LHCb experiment.

With Cherenkov detectors it is possible to measure the particle velocity β using Cherenkov radiation. With this information, it is then possible to determine the particle mass combining β with knowledge of the particle momentum from the tracking systems.

The two RICH detectors provide particle identification over the wide momentum range 2-100 GeV/c. Three radiators each with different refractive indices are chosen: silica aerogel for the lowest momentum tracks, while the intermediate region of the spectrum of 10-60 GeV/c is well matched to gaseous C_4F_{10}. For the highest momentum tracks, gaseous CF_4 is used (Figure 2.10).

RICH1 is designed to provide particle identification over the momentum range 2-60 GeV/c. It combines aerogel and C_4F_{10} radiators to cover the full outer acceptance of the detector up to 300 (250) mrad in the horizontal (vertical) plane. It is located between the VELO system and the TT, before the magnet. The inner acceptance of 25 mrad is defined by the beam pipe. The layout of RICH 1 is illustrated in Figure 2.11.
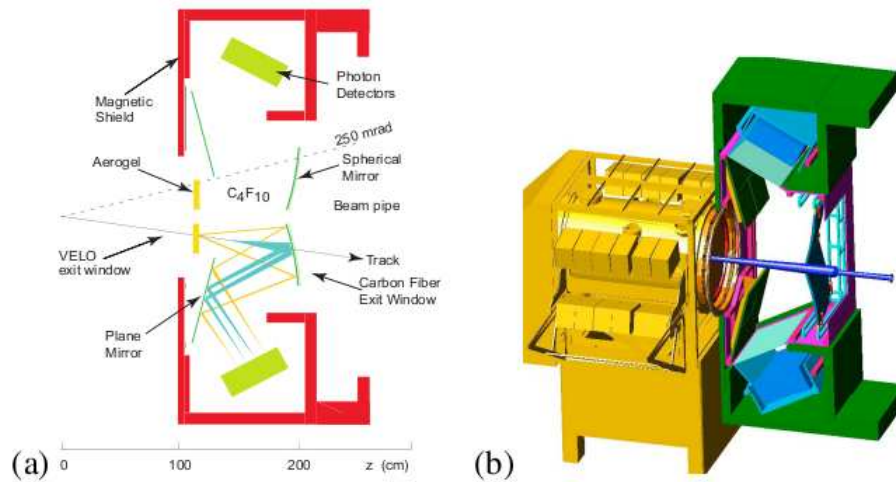
Figure 2.11: (a) RICH 1 internal layout. (b) The position of RICH 1 detector (green) with respect to VELO (yellow).

The Cherenkov photons emitted along the trajectories of the particles are focused by an array of spherical mirrors. The tilting of the mirrors allows the Cherenkov photons to be focused outside the spectrometer acceptance, thus reducing the materials within the acceptance and minimising the degradation of the tracking performance. The focusing spherical mirrors are followed by an array of flat mirrors. These flat mirrors are used to reflect Cherenkov rings outside the LHCb acceptance where they are collected by photodetectors.

RICH2 is placed between the last tracking station and the first muon station and it uses low refractive index gaseous CF_4 as Cherenkov radiator. This detector is suitable for high momentum particle identification.

RICH2 has a reduced angular acceptance, limited to 120 mrad and to 100 mrad in the horizontal and vertical plane respectively. It provides particle identification up to 100 GeV/c. The optical geometry configuration of RICH 2 is similar to the one adopted in RICH 1, but it is horizontally symmetrical. Each of the spherical mirror matrices is composed by 21 hexagonal and 7 half hexagonal 6 mm thick glass mirrors, and it is tilted by 390 mrad horizontally with respect to the beamline. The radius of curvature is 8,600 mm. To cover one half of the flat mirror surface, 20 rectangular 6 mm thick glass mirror segments each of 410×380 mm^2 are used. Each array is tilted by 185 mrad horizontally. The two photon
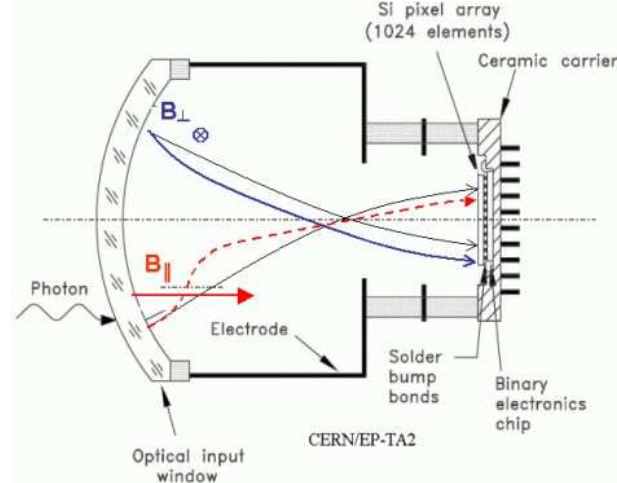
Figure 2.12: Internal structure of an HPD, showing the cross-focusing effect of the photo-electron trajectories.

detector matrices are placed inside the magnetic shielding boxes.

2.6.1 Photodetectors

The baseline photodetector technology selected for the LHCb RICH is the pixel Hybrid Photon Detector (HPD) which uses a silicon detector anode inside the vacuum envelope, with a quartz window in the front [8]. Photoelectrons released by photons incident on the photocathode are accelerated onto the silicon sensor by an applied high voltage of 20 kV, resulting in a signal of 5,000 e in the silicon. It is based on an image intensifier technology, employing electrostatic cross-focussing to accelerate and image photoelectrons from the photocathode onto the anode, demagnifying by a factor of 5, in the process of cross-focussing as illustrated in Figure 2.12. The anode assembly comprises a segmented silicon pixel sensor which is bump-bonded to a pixel readout chip.

The HPD imaging quality is degraded by an external magnetic field, which causes the photoelectron trajectory to bend. An overall magnetic shield is used together with individual tube made from high magnetic permeability alloy surrounding each individual HPD. The residual distortions can be corrected with a dedicated calibration system, Magnetic Distortion Calibration System (MDCS) and it will be described in details in Chapter 3.
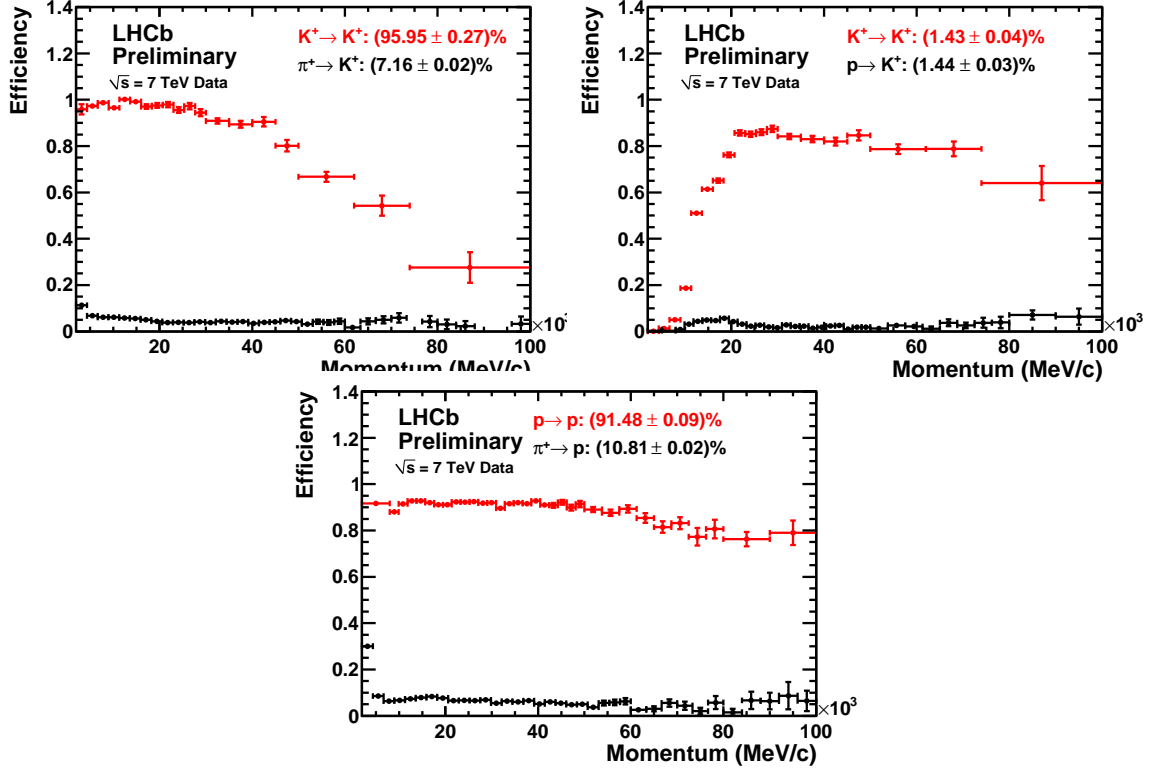
Figure 2.13: RICH PID performance from collision data. The kaon identification and $\pi \to K$ mis-ID rate is shown in top left. The top right plot shows the equivalent curve for kaon identification efficiency versus $p \to K$ mis-ID, and the bottom plot shows proton identification and $\pi \to p$ mis-ID.

2.6.2 Performance

The RICH PID performance from 2010 data is illustrated in Fig. 2.13. These results are for a particular cut on the log likelihood information from the RICH pattern recognition. A tighter cut can be used to suppress the mis-ID rate to a lower level. These plots show that the RICH system already has excellent performance over the typical track momentum range of the B and D meson decays, from 2 to 100 GeV/c. Though the performance is very good, it is not yet at the level found in the Monte Carlo (MC) simulation. Improvements are underway in terms of mirror alignment and calibration of the radiator refractive indices.

2.7 Calorimeters and Muon System

The analysis presented in this thesis does not make significant offline use of these sub-detectors, although they are important for the earliest level of triggering. Therefore only a brief description is given here. More information may be found in [9].

2.7.1 Calorimeters

The calorimeter system [10] reconstructs the energy deposited in electromagnetic and hadronic showers, allows for the identification of electrons, photon and π^0, and provides important input to the earliest level of the trigger.

The system consists of a single-layer scintillator pad detector (SPD), followed by a single-layer preshower (PS), an electromagnetic calorimeter (ECAL) and an hadronic calorimeter (HCAL).

The SPD distinguishes charged particles from neutral ones, which are the main source of background to the electron trigger. It consists of 15 mm thick scintillator pads arranged in a matrix-like layer.

The PS is designed for the detection of early shower developments from electromagnetic particles and is also useful in $e - \pi$ discrimination. It consists of cells made up from 14 mm-thick lead plates followed by squared scintillators 10 mm thick. The transverse dimensions are 4, 8 or 16 cm, which matches the ECAL segmentation.

The ECAL identifies electrons, photons and π^0s, and measure their energy. It is constructed of 70 layers consisting of 2 mm thick lead plates and 4 mm-thick polystyrene based scintillator plates. Its length corresponds to 25 X_0 and has a resolution of $\sigma(E)/E = 10\%\sqrt{E} \oplus 1.5\%$, with E in GeV.

The HCAL is constructed from scintillator tiles embedded in an iron structure. This provides 7.3 λ_I and a resolution $\sigma(E)/E = 80\%\sqrt{E} \oplus 10\%$. Photomultiplier tubes (PMTs) are used for the light detection.

2.7.2 Muon System

The muon system [11] provides muon identification as well as inputs for the L0 trigger on high-p_T muon candidates. It consists of one station (M1) located in front of the calorimeters and four stations (M2-M5) located downstream the HCAL, embedded in an muon filter made of four 80 cm thick iron walls, for a total thickness of 320 cm, corresponding to 20 λ_I. The total area is about 435 m^2 and the acceptance angle from 15 to 300 mrad leads to a geometrical acceptance for muons coming from B meson decays of about 20%.

Each muon station has two detector layers with independent readout. Due to the large variation in particle flux depending on the distance to the LHC beam pipe, each station is divided in four regions characterised by different readout channel coarseness. Except for the innermost region of M1, all are multi-wire proportional chambers (MWPCs) filled with a mixture of $Ar/CO_2/CF_4$ (40 : 50 : 10). MWPCs have a response time under 25 ns, allowing hits to be unambiguously assigned to their corresponding bunch crossing. For the innermost region of M1, where particle rate exceeds the MWPCs capabilities, gas-filled pad detectors using Gas Electron Multiplier (GEM) foils are used.

The muon system allows the p_T to be measured for muon L0 trigger with a resolution of 20%. Muons with momentum down to 3 GeV/c are identified with an efficiency in excess of 90% (Figure 2.14), while keeping the pion misidentification probability below 1.5% (Figure 2.15).

2.8 Trigger

2.8.1 Original Design

The LHC beam crossing rate is 40 MHz, of which visible pp interactions in LHCb design condition is 10 MHz. That has to be reduced by a factor of 50,000 to 2 KHz before being written to tape for offline analysis. This is achieved by utilising two layers of triggers: the Level-0 (hardware) and the High Level Trigger (HLT, software). (Figure 2.16)
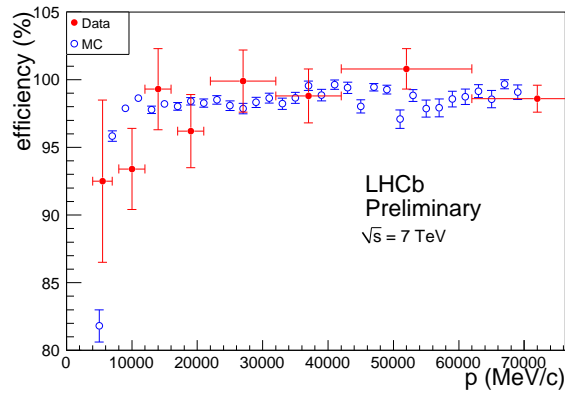
Figure 2.14: Muon ID efficiency using $J/\psi \to \mu^- \mu^+$, over a momentum span of around 5-70 GeV/c. Data and MC are shown in filled and empty circles, respectively.
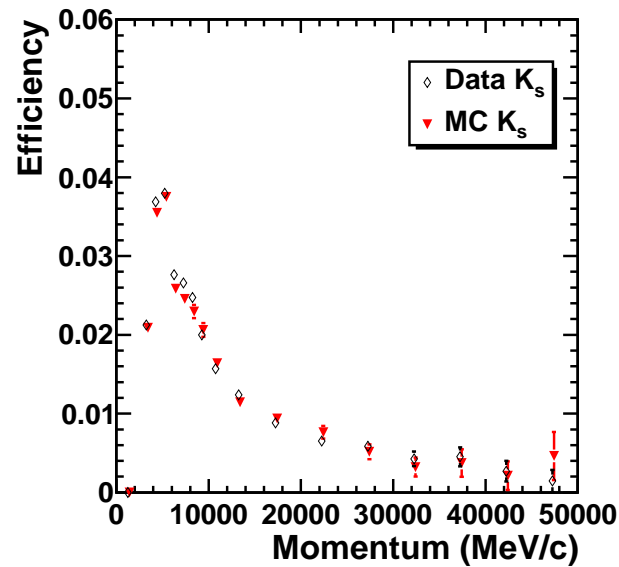
Figure 2.15: $\pi - \mu$ mis-ID rate, with data in empty circle and MC in filled shape.
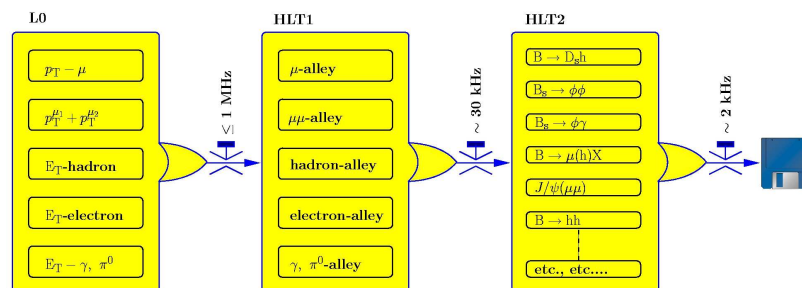
Figure 2.16: Trigger decision flow chart.

The main requirement of the trigger [12] is to retain high signal efficiency for the offline selections, while significantly reducing the data rates. At nominal LHCb luminosity the rate of $b\bar{b}$ pairs produced is around 100 kHz, of which only 15% will have at least one B-meson with its complete decay cone within the LHCb acceptance. The typical branching ratios for B-meson decays in $\mathcal{CP}$-violation studies is less than 10^{-3}.

The Level-0 trigger reduces the event rate from 10 MHz to 1 MHz, at which all the sub-systems are able to contribute to a trigger decision. A typical signature of the B-meson decays is the high transverse momentum p_T (typically a few GeV) of the decay daughters w.r.t that of particles produced in light quark events, due to the high rest mass of the b-quark.

The Level-0 trigger utilise this property to reconstruct the highest p_T hadron, e/γ clusters in the calorimeters, and highest p_T muons in the muon chambers. The final decision is made by Level-0 Decision Unites (L0DU), which collect information from all components from triggering sub-systems.

The HLT is the second and last level of trigger in LHCb, which runs on events passing the L0 trigger. Unlike in Level-0, the HLT output rate is not limited by hardware design. It has access to data from all sub-detectors and is able to use the final quality information from the tracking systems. The HLT is further divided into 2 levels: HLT1 and HLT2.

HLT1 reduces the rate from the 1 MHz output of L0 to a few KHz. It applies different "alleys" (i.e. parallel sequences of algorithms) according to the type of candidate on which the L0 decision was taken. Due to the limited CPU power available, HLT1 uses only part of the full information available. The first task of the alleys is to confirm the L0 candidates with better resolution by adding information from at least one tracking sub-detector, i.e. the VELO and the tracking station. After the L0 confirmation, the trigger decision is then taken based on the p_T and impact parameter (IP) of the confirmed candidate.

HLT2 further reduces the 10kHz rate down to around 2 kHz, at which the data is written to storage for offline analysis. Global event reconstruction and selections are performed in HLT2. The combined HLT1 alleys output rate is sufficiently low to allow a track reconstruc-
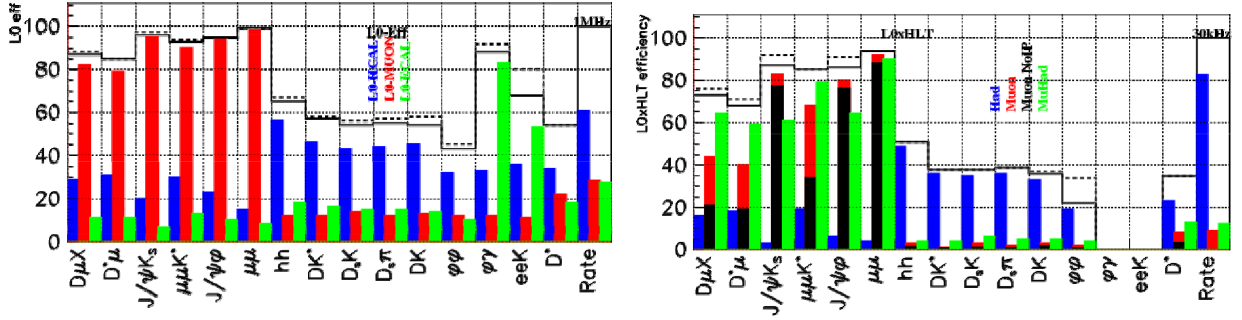
Figure 2.17: Example of L0×HLT1 trigger performance on various physics channels.

tion equal to that performed offline. The only difference is that the former is without Kalman filter, which provides a full covariance matrix, due to CPU processing power limitation in the HLT. Previous trigger stages do not use cuts on invariant mass, nor precise pointing cuts to a primary vertex (PV). Those cuts are applied in the HLT2 inclusive and exclusive selections. The exclusive triggers are more sensitive to tracking performance, while the inclusive triggers reduce the need on having to reconstruct all particles. On the other hand, the exclusive selections produce a smaller output rate, allowing for a more relaxed values for the selection cuts. The final trigger is a logical OR between all the inclusive and exclusive selections. The performance of the Level-0 and HLT1 triggers, based on Monte-Carlo study, is illustrated in Figure 2.17.

The trigger is configured using a unique hexadecimal Trigger Configuration Key (TCK); for example, setting 0x002e002a was used in 2010. The TCK setting defines the sequence of lines included in the trigger and what thresholds and selection criteria are used for each line. It is therefore possible to pinpoint exact trigger conditions for individual events in data and to reproduce the trigger on Monte-Carlo simulated events.

2.8.2 Actual Setup in 2010 Data Taking

Trigger configurations were changed during the 2010 data taking to adapt to the running scenarios from the LHC. The LHC's increase in luminosity was achieved only with a limited number of bunches in the machine, which led to significant pileup different from the $n = 1$

(i.e. one collision per bunch crossing) scenario as envisaged. It was decided that LHCb would record all the luminosity available, and this meant continual changes needed to be implemented into the trigger. For this reason, the physics analysis presented in this thesis spans several trigger configurations.

In early 2010, the HLT1 trigger consisted of an L0 decision confirmation step, This then evolved into a different strategy later in the year when the majority of the integrated luminosity was recorded. This updated HLT1 trigger is a set of inclusive trigger "lines" whose decisions were combined in a logical OR to give the final HLT1 decision. There are approximately 20 lines, of which about 15 are intended for use in physics analysis. Each of the trigger lines used in physics analysis required the presence of one or two tracks (single or dimuons, single electrons, single hadrons) which fulfilled certain criteria, for example high transverse momentum and good χ^2 per degree of freedom for the track fit. HLT1 has a maximum output rate of 40 kHz.

At the HLT2 stage, there are more lines each triggering on the presence of an inclusive decay signature or exclusive c- and b-hadron candidates. In each line, reconstruction and selection of the signature or candidate is performed in as similar a way as possible to that performed on the fully reconstructed data.

2.9   Online System

The LHCb Online system [13] consists of three components:

- Data Acquisition (DAQ) system,

- Timing and Fast Control (TFC) system,

- Experiment Control System (ECS).

2.9.1 Data Acquisition System

The purpose of the Data Acquisition (DAQ) system is the transport of the data belonging to a given bunch crossing, as identified by the trigger, from the detector front-end electronics to permanent storage.

Data from the on- or near-detector electronics (front-end electronics) are collected in LHCb-wide standardised readout boards (TELL1).

In the CPU farm, the HLT algorithm selects interesting interactions; upon a positive decision, the data are subsequently sent to permanent storage. The HLT is expected to reduce the overall rate from the original trigger rate of 1MHz to 2 kHz, hence by a factor of 500. The storage system is expected to have an initial capacity of ~ 40 TB, which should offer sufficient buffer space to cope with possible interruptions of the transfer to permanent storage at CERN.

2.9.2 Timing and Fast Control

The TFC system drives all stages of the data readout of the LHCb detector between the front-end electronics and the online processing farm by distributing the beam-synchronous clock, the L0 trigger, synchronous resets and fast control commands. The system is a combination of electronic components common to all LHC experiments and LHCb custom electronics. The TFC architecture can be described in terms of three main ingredients, the TFC distribution network, the trigger throttle network, and the TFC master (Readout Supervisor).

The heart of the system, the Readout Supervisor, implements the interface between the LHCb trigger system and the readout chain. The Readout Supervisor synchronizes trigger decisions and beam-synchronous commands to the LHC clock and orbit signal provided by the LHC. It is also capable of producing a variety of auto-triggers for sub-detector calibration and tests, and performs the trigger control as a function of the load on the readout system. In order to perform dynamic load balancing among the nodes in the online processing farm,

the Readout Supervisor also selects and broadcasts the destination for the next set of events to the Readout Boards based on a credit scheme in which the farm nodes send data requests directly to the Readout Supervisor.

For each trigger the Readout Supervisor transmits a data bank over the readout network which is appended to the event data and which contains the identifier of the event, the time and the source of the trigger.

2.9.3 Experiment Control System

The Experiment Control System (ECS) ensures the control and monitoring of the operational state of the entire LHCb detector. This encompasses not only the traditional detector control domains, such as high and low voltages, temperatures, gas flows, or pressures, but also the control and monitoring of the Trigger, TFC, and DAQ systems. The hardware components of the ECS are somewhat diverse, mainly as a consequence of the variety of the equipment to be controlled, ranging from standard crates and power supplies to individual electronics boards. In LHCb, a large effort was made to minimize the number of different types of interfaces and connecting buses.

The ECS software is based on PVSS II, a commercial SCADA (Supervisory Control And Data Acquisition) system. This toolkit [14] provides the infrastructure needed for building the ECS system, such as a configuration database and communication between distributed components, graphical libraries to build operations panels, and an alarm system as well as components, such as OPC clients.

Device Units denote low-level access components which model the physical device and typically communicate directly with the hardware. In general they only implement a very simple state machine which is exclusively driven by the controlling Control Unit. Examples of Device Units are power supplies, and software processes, such as the HLT processes.

Control Units implement high-level states and transitions and also local logic to support recovery from errors of subordinate Device Units. Typical examples of Control Units are

a HV subsystem, or the component that controls the ensemble of crates of a sub-detector or an entire sub-farm of the Event Filter Farm. Control Units can be controlled by other Control Units, to allow the building of a hierarchy of arbitrary depth. State sequencing in the ECS system is achieved using a Finite State Machine package, based on SMI++ [15] that allows creating complex logic needed, for example, for implementing elaborate sequencing or automatic error recovery.

The distributed components of the ECS system are connected with a large Ethernet network consisting of several hundred Gigabit and Fast Ethernet links.

2.10 Offline computing, Data Reduction and Storage

The most effective solution for meeting the data analysis challenge lies in a global computing infrastructure called the "Grid" [16]. This is a form of distributed computing, where computers located all over the world can be accessed via the Internet to harness their overall processing power. This method of resource sharing in effect creates a single huge and powerful computer brain to benefit all the network collaborators.

The Grid relies on the existing underlying hardware of the Internet (communication networks), with a specially developed software called "middleware". This organises and integrates the geographically dispersed resources into a coherent entity and enables access to the resource. To handle the complexity of the scientific tasks, the Grid includes major computer centres dedicated to supplying its resources with high-speed connections. Many Grid systems are developing and evolving. These may be private or public, regional or global, and may be multi-purpose or dedicated to one particular project.

The events which passed the trigger selections are stored for offline analysis. The data are further reduced via the so-called "stripping" selections, which are applied centrally to prepare preselected data sets for the various analysis groups.

2.11   Data Simulation

In the simulation, pp collisions are generated using Pythia 6.4 [17] with a specific LHCb configuration [18]. Decays of hadronic particles are described by EvtGen [19], in which final state radiation is generated using Photos [20]. The interaction of the generated particles with the detector and its response are implemented using the GEANT4 toolkit [21] as described in [22].

Chapter 3

Magnetic Distortion Calibration for the RICH-1 Detector

3.1 Hybrid Photon Detectors (HPDs)

3.1.1 Overview

The RICH detectors utilise Hybrid Photon Detectors (HPDs) to measure the spatial positions of emitted Cherenkov photons. The HPD is a vacuum photon detector, in which photoelectrons released from the photocathode by an incident photon are accelerated by an applied high voltage (typically 16 to 20 kV) onto a reverse-biased silicon detector. Electron-hole pairs are created at an average yield of one for every 3.6 eV of deposited energy during the photoelectron energy dissipation process in silicon. The nominal operating voltage of the HPD at 20 kV corresponds to ~ 5000 electron-hole pairs released in the silicon. Carefully-designed readout electronics and interconnects to the silicon detector result in very high efficiency at detecting single photoelectrons.

A dedicated pixel-HPD has been developed by LHCb, in close collaboration with industry [23][24]. The specific RICH requirements include:

- Large area of coverage ($\sim 3.5\text{m}^2$, RICH-1 + RICH-2),

- High active-to-total area ratio after close-packing (64%),

- High granularity (2.5×2.5 mm^2 at the photocathode), and

- High speed (25 ns timing resolution).

The pixel-HPD is shown in Figure 2.12. It is based on an electrostatically focussed tube design with a tetrode structure, demagnifying the photocathode image by a factor of ~ 5 onto a small silicon detector array, with a long (~ 125 mm) drift trajectory from the photocathode to the silicon sensor.

The HPD entrance window is fabricated from quartz and forms a spherical surface, with 7 mm thickness and 55 mm inner radius of curvature. The photocathode is of the thin-S20 multi-alkali type, deposited on the quartz inner surface. Normally-incident Cherenkov photons to the HPD plane can be detected over an active diameter of 75 mm. Since the overall tube diameter is 83 mm, the intrinsic tube active area fraction is thus $(75/83)^2 = 0.817$.

The silicon detector is segmented into 1,024 pixels, each 500 μm $\times$ 500 μm in size and arranged as a matrix of 32 rows by 32 columns. Each effective pixel used in LHCb (termed "LHCb pixel") actually consists of eight physical "ALICE pixels" (so termed since the silicon sensor technology was jointly developed by LHCb and ALICE collaborations but each with a different granularity requirement), each of area 0.5×0.0625 mm^2. The eight ALICE pixels are grouped together in the readout to form a single LHCb pixel. The nominal electrostatic demagnification factor of five [25] gives a measurement granularity of 2.5×2.5 mm^2 at the exterior of the quartz window. The silicon pixel detector array is bump-bonded to a binary readout chip. This assembly is mounted and wire-bonded onto a Pin Grid Array (PGA) ceramic carrier to form the HPD anode.
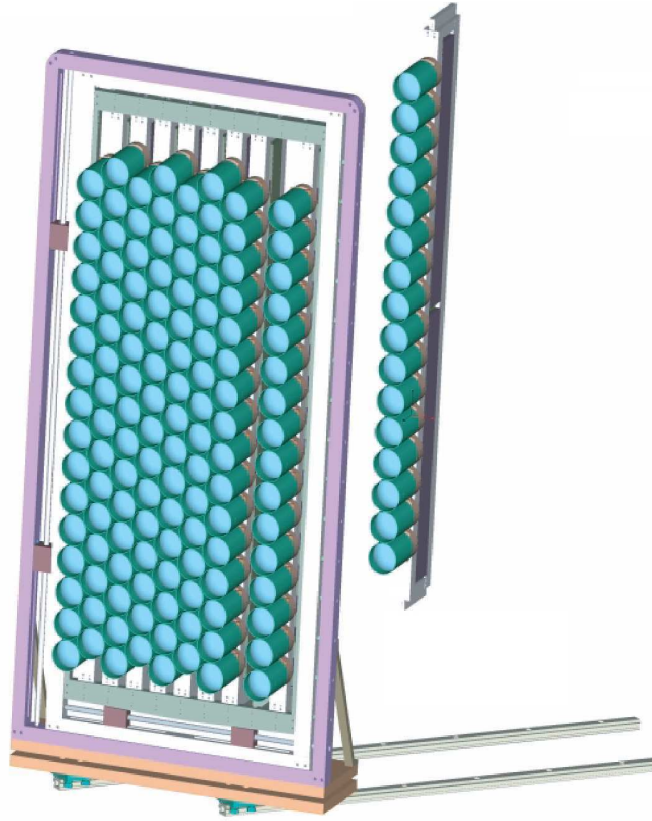
Figure 3.1:   Column mounting scheme for RICH-2.

3.1.2   Photon Detector Integration

A total of 484 HPDs (196 for RICH1 and 288 for RICH2) are required to cover the RICH photon detection areas. The HPDs are grouped in 4 detection planes (2 for RICH1 and 2 for RICH2) and positioned on a hexagonal lattice, chosen for the close-packing factor of 0.907. The HPDs are mounted on columns which are installed in the magnetic shielding boxes of the two RICH detectors. There are 2×7 columns of HPDs in RICH-1 with 14 HPDs per column and 2×9 columns in RICH-2 with 16 HPDs per column. Figure 3.1 illustrates the column mounting scheme for RICH-2. The column also contains front-end electronics boards (one per pair of HPDs), power supply distribution, cabling and active cooling, all within one mechanical module.

3.1.3 Physics Performance from Simulation

In physics simulation, the LHCb RICH system is modelled as part of the LHCb simulation program based on the GEANT4 toolkit [21]. All important aspects of the geometry and the material descriptions are fully implemented in the simulation. A database is setup with all this information which is then input into the simulation and the reconstruction programs. The Cherenkov light generation is performed inside GEANT4, with the photons propagated with the full knowledge of the expected reflectivities, transmissions and refraction effects at the various optical elements in RICH.

Table 3.1: Single photoelectron resolutions for the three RICH radiators. All numbers are in mrad. Individual contributions from each source are given, together with the total.

	Aerogel	C_4F_{10}	CF_4
Emission	0.4	0.8	0.2
Chromatic	2.1	0.9	0.5
HPD	0.5	0.6	0.2
Track	0.4	0.4	0.4
Total	2.6	1.5	0.7

The RICH's Cherenkov photon resolutions from simulation are shown in Table 3.1, where both the total resolutions and the individual contributions are listed. The single photoelectron resolution is largest for the aerogel in RICH-1, at 2.6 mrad, and smallest for the CF_4 in RICH-2, at 0.7 mrad. These resolutions have contributions from the uncertainty associated with the photon emission point, the chromatic dispersion of the radiators, the intrinsic pixel resolution and the point spread function (together listed as 'HPD' in the table). For the aerogel it is the chromatic dispersion uncertainty which dominates, whereas for the other two radiators the contributions are well matched. An additional uncertainty comes from the reconstruction of the track direction, which is identical for all three radiators.

3.1.4 Effects from Magnetic Fields

The RICH-1 HPDs are located at a position where the upstream fringe field from the LHCb dipole, in the absence of any materials in this region, is about 60 mT. Due to the cross-

focusing nature of the HPD design (Figure 2.12), this fringe field can affect the photo-electron trajectory, leading to distortions in the observed image and possible inefficiency when the photo-electron falls outside the sensitive area of the silicon detector [26][27]. Magnetic field tests have been carried out on the full-scale HPD equipped with a phosphor screen anode, exposed to fields up to 3 mT. The performance of the electron optics were studied and full details appear in a technical note [28].

Due to this magnetic distortion effect, the HPDs only operate at full geometric efficiency in a B-field up to 3 mT. With a longitudinal field of 5 mT there is a loss of about 4% of the photocathode area. Therefore shielding is required to reduce the external field by a factor of at least 20. The shielding boxes need to be large enough to accommodate the HPDs and their associated readout, and they must not obstruct Cherenkov light falling on the HPD photocathodes. Two types of shielding are used: iron shielding boxes for each HPD systems (upper + lower) and Mu-metal shields for individual HPDs.

3.2 Magnetic Shielding

3.2.1 Magnetic Shielding Boxes

The shielding has been designed with the aid of the TOSCA/OPERA1 finite element software package [8] with which the complete LHCb dipole was designed. The model resulting from an iterative optimisation procedure, is shown in Figure 3.2(a). The shielding boxes are constructed from very pure 50 mm and 100 mm-thick (ARMCO) iron with a high saturation field of 1.8 T. Their essential components are illustrated in the figure.

Measurements made with the shielding boxes in place and the LHCb dipole at full field indicate that the maximum B-field at the HPD plane is 2.4 mT (Figure 3.2(b)). The design of the shielding boxes also ensures that the field orientation at the HPD planes is primarily longitudinal, with only a small transverse component. The weight of each box is about 75 kN and the magnetic forces at full field are about 50 kN. The rigidity of the shielding structure
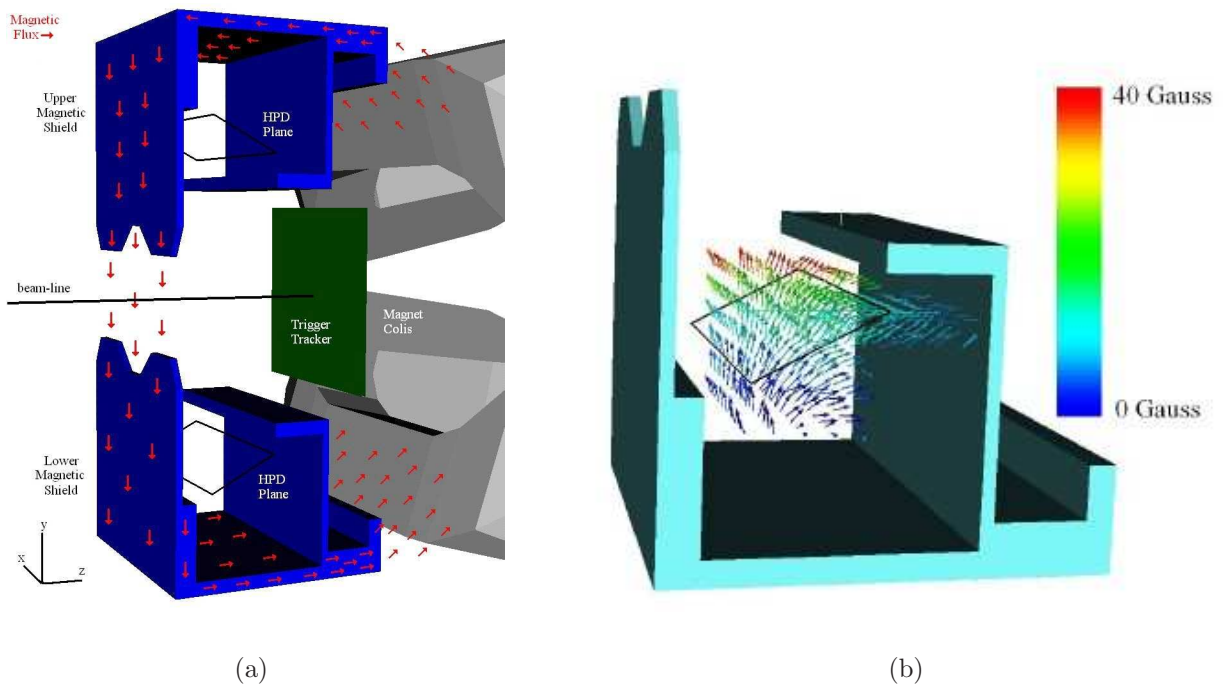
Figure 3.2:   (a) Design of the magnetic shielding boxes in RICH1. (b) Residual field inside the shielding boxes, where the rectangle shows the location of the HPD plane.

and mounting ensures that any displacement of the HPD assembly is less than 0.5 mm when the LHCb magnet current is switched on [29].

3.2.2   Individual HPD Shielding

To reduce further the field within the photon detectors, individual HPDs are also surrounded by a 200 mm long, 0.9 mm thick cylindrical Mu-metal (nickel-iron alloy) shield that is grounded and insulated with 250 μm Kapton foil (Figure 3.3). Mu-metal is chosen for its high permeability which allows effective screening of static magnetic fields. Mu-metal can have relative permeabilities up to 100,000 compared to several thousand for ordinary iron. The Mu-metal shield extends to 20 mm beyond the centre of the entrance window, resulting in minimal light shadowing of the photocathode. These individual shieldings reduce the field strength to under 0.5 mT within the HPDs.

The HPDs with the Mu-metal shields have been tested in both longitudinal and transverse

Figure 3.3:   HPDs with Mu-metal shieldings.

magnetic fields of 3 mT. The distortions of the electron optics, primarily a rotation of the image due to the longitudinal B field component, is shown in Figure 3.4 for a single HPD. There is no loss of the image from the active area of the pixelated anode. Transverse fields give small distortions but it is more difficult to shield due to saturation of the Mu-metal tube array. Testings with an array of 0.9 mm-thick Mu-metal cylinders in the RICH-1 shield indicates that the field inside the cylinders does not exceed 1 mT, while the field in the Mu-metal itself is 0.35 T, about one half the saturation value [29].

3.3   Magnetic Distortion Calibration System (MDCS)

Even with the two levels of shielding in place, it is necessary to correct for the distortion of the ring-images to obtain optimum Cherenkov angle resolution. As shown in Table 3.1, the expected Cherenkov angle resolution with C_4F_{10} radiator is 1.55 mrad, of which 0.6 mrad comes from the HPD intrinsic resolution. If the distortion from residual magnetic field is uncorrected, it will contribute to an additional factor of 1.3 mrad on the angle resolution, due to the distortion effects as illustrated in Figure 3.4. Therefore the magnetic distortion calibration systems (MDCS) are designed to correct for the field distortions.

(a) (b)
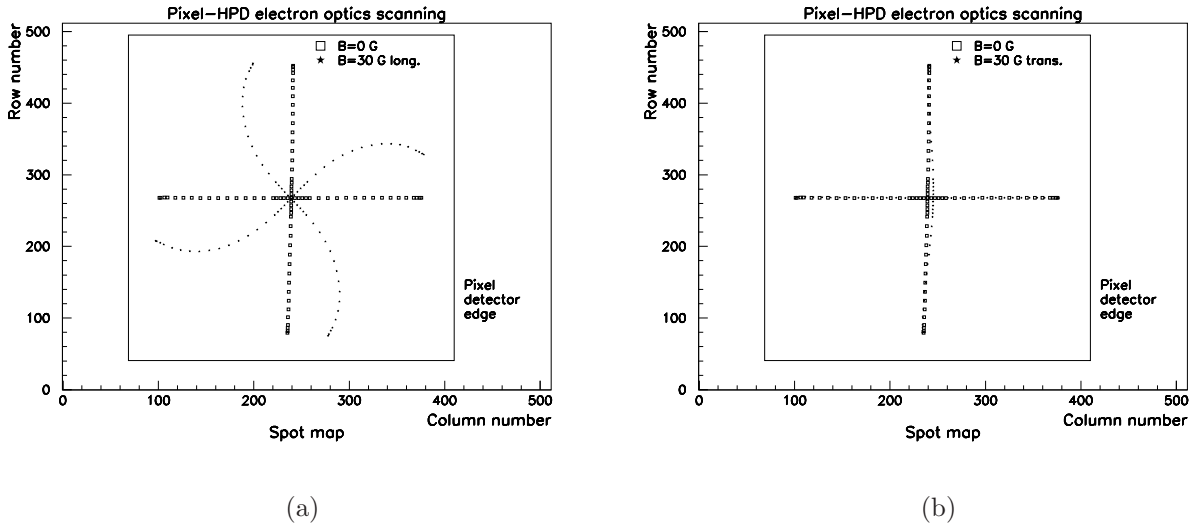
Figure 3.4:   The effect of 3 mT longitudinal (a) and transverse (b) B field on an HPD image without Mu-metal shieldings, from simulation.

3.3.1   Apparatus

There are two identical MDCS in RICH-1, one each for the upper and lower HPD boxes. The RICH 1 MDCS is designed to produce a high density grid of light-spots which can provide a detailed map of any distortion and the ability to perform an absolute calibration. The system is comprised of a series of LEDs boards mounted on a LED bar that traverses the width of the photon funnel. In total 19 LED boards are aligned in series and are mounted and glued between two carbon-fibre supports. Each board is comprised of 5 arrays of 28 LEDs (Figure 3.5). The spacing between adjacent LEDs is 2.5 mm from centre to centre. The boards are aligned in a way such that it has a 11.31° (or arctan $\frac{1}{\sqrt{26}}$) tilt with respect to the length of the LED bar. With this layout the distance between LED centres in the long (i.e. mount bar) direction can be as small as 0.498 mm, compared with 2.5 mm without the tilt. Unfortunately this fine design feature cannot be utilised in the current calibration procedure due to the amount of time it take to scan across the whole HPD plane with such granularity.

The LED boards are connected in series with an input voltage set to 5.1 V. At this value, if one LED is turned on for each board it provides an approximate flux of green photons
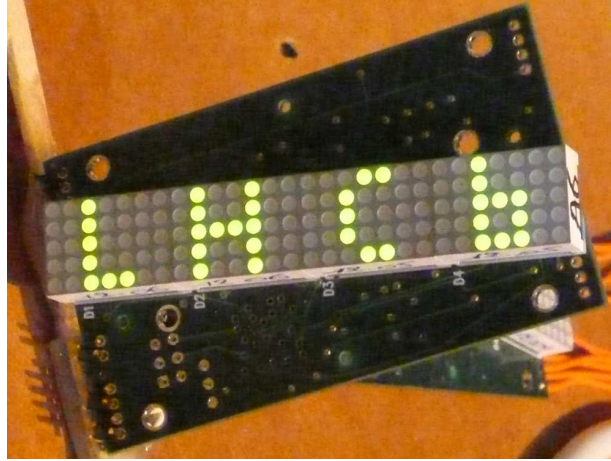
Figure 3.5: A single MDCS board with 5 arrays of 28 LEDs.
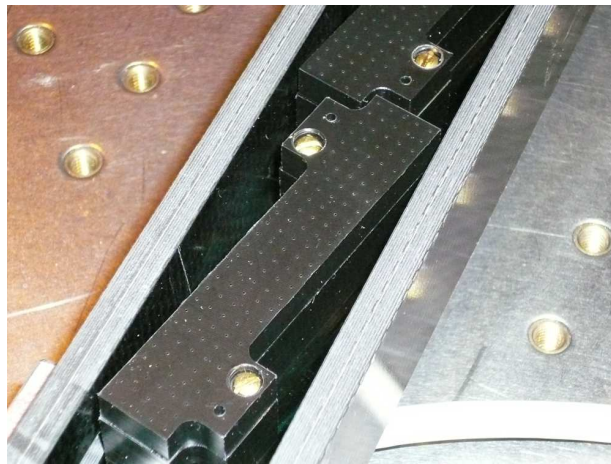
Figure 3.6: MDCS boards with collimator mounted on top.

at 1 MHz per LED. This voltage is controlled via a local bar regulator. Each LED bar is powered by a 7.5 V power supply located some 20 m away from the detector. The bars are connected to the power supplies with shielded 25 m DB25 cables. The voltage drops at the regulator and across the cable are dependent on the number of illuminating LEDs on each board (i.e. the calibration pattern). At one LED per board, which is the setup used in the calibration, the voltage drops were measured to be 0.5 V at the bar regulator and 0.4 V for a 25 m long cable. These drops were then compensated in the input power settings.

Collimators are mounted on the front face of the LED boards to control the LED light-spot size and improve the precision of the system (Figure 3.6). Several designs of the colli-mator with various shapes and length were proposed and tested (Figure 3.7(a)). The results

are shown in Figure 3.7(b). A simple straight design (Type C) suffers from diffraction effect coming from light reflected by the internal wall of the collimator. The Type-E design was finally chosen for providing the optimum light-spot size.

The LED bar is mounted on a gantry, each side of which is connected to a Parker LP28 linear stage along the long side of the photon funnel, an aluminium welded structure between the RICH-1 gas enclosure and the HPD box. Each stage is 540 mm long, this dynamic range allows the LED bar's illumination to cover the effective area of all seven HPD columns (Figure 3.8). The LED bar is driven by a pair of Parker LD28 stepper-motors (Figure 3.9), synchronised by a single ViX-500-IM Stepper Drives controller unit to avoid differential movement of a cantilevered load. The power transmission from the stepper-motors to the gantry is via a gear box as shown in Figure 3.9(b). The gear ratio is chosen so that 4,000 steps from the motor corresponds to an LED bar movement of 3 mm. An LP28 positioner is used to record the reading of steps in a movement for monitoring the position of the LED bar. The position repeatability of the motor is extremely good. If a travel through the full 540 mm length of the stage is performed with up to 100 stop-and-go movements, the error on the final position reading is less than 40 μm. In comparison, the size of an HPD pixel, when projected to the outer surface of the quartz window, is 2.5 mm. The start position of the LED bar is defined with respect to a limit/home switch installed on the LP28. This home switch is a hall effect sensor tripped by a magnet embedded in the carriage. It signals to the motor to stop whenever the carriage is approaching the end of travel and provides a fixed reference point to which the carriage can be commanded to return repeatedly. It has a position repeatability better than 100 μm.

At any time other than a calibration run, the LED bar is located at the "Parking" position (Figure 3.8(a)) out of the fiducial volume, to avoid blocking Cherenkov light in physics data taking. In a calibration run, the synchronised motors drive the LED bar along the 540 mm stages to scan over the front-faces of the HPD arrays with a dedicated calibration grid pattern from the LEDs.

The final position of the MDCS, mounted inside the photon funnel, is shown in Figure
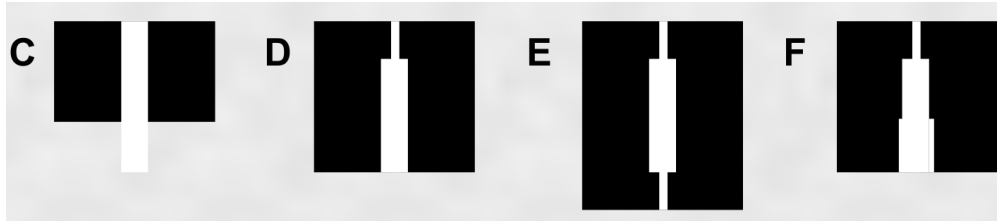
(a)
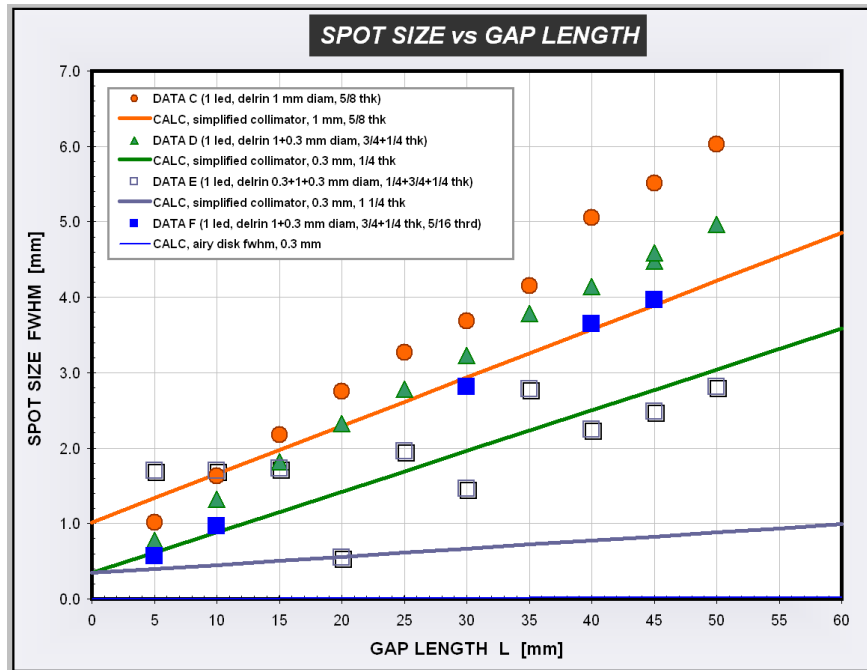
(b)

Figure 3.7:   (a) A selection of collimator designs. The light from the LED comes through from the bottom. (b) Test results comparing the collimator designs above. As can be seen Type E has the best performance and is thus chosen as the final design.

(a)   (b)
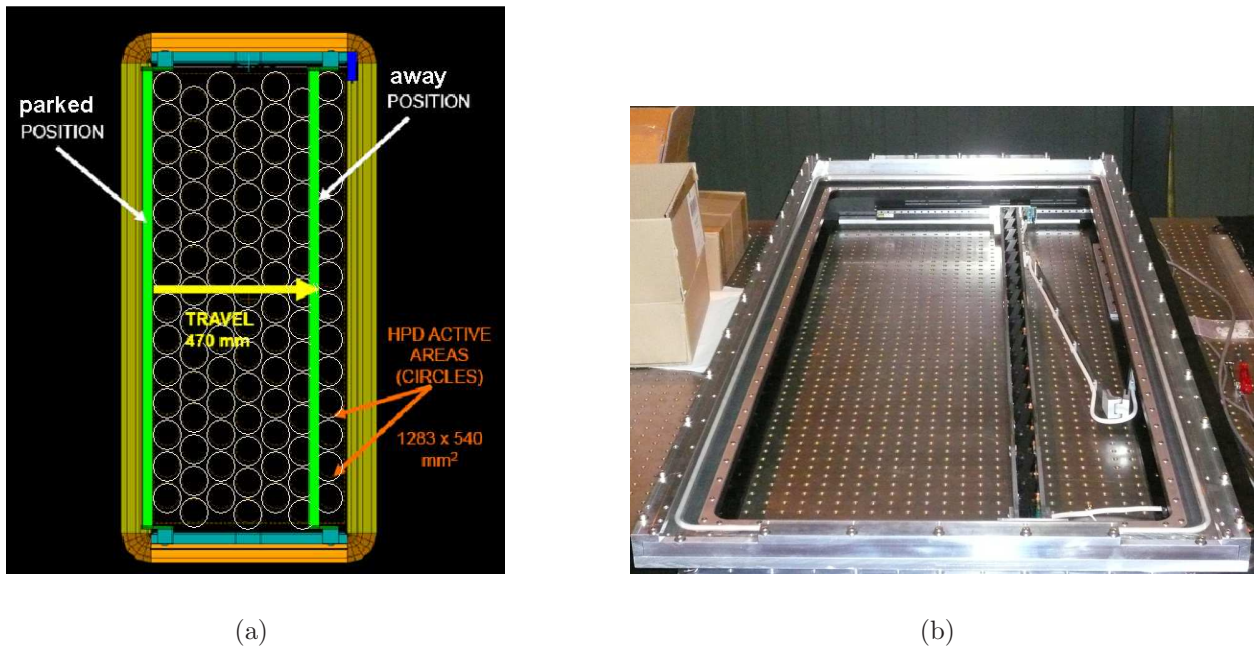
Figure 3.8:   (a) Engineering drawing of MDCS LED bar installed in the photon funnel. The circles indicate the active HPD areas. (b) MDCS LED bar in the photon funnel, before integration with the HPD box. During physics data taking the LED bar is parked on the right end to allow clear passage of Cherenkov light.

(a)   (b)
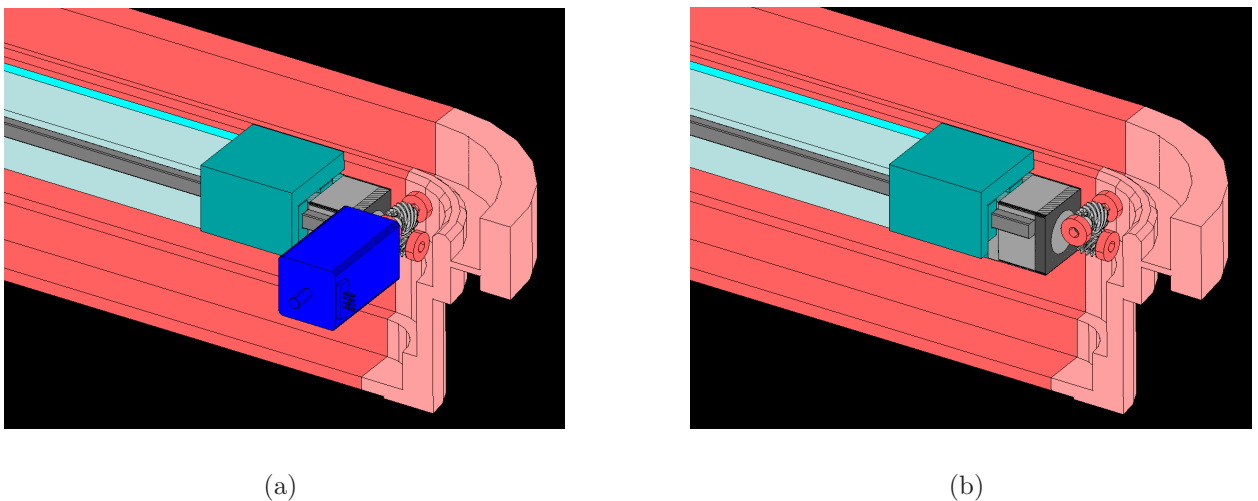
Figure 3.9:   (a) An LED bar with Parker stepper-motors shown on the right. (b) The same view with the motor removed for a clearer sight of the gear box.
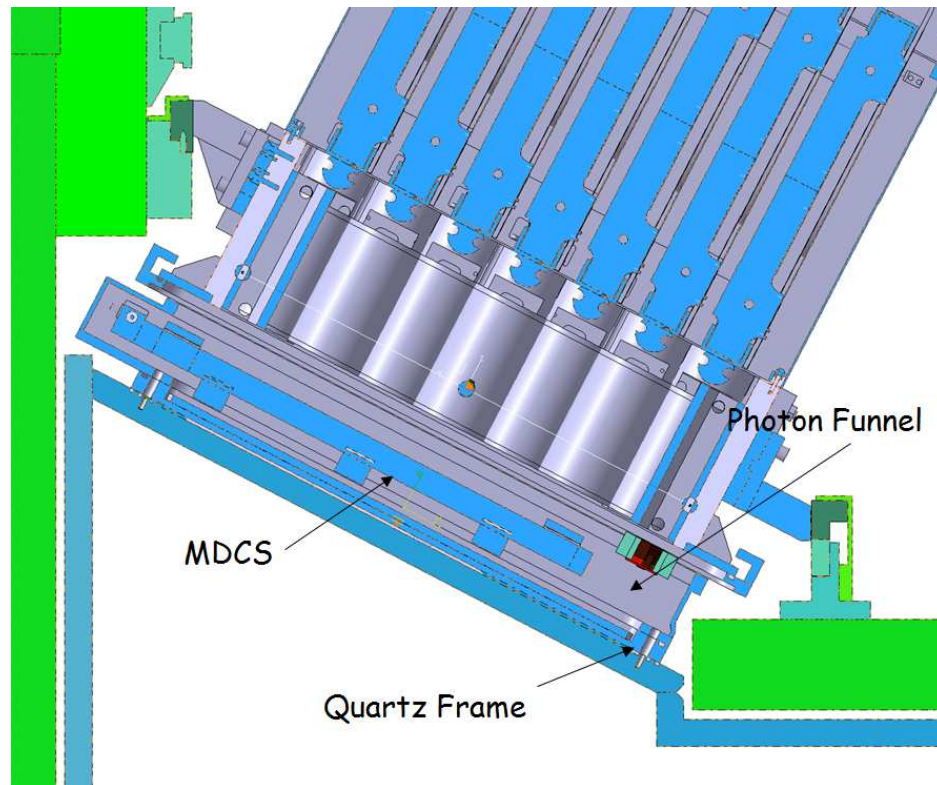
Figure 3.10:   Upper MDCS and the photon funnel.

3.10. It is located ~ 80 mm from the front entrance of the HPDs (Figure 3.11). The "Parking" position of the LED bar is on the upstream side in the funnel. The photon funnel is an aluminium welded box. Its location between the radiator gas enclosure and the HPD boxes places numerous constraints on its dimension. Within a width of 75 mm it has to provide enough room for the MDCS, including space for extra length of the stages as well as the patch panel. A quartz window is mounted at the bottom of the funnel to close the gas enclosure while at the same time providing clear passage for Cherenkov lights.

The MDCS has to be controlled remotely via the LHCb online network, therefore it is essential that the commands can be sent using Ethernet. A Lantronix XPORT module is used to handle the Ethernet to serial conversion. The XPORT is registered in the online network with a specific IP address. Once the XPORT gets an IP address, it can be configured via a web browser. When TCP/IP communication is established with the XPORT, commands can then be sent to the LED units and the stepper motors. Two identical control boxes, one for each of MDCS, are installed about 20 m away from the photon detectors in a local
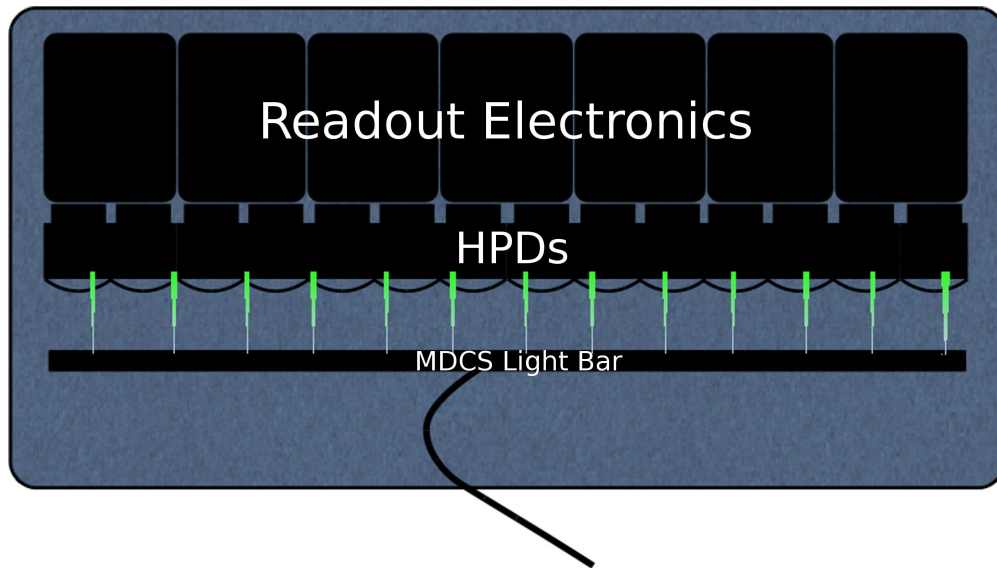
Figure 3.11:   The position of the MDCS with respect to the RICH photon detectors.

power supply rack. Each box contains one Parker ViX-500-IM Controller and XL-PSU Power Supply, both for the stepper-motors, as well as a 7.5 V power supply for the LED bars.

3.3.2   Software Control

The MDCS is located inside the LHCb detector in the underground cavern, hence it is essential to have a remote operation capability. For the RICH-1 MDCS, the operation is performed via PVSS [30], the LHC-wide standard detector control software. PVSS is a supervisory control and data acquisition tool. It can be used to connect to hardware devices, acquire and process the data they produce for supervising the devices. Control panels can be designed using PVSS graphical objects. The PVSS control scripts are based on C (Figure 3.12). They can either be embedded in a graphical object or run in the background independently. In the MDCS main control panel (Figure 3.13), embedded control scripts are written to automate the movement of the LED bar and the LED pattern sequence. The remote communication between PVSS and the hardware is achieved via TCP/IP protocol. The upper and lower systems receive identical instructions simultaneously.

The MDCS main control panel (Figure 3.13) is designed in a tabbed structure. The first tab is designed to handle all standard running scenarios. Sector 1 of the panel handles
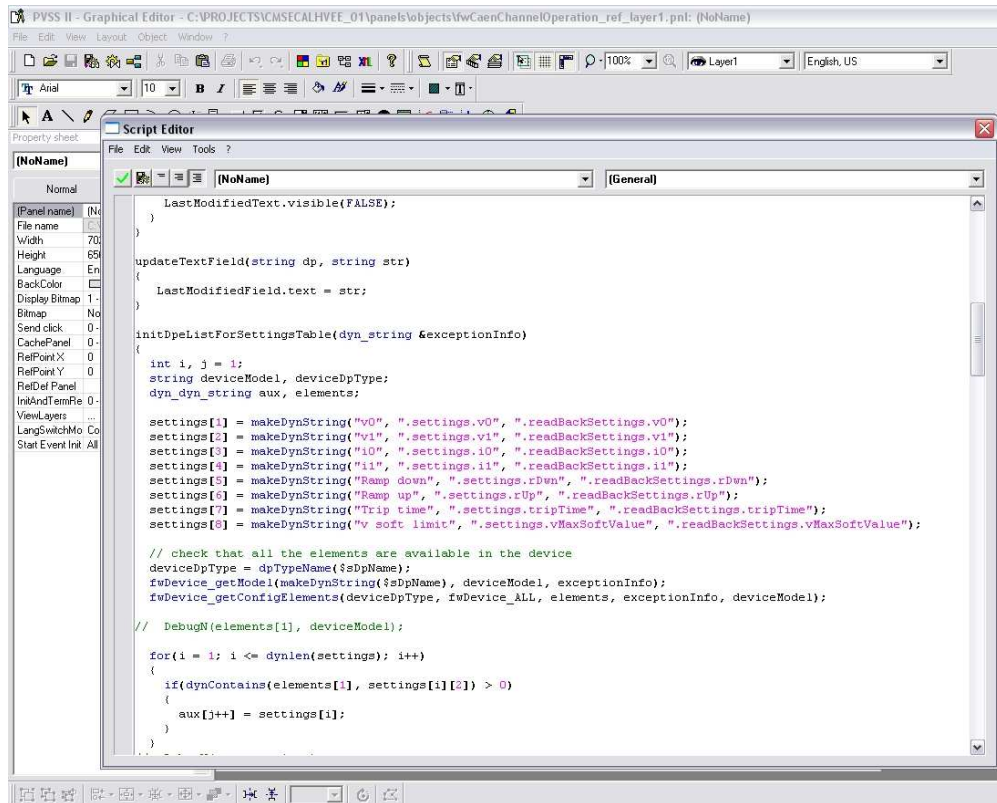
Figure 3.12: An example of script editing with the PVSS software.

the communication establishment to the hardware, where one can choose to operate the Upper and Lower system independently or simultaneously. Sector 2 takes the stepper-motor movement parameters for a calibration scan. In addition the user can choose one of the three pre-defined LED calibration patterns. The text boxes at the bottom of the panel show monitoring information. The left boxes show the command that has been sent to the hardware from PVSS. This is useful for confirmation and debugging. The right boxes display responses from the hardware controllers. These include for example the acknowledgement from the controller upon receiving commands, the reading of the stepper-motor position from the LP28 positioner etc. A script is written embedded in the panel to convert the hex strings from hardware to human readable information. On the right of the main panel is a list of frequently used command buttons. Each button has embedded scripts to send corresponding commands to the hardware controller:

- The "Park" command returns the LED bar to the parking position which is defined as

500 motor steps away from the home switch;

- "List All Parameters" returns the initialisation parameters of the hardware system;

- "Set Soft Zero" is performed once in a while to ensure there is no systematic shift of the LED bar starting position;

- "Emergency Kill" is used to stop all hardware actions in the extreme scenario when the MDCS action may cause any damage to the rest of the RICH systems. This occur if the motors become desynchronised, or the speed of the motor is out of control.

The rest of the tabs on the main panel are mainly designed for more detailed monitoring as well as for hardware testing. For example, tab 2 "LED Settings" allows the user to override the pre-defined LED patterns. In this tab the 5×28 arrays of the LEDs are visualised for configuring patterns interactively. The embedded scripts then convert the visual pattern to the hex commands to send to the hardware. Tabs 3 and 4 allows the patterns set on each LED board to be monitored individually. Tab 5 contains more advanced actions, including those associated with the safety lock system and the stress-testing of the system, and is reserved for MDCS experts.

The MDCS control is an integrated part of the LHCb RICH Detector Control and is connected to the other sub-detectors via Finite State Machine (FSM) architecture [31]. FSM is a tool which uses the SMI++ (State Management Interface) language to model abstract detector behaviour. Sub-detectors are modelled as a hierarchy of FSM "objects" e.g. LV, HV, Cooling, etc., each with its own set of "states": Off, Configured, Running, Error, etc. as shown on the top left in Figure 3.14. Transitions between states are defined with a set of control scripts. A software safety lock is programmed so that the MDCS control can only be activated when the run type is set to dedicated magnetic calibration runs.

In the default operation, the MDCS is controlled from the RICH-1 top panel (Figure 3.14). It is operated with a calibration stepping mechanism that is used to provide a link between the hardware control and the DAQ. Each LED pattern is associated to a single calibration step; with this it is possible to remove the ambiguity on the reconstructed patterns.
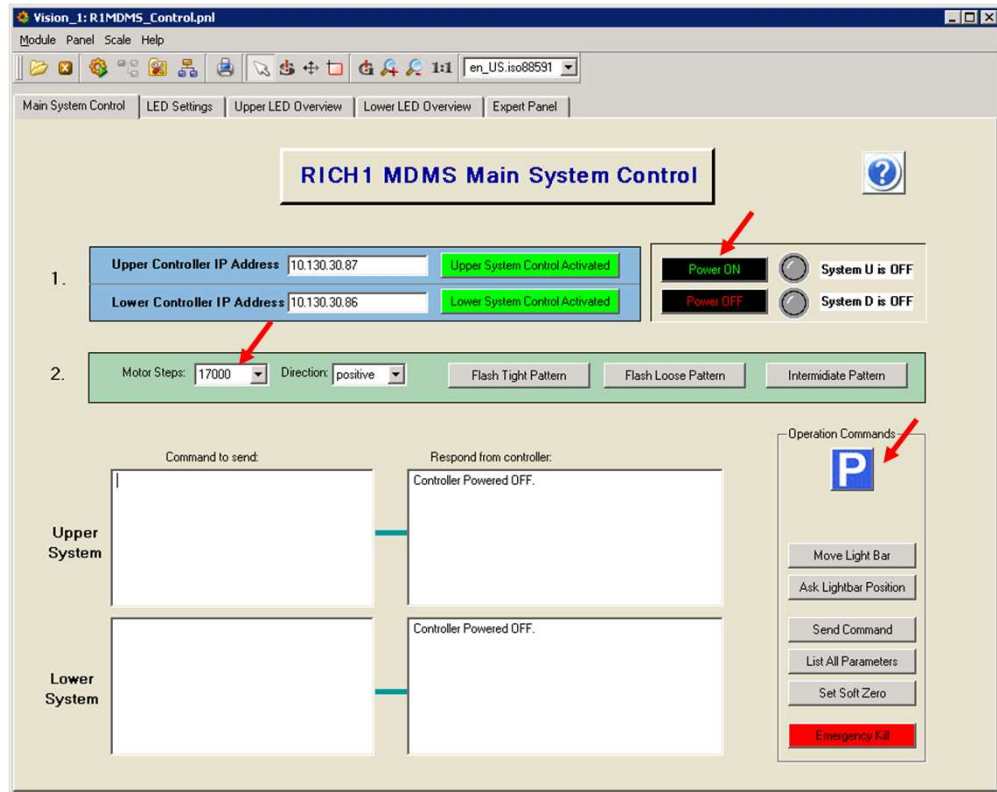
Figure 3.13: MDCS main panel designed in PVSS, for remote control of the system.

The calibration step is an integer, stored in the ODIN bank (readout supervisor) in the raw data. The calibration stepping was originally designed for the purpose of the L0 DAQ board calibration. It enables the grouping of raw data in the ODIN bank using the calibration step number. In this way the reconstruction and the subsequent analysis can distinguish the correct LED light spots pattern by pattern. This feature is very important when comparing different sets of scan data or when comparing the scan data to the grid, as a wrong pattern-position matching will completely ruin the analysis. The ODIN can be configured to collect any number of events for each of a pre-defined number of steps. During a calibration scan, the system is configured in ALICE mode (where data recorded with each of the 8 "ALICE pixels" within an "LHCb pixel" are individually read out) as oppose to LHCb mode (where the 8 "ALICE pixels" are combined in the readout to form a single "LHCb pixel") in physics data taking, in order to have a finer granularity in the event reconstruction. The progress of the calibration scan can be monitored via the online monitoring histograms. Alternatively, the MDCS Main panel (Figure 3.13) can also be used for for the scan progress. The display
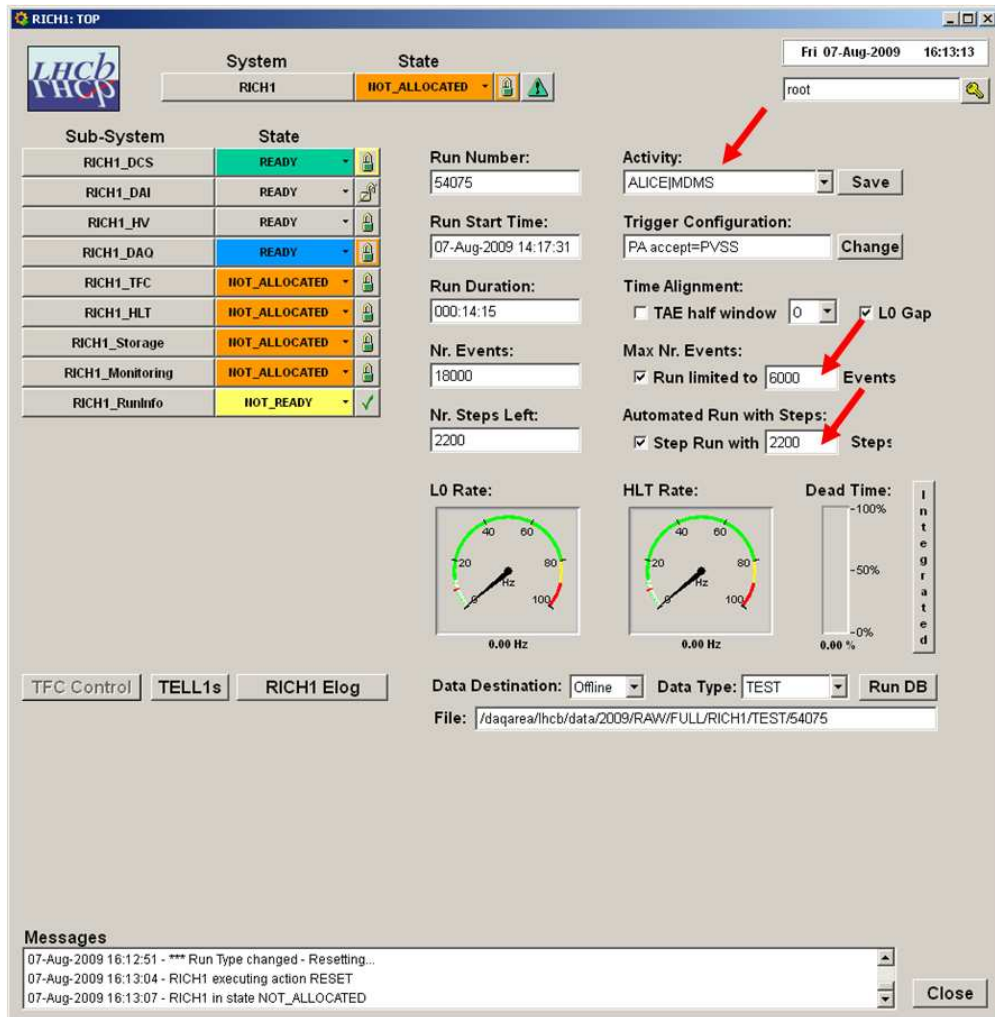
Figure 3.14: RICH-1 top panel, from where MDCS calibration scans are initiated.

box at the bottom constantly updates the positions of the LED bars and the total progress of the scan.

3.3.3 System Performance Test

Both the upper and lower MDCSs were tested in-situ with the complete RICH system. The tests were mainly focused on photon yield, pattern resolution and position repeatability.

When the DAQ system is configured with a trigger set at 5 kHz, the recorded photon yield on an HPD is $\sim 4,000$ per LED per second. A light spot usually covers a 6×6 pixel area. The position of a light spot is calculated as the centre (mean) of each light spot on
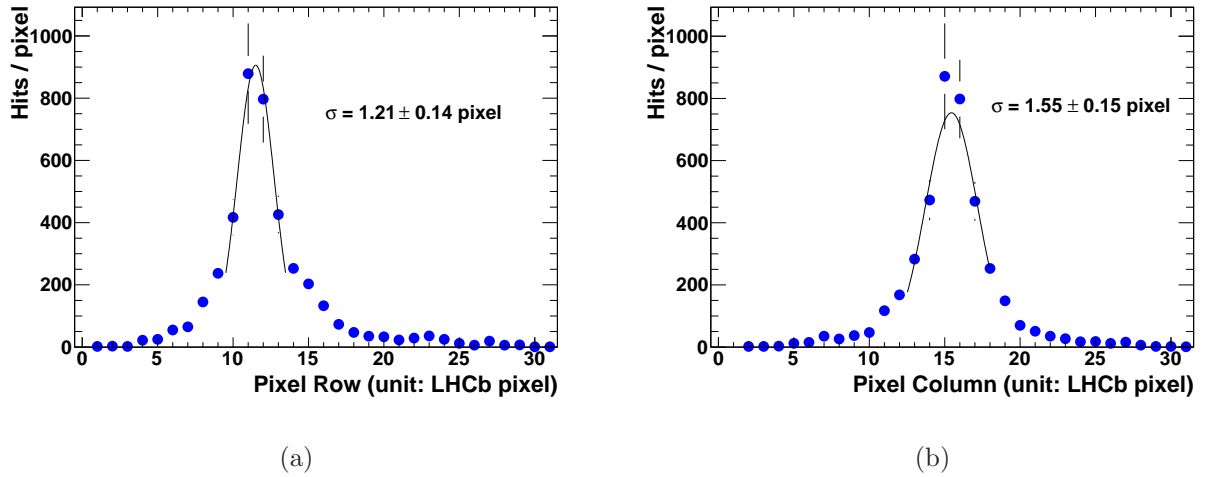
Figure 3.15:   Resolution of a single LED light spot projected along (a) the 0.0625 mm pixel spacing direction, (b) the 0.5 mm pixel spacing direction.

the anode. The precision of the centre-of-gravity calculation on such a pixelated surface is proportional to the inverse square root of the number of photo-electrons. Figure 3.15 shows the peak structure with $\sim 6{,}000$ photons. Due to the 0.5×0.0625 mm^2 ALICE pixel size, one direction gives finer granularity compared with the other. A two-dimensional fit gives the width of the Gaussian of 1.4 pixels, which corresponds to ~ 3.6 mm.

During the testing it was noticed that several samples exhibit multiple-peak structure (Figure 3.16), where only one peak is expected. This is now understood to be due to the total internal reflections (TIRs) in the HPD quartz window. When the LEDs illuminate close to the edge of an HPD (Figure 3.17), the light refracted by the quartz windows's top surface can have an incident angle larger than the critical angle of quartz $\sim 40.49°$, which results in the TIRs within the quartz window. Photoelectrons are released when the reflected light hits the photocathode at the bottom of the quartz window. Up to 6 reflections can happen given the quartz window's 7 mm thickness and 55 mm inner radius. This structure only appears when the centre of spot is within 5 mm, or 2 pixels from the edge of the HPD.

The total internal reflection creates a complication for the analysis, as the reconstruction returns multiple reflected peaks in addition to the true light spot. It is possible to exploit the differences in property between those reflected peaks and the real light spots to filter
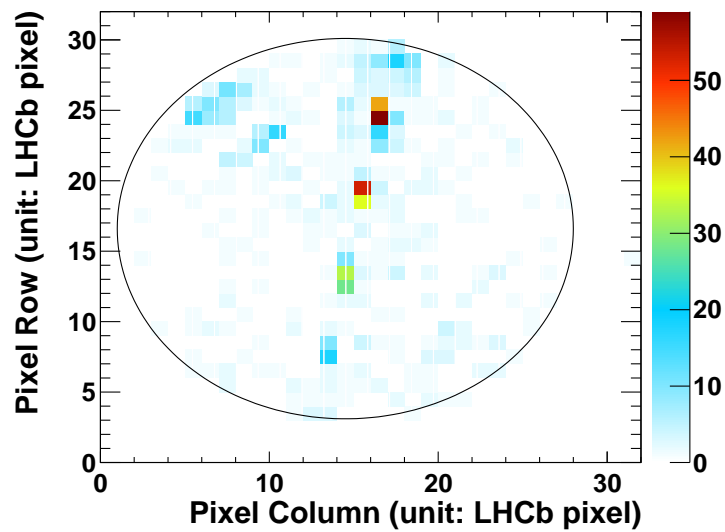
Figure 3.16: Multiple-peak structure seen on the HPD with a single-LED pattern.
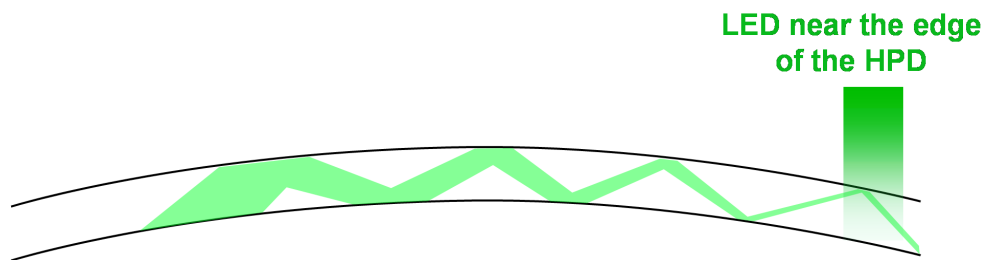
Figure 3.17: Total internal reflections occur when the LED light falls close to the edge of the HPD quartz window.

out the former. For example, the width of the light spots from reflection tends to be smaller than that of the true light spot. In addition, the relative percentage of total hits under each peak is different between events with and without reflections.

3.3.4 HPD Image Shifting Problem

Several MDCS position repeatability tests were performed, including one in which 5 hours of data was taken with a static pattern. When the data were analysed it was found that over 25% of the HPD images "wander" by maximum displacements of over 1 LHCb pixel. An example with one of the largest displacements is shown in Figure 3.18. As can be seen the position of the HPD image appears to shift continuously over time and the movement is
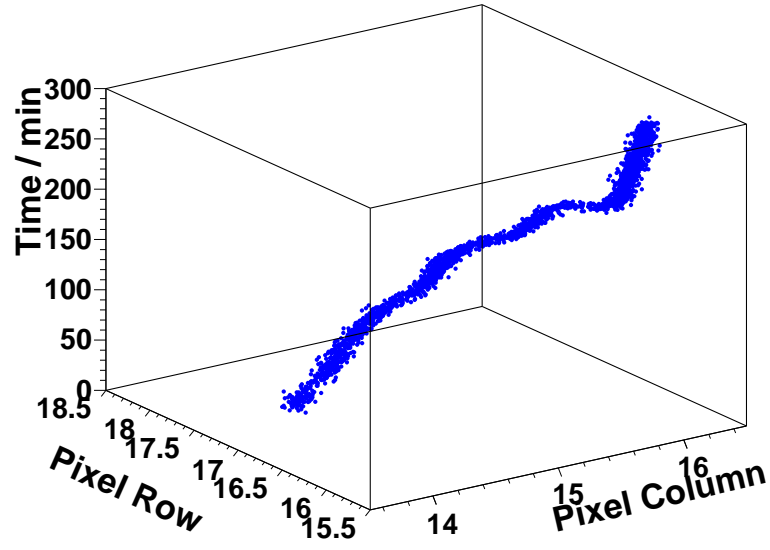
Figure 3.18: Disc image movement over time. X-Y coordinates: the amount of shifts in LHCb pixel unit. Z coordinate: time in second.

not restricted to one direction.

With data from repeated tests, it appears that the images from all HPDs are equally likely to move. While a few HPDs appear to have more significant movements than others, some HPDs can have stable position readings for hours and then suddenly start to move. These movements do not seem to be location dependent (Figure 3.19) or correlated to environmental variables e.g. HV level, temperature, humidity etc. The most rapid shift observed was at a rate of 2 pixels over 2 hours. That means if a shift of 1 pixels is considered to have significant impact on the Cherenkov angle resolution, it has to be calibrated hourly. Most HPDs move slowly, but studies with multiple set of test data show that it is difficult to predict what can suddenly happen on any given HPD.

This strange feature was confirmed by independent analysis using laser illumination, as well as with dark current where no external light source is used to illuminate the HPDs. Lab tests were carry out with a spare HPD installed under a similar condition as it is in the pit, in order to study the cause of the movement. It is now understood to be a problem with the HPD grounding. The ceramic inner surface of the HPD is electrostatic. However, over time it is possible for the charged photo-electrons to accumulate and eventually discharge
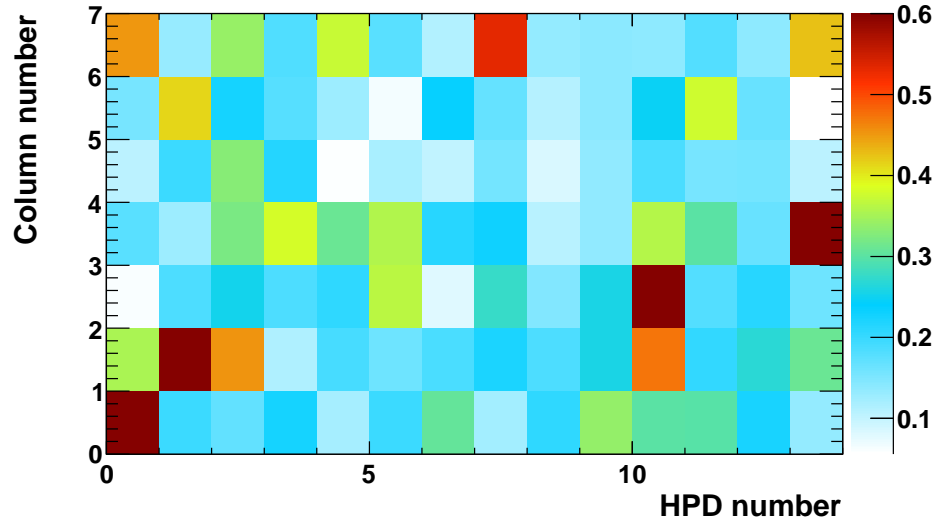
Figure 3.19: The amount of shifts (unit in LHCb pixel) for all HPDs in the upper box comparing 2 measurements taken 5 hours apart. The shifts do not appear to be location dependent. Note that this plot only compares two points in time and does not represent the maximum amount of shift, which can be significantly larger, during the 5-hour period.

in a localised area, without proper grounding. This localised voltage can distort the cross-focusing path of the photo-electrons and make the HPD image appear to move.

It is necessary to calibrate this random movement in order to reconstruct photo-electrons with the correct centre coordinates. The MDCS does not seem to be the ideal system to perform this however, as a complete MDCS scan take more than 3 hours. Further tests show that no rotation is detected from this kind of movement (Figure 3.20), which means the shifts can be calibrated without needing to run an MDCS scan. Therefore the calibration can be done more frequently if required. The exact procedure is being devised within the LHCb RICH group, and the results will be complementary to that from the MDCS.

3.4 Magnetic Distortion Analysis

To perform a calibration, it is essential to design a known pattern that can be compared between magnet-on and magnet-off data. Each light spot in such pattern has to be reconstructed unambiguously. As the photo-electrons are cross-focused from the photocathode to the anode, careful extrapolation has to be made to map the hits from the pixel chip to the

(a)   (b)
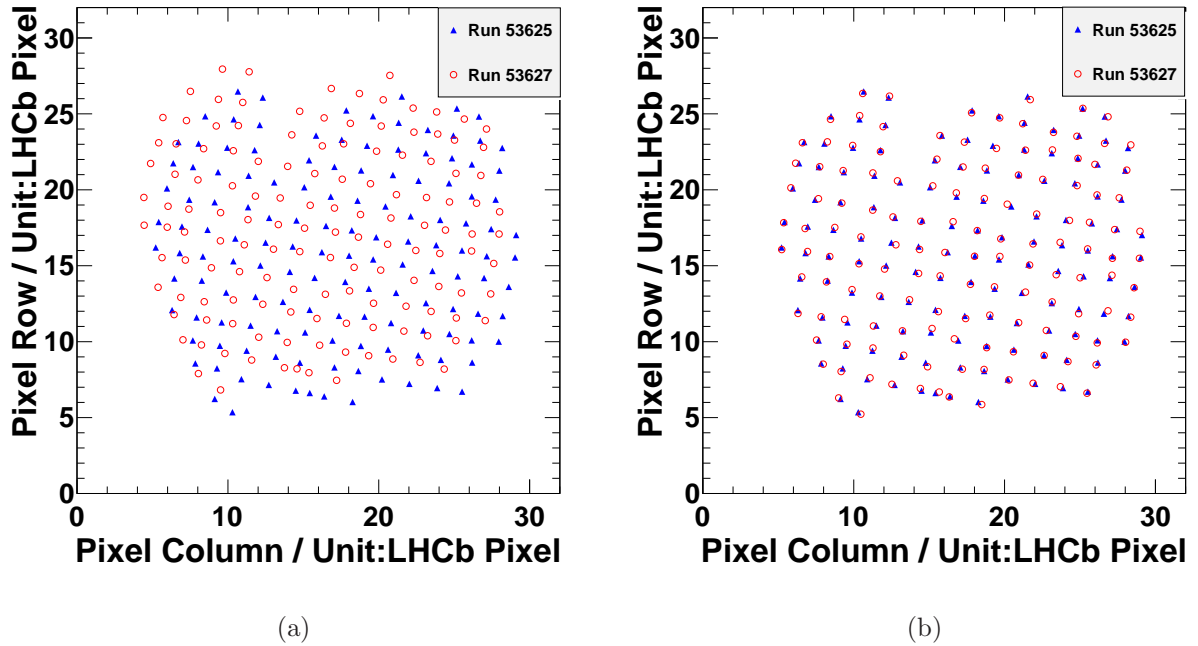
Figure 3.20:   A demonstration that the image shift does not involve rotation: The light spots from two runs appears to be dislocated from each others (a), but after applying a simple x-y translational correction they become almost identical (b).

front of the quartz window. By comparing the pattern position differences between field-on and field-off data, one can parametrise the corrections for distortions from both longitudinal and transverse components of the magnetic field. At the last step of the calibration, the correction parameters are stored in the Condition Database so that they can be used in offline reconstruction. At the end of this section the performance of the parametrisation on 2009 collision data will be shown.

3.4.1   Calibration Pattern

The basic principle of the calibration is to project a known pattern of light directly on the matrix of the HPD and design an algorithm to reconstruct the pattern. Performing these with and without magnetic field allows the effect of distortions in the known pattern to be analysed. It is then possible to characterise and parametrise the magnetic distortion correction and apply it in the online reconstruction. The requirement is that the correction

process must obtain a result such that the residual uncertainty due to the magnetic distortion is negligible compared with the intrinsic resolution of an HPD pixel (0.6 pixel).

As already explained, the total internal reflection creates a complication for the analysis when the LED is shining at the edge of the HPDs. It is possible to exploit the differences in properties between those reflected peaks and the real light spots to filter out the former. However, it is difficult to define a filtering process that can retain all the real light spots, particularly when a pattern contains more than one true light spot on a single HPD. Often such a filtering process results in "holes" in the integrated pattern, where good light spots are also incorrectly filtered out.

Taking into account the requirements of pattern "cleanness", time constraint and the target resolution, it was decided to define an LED pattern sequence such that for every pattern there is always only one or zero LEDs shining on each HPD. With that we can discard (in the analysis) a pattern in an HPD if it contain more than one peak, as they are almost certainly background from TIRs. Grid patterns with two different spacing, 2.5 mm and 5.0 mm, have been tested for comparison. The results show that both have similar performance in resolution, with the latter having an advantage of quartering the scan time. The grid spacing is subsequently chosen to be 5.0 mm. This spacing is achieved by turning on every other LED along either directions on the LED bar.

As mentioned in the hardware section the smallest control unit of the MDCS hardware is an LED board (Figure 3.5) and there are 5 columns of 28 LEDs on each board. Due to a limitation in the hardware design, only one column and a maximum of 14 LEDs on that column can be switched on at any given time on a board. Therefore to cover the whole effective HPD coverage with the grid pattern, a sequence of LED pattern changes and LED bar movements has to be defined:

Movement: The length of a LED bar movement is defined in such a way that LED column 01 in movement n is exactly one column spacing away from column 05 in the last movement $n-1$, along the direction of the LED bar travel. This corresponds to a movement length of 12.75 mm (i.e. 2.5 mm $\times \sqrt{26}$). The stepper-motor is set to move 17,000 steps

in each movement. The start position of movement 1 is defined as 25,500 steps, or $1.5\times$ movement length, forward from the LED bar "Parking" position. The relative positions of the LED boards between two adjacent movements are illustrated in Figure 3.22. As can be seen the projections of the two board positions sit right next to each others, with zero gap or overlap. In total, 42 movements are required to scan over the entire HPD coverage. The end position of the LED bar after movement 42 is just short of the 540 mm full length of the stages and beyond the effective area of the HPDs.

LED patterns following a movement: The light on the LED boards are only turned on when the LED bar is stationary, i.e. after a movement is completed. Two sets of patterns are used, depending on whether it is following an odd or even number of movements. For odd movements, the pattern starts with LED 1 on column 1, followed by the $(2n-1)$th LED in the nth pattern, until LED 27 is reached in pattern 14. The sequence is illustrated in Figure 3.21. In total, there are 15 patterns on each column, including 14 one-spot pattern on each odd LEDs plus one "blank" pattern without any LED lit at the end. This "blank" pattern is used to signal a change in column in the offline reconstruction. The same sequence then appears on column 3 and 5, successively. For even movements, the first pattern starts from LED 2 on column 2, followed by the $(2n)$th LED in the nth pattern, until LED 28 in pattern 14 and another "blank" pattern. Following that is the same sequence on column 4. The reason for having different patterns for two adjacent movements is to correct for the $11.31°$ tilt to keep the grid spacing along the direction of movement always the same and equal to that along the LED bar columns (i.e. every other spot).

The two configurations above combined produces a 2D grid pattern (Figure 3.22), with one axis along the length of the LED board direction (i.e. with a $11.31°$ angle tilt with respect to the LED bar direction), and the other axis perpendicular to the first.

The LED pattern change is controlled by the calibration stepping mechanism as described in Section 3.3.2. When a calibration run is initiated from the central RICH Detector Control panel, the MDCS PVSS control waits for the change in calibration step before initiating a command to the MDCS hardware. The ODIN is configured to run for 2,200 calibration
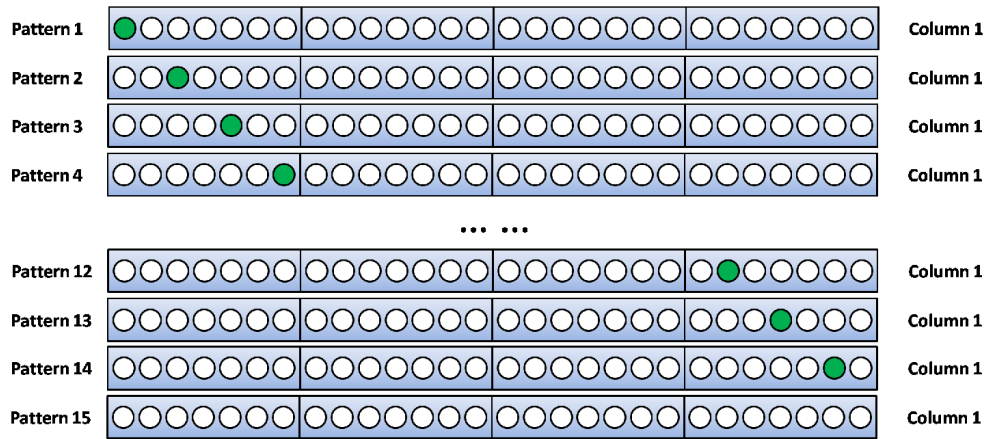
Figure 3.21: An illustration of the calibration pattern sequence on Column 1 following odd number of movements, starting from top to bottom. Only the 1st LED is turned on in the first pattern, while only the 3rd LED is on in the second pattern. In the nth pattern, only the $(2n-1)$th LED is on. This continues until the 27th LED is reached in pattern 14. It is then followed by a blank pattern 15 with no LED on, to signal a change in column in the offline reconstruction. The same sequence then appears on Column 3 and 5, successively. Column 2 and 4 are skipped to give a grid spacing of 5.0 mm. For the same reason only every other LEDs are lit along the column direction. In comparison, patterns only appear on Column 2 and 4 after even number of movements. The integrated patterns are shown in Figure 3.22.
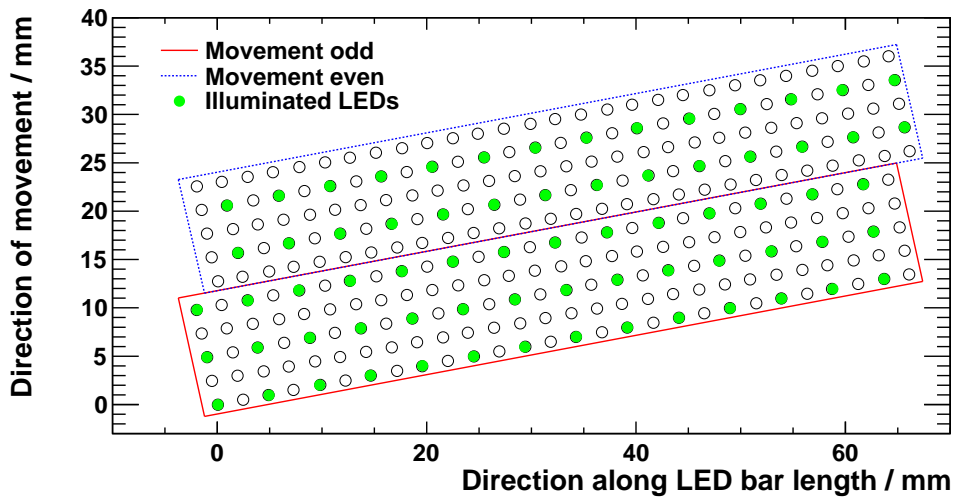
Figure 3.22: Integrated grid pattern from two adjacent movements, from a single board. Columns 1, 3 and 5 are lit following odd number of movements, as in the bottom board; while columns 2 and 4 are lit following even number of movements, as in the top board. This movement-pattern combinations produce an equally spaced (5.0 mm) grid in both directions.

steps, collecting 6,000 events for each step.

It is worth noticing that although the MDCS hardware can produce a grid pattern in which the LED spots are spaced by only 0.5 mm, in practice a spacing of 5 mm is used. This is because such a spacing is adequate to achieve a resolution better than the intrinsic resolution of the HPD, and allows for scans which can be completed in an acceptable period of time ($\sim$ 3 hrs).

3.4.2 Pattern Recognition and Reconstruction

An algorithm to reconstruct the position of the LED spots has been developed. As mentioned before, the calibration stepping mechanism was used to separate different LED patterns. The reconstruction is run for each calibration step and the algorithm works in three stages:

- Firstly, local maxima on the pixel chip are searched for. An iterative function searches for the absolute maximum within a region of pixels: a pixel is selected if it contains over 1% of the total hits within the HPD; if there is no existing peak within a 2×2 pixel area of the selected pixel, it is stored as a peak candidate.

- Secondly, clusters are created associated with each maximum. As an LED typically illuminates an area covered by 6×6 pixels, a cluster is required to have all hits within the 3×3 pixels immediately surrounding a maximum. In this way the background from "hot" pixels, which are the noisy pixels always producing a hit signal, can be eliminated.

- Finally, the centres-of-gravity of all clusters are calculated. A 2D rotatable Gaussian function is used to fit the position and width of each cluster. A centre-of-gravity mean is also calculated for each cluster as a quality check.

At the end of the reconstruction, a series of histograms and ntuples are produced. The histogram files contain all integrated hit maps for each LED spot. The ntuples contain more detailed information regarding, for example, the (X, Y, Z) position of each LED spot in the

local HPD coordinate, the pixel (column, row) coordinate of the corresponding centre as measured on the HPD anode, the number of photo-electrons etc. This information is then used in the analysis at later steps.

3.4.3   Pattern Filtering

With the chosen calibration pattern, a simple filtering requiring a maximum of one reconstructed peak per HPD is able to reject almost all the TIR peaks. This requirement, however, means that some real light spots also are rejected by the filter. Most commonly these losses occur at the edge of the HPDs and for the HPDs near the edge of the HPD box.

To recover the losses it is necessary to refine the filter by exploiting three major differences between true LED spot and the reflected spots. Firstly, a spot is required to contain at least 40% of the total hits within the HPD. Since a TIR usually gives 3-5 spots, each with similar proportion of hits, most of them will be rejected by this requirement. Secondly, a spot is required to have a width larger than 0.8 pixels. This is because a reflected peak tends to have a narrower structure compared with the ~ 1.4-pixel width from a true LED spot. Finally, the total number of HPDs that record at least one spot must exceed 10 (out of 14). With this the noisy clusters will be rejected.

3.4.4   Extrapolation to HPD Entrance Window

The first step in extracting the correction parameters is to determine the centres of the HPDs. It is known that pixel chip misalignments occurred during the manufacturing process, which means the centres of the 32×32 pixels are not always the centres of the HPDs. The MDCS data allow these offsets to be determined.

For each MDCS calibration scan, the hit map histograms are integrated over all calibration steps. This integration creates a new set of histograms each with an HPD with hits (almost) evenly distributed across its surface. It is not exactly even, due to the TIR effect and the noisy pixels. A cut has to be made, requiring hits in a pixel to be between 10% and
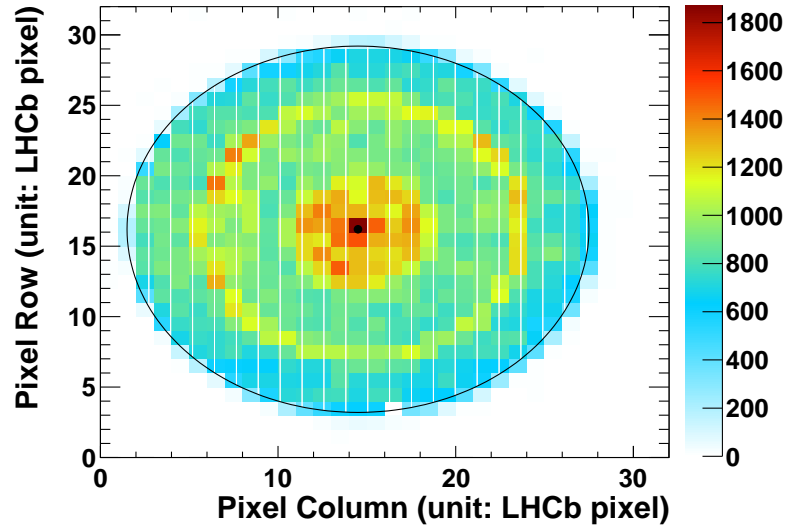
Figure 3.23: An example disc fitted to obtain centre and radius of an HPD image.

80% of the maximum number of hits in one pixel within this HPD. Any pixel passing the cut has an entry of 1. This procedure gives a truly uniform "disc" image of an HPD. The disc is fitted to a circle, thus giving the centre (x, y) of the HPD at the pixel plane and its radius R. An example circular image of the photocathode, projected through the electrostatics onto the pixel chip, is shown in Figure 3.23.

Since the MDCS patterns are projected on the quartz window entrance plane of the HPDs, while the positions of the hits are recorded on the anodes of the HPDs, in order to reconstruct the grid pattern, each anode coordinate has to be extrapolated to a corresponding coordinate on the quartz window entrance plane (Figure 3.24). This involves two steps of conversions. Firstly the inverse-demagnification from anode to photocathode must be performed, and then the refraction correction from the cathode to the outside of the quartz window is made. The magnification value and the refractive index of the quartz window are measured in a dedicated electron-optics study [32]. To perform the magnification from anode to cathode, the following formula is used:

$$R_{\text{cathode}} = c_{11} \times R_{\text{anode}} + c_{12} \times R_{\text{anode}}^2 \tag{3.1}$$
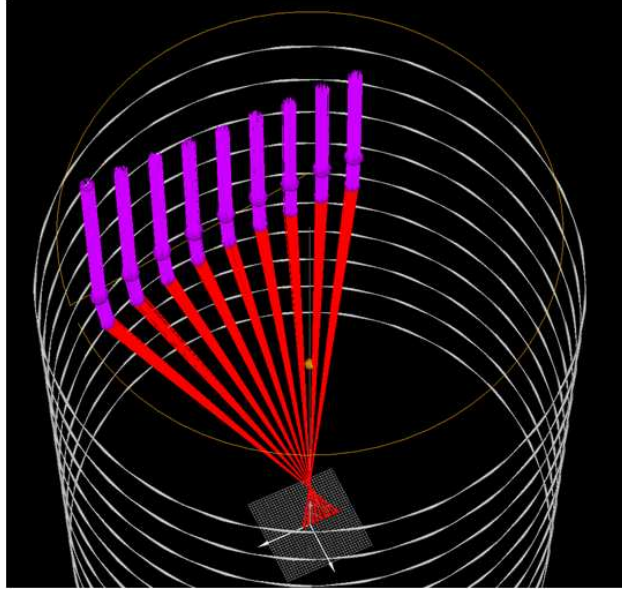
Figure 3.24: The cross focusing feature of the HPD means the position of the photo-electrons detected on the pixel has to be extrapolated back to its entrance position on the photocathode.

where R_{anode} is the distance from the hit position to the centre of the HPD at the pixel plane, i.e. the centre (x, y) determined from the previous disc fitting. R_{cathode} is the distance from the hit position extrapolated to the photocathode, to the centre of the photocathode. c_{11} and c_{12} are parameters determined from the dedicated electron-optics study.

A quadratic function is used to correct for the refraction from the photocathode to the outer surface of the HPD quartz window:

$$R_{\text{outer}} = R_{\text{cathode}} + c_{21} + c_{22} \times R_{\text{cathode}} + c_{23} \times R_{\text{cathode}}^2 \qquad (3.2)$$

where R_{outer} is the distance from the hit position extrapolated to the outer surface of the quartz window to the centre of the quartz window. The values of the parameters are listed in Table 3.2.

When all the light-spot positions are found on the HPD quartz window entrance plane, the grid pattern described in Section 3.4.1 can be seen in the field-off scans.

Table 3.2: Parameters taken from Conditions Database for extrapolating hit positions from anode to the outside of the HPD quartz window [32].

Parameter	Value
c_{11}	5.11
c_{12}	0.01 mm^{-1}
c_{21}	-0.003492 mm
c_{22}	0.03964
c_{23}	-0.0002438 mm^{-1}

3.4.5 Parametrising the Distortion Corrections

The normal trajectories of photo-electrons in an HPD are shown schematically in Figure 2.12. If there is a magnetic field in the volume of the HPD, the photo-electrons will experience an additional term in the Lorentz force:

$$\vec{F} = -e(\vec{E} + \vec{v} \times \vec{B})\tag{3.3}$$

where $\vec{E}$ is the electric field used to cross-focus the photo-electron from photocachode to anode and $\vec{B}$ is the residual magnetic flux density. The resulting distortion depends on the direction and strength of the fields.

In a longitudinal magnetic field $B_\parallel$ parallel to the long axis of the HPD, the distortion has a cylindrical symmetry and the Lorentz force perpendicular to $B_\parallel$ makes the photo-electrons rotate around the centre of the HPD in spiral trajectories. This leads to an "C" shape distortion recorded on the anode (Figure 3.4(a)). With this class of distortion, the amount of rotation is a function of r, where r is the distance between the photo-electron and the centre of the HPD on the pixel plane. The photo-electrons also have small movements outwards from the centre as a function of r.

In contrast, a transverse magnetic field $B_\perp$ perpendicular to the long axis causes a lateral movement to the photo-electrons (Figure 3.4(b)). The value of displacement depends on the emission point of the photo-electron from the cathode as well as the geometry of the

(a)

(b)
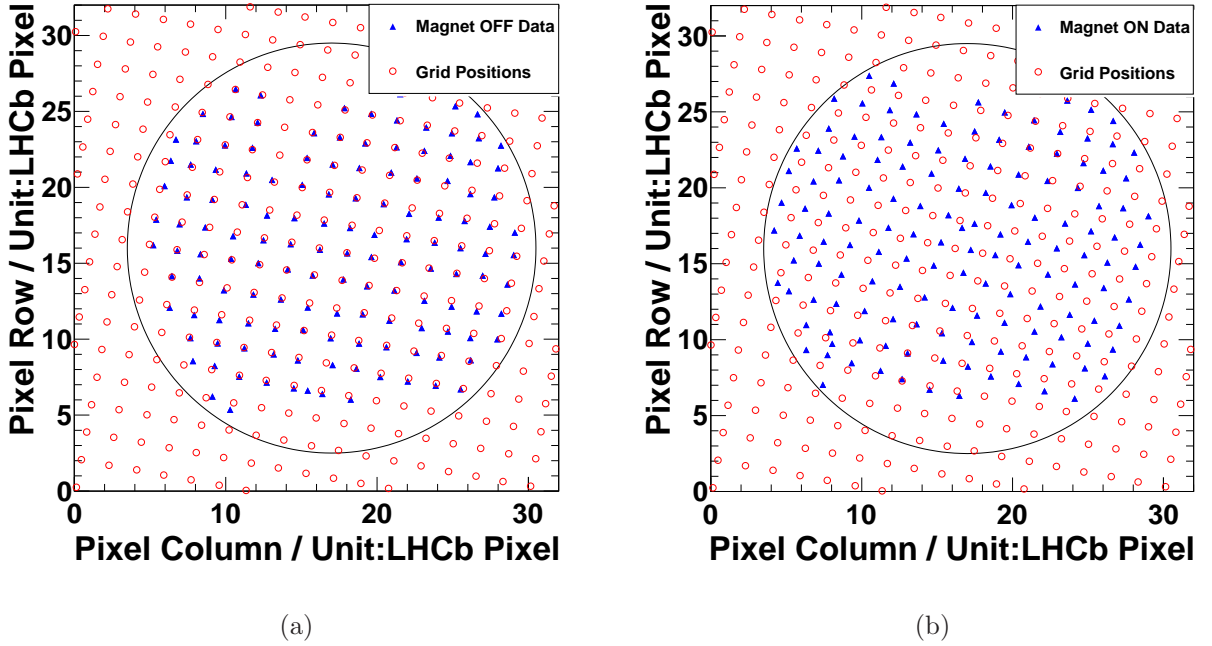
Figure 3.25: A comparison of RICH-1 LED light spot positions in one HPD, in MDCS scans with field off (a) and on (b). Blue triangles: reconstructed LED pattern positions. Red circles: expected calibration grid position. Note that the locations of hits nearer to the edge of the HPD has larger uncertainties and some patterns close to the edge are discarded as they did not pass the pattern filtering criteria, both due to the TIR effect.

electrostatic field. The displacement from $B_\perp$ tends to be much smaller compared with $B_\parallel$ with a same strength. Furthermore, the magnetic shieldings were designed to yield primarily longitudinal field within the volume of the HPD boxes. Therefore the distortion from $B_\perp$ is expected to be small.

The magnetic calibration procedure is performed in dedicated runs with dipole field on and off. The positions of the LED light spots recorded with field off are used as reference points (Figure 3.25(a)). The positions of the patterns recorded in field-on scans (Figure 3.25(b)) are then compared with the reference pattern to evaluate the correction parameters.

The longitudinal and transverse components of the magnetic field are treated separately in the distortion parametrisation, for each individual HPD. The distortion resulting from longitudinal $B_\parallel$ field component is modelled in the polar coordinates as a $3^{\rm rd}$-order polynomial

rotation:

$$\Delta_\phi = a_0 + a_1 r + a_2 r^2 + a_3 r^3, \tag{3.4}$$

plus a 2nd-order polynomial radial expansion:

$$\Delta_r = b_0 + b_1 r + b_2 r^2, \tag{3.5}$$

where r is the radius of a given light-spot with respect to the HPD centre determined in the previous step, while Δ_ϕ, Δ_r are the angular rotation and radial expansion from a field-on spot to its corresponding reference point. a_0 to a_3 and b_0 to b_2 are the correction parameters. The parameters are found by minimisation using MINUIT [33] in ROOT [34]. The quantity in the minimisation is Δ^2, defined as the sum of the square distance between each field-on and field-off spot, as in Equation 3.6.

$$\Delta^2 = \sum_{i=0}^{n_{\text{spots}}} \left\{ \frac{(F(x_{\text{i,on}}) - x_{\text{i,off}})^2}{\sqrt{\sigma^2_{x_{\text{i,on}}} + \sigma^2_{x_{\text{i,off}}}}} + \frac{(F(y_{\text{i,on}}) - y_{\text{i,off}})^2}{\sqrt{\sigma^2_{y_{\text{i,on}}} + \sigma^2_{y_{\text{i,off}}}}} \right\}, \tag{3.6}$$

where the $(x, y)_{\text{i,off}}$ are the coordinates of each light spot i on the pixel detector plane in magnet-off data, with x along the LHCb pixel direction and y along the direction where an LHCb pixel is split into ALICE pixels; while $(x, y)_{\text{i,on}}$ are the corresponding points for field-on data. The $\sigma_{x,y}$ are taken from the widths of the 2D Gaussian fit to each light spot.

The transformation F consists of three steps:

1. Each spot position $(x, y)_{\text{i,on}}$ on the outer surface of the HPD quartz window is converted into polar coordinate $(r, \phi)_{\text{i,on}}$;

2. It then undergoes a transformation described in Equation 3.4 and 3.5;

3. The new position is then converted back to the HPD local coordinates at $(x', y')_{\text{i,on}}$.

The effect from a transverse field with equal strength is much smaller (Figure 3.4(b)) than one from a longitudinal field. Only HPDs closest to the magnetic shielding wall experience visible transverse field distortion effect. The distortion caused by transverse magnetic field manifests itself in two ways:

1. Grid spacing expands in half of the HPD plane and contracts in the other half, or

2. The centre of rotation is shifted away from the HPD disc centre, when the distortion effect is weak.

The first effect is found to be negligible, with the grid spacings remain equal and constant even for the HPDs closest to the magnetic shielding. To a good approximation the distortions from the transverse field can be described as a shift of the centre of rotation away from the HPD image centre, i.e. adding two new parameters x_t and y_t. This means that the light spot positions in polar coordinate becomes (r', ϕ') calculated with respect to the shifted centre of rotation $(x - x_t, y - y_t)$. Therefore transformations in Equation 3.4 and 3.5 become:

$$\Delta_{\phi'} = a_0 + a_1 r' + a_2 r'^2 + a_3 r'^3; \tag{3.7}$$

$$\Delta_{r'} = b_0 + b_1 r' + b_2 r'^2. \tag{3.8}$$

Figure 3.26(a) shows an example distribution of the parameter a_0 in one field-on run. Parameter a_0 is found to be the most dominant correction parameter, with its sign directly related to the direction of the field. It can be seen in Figure 3.26 that the a_0 parameters from the upper system is almost exactly the inverse of those from the lower system, as expected from a near symmetrical field orientation in design. The radial expansion parameter b_0 is shown in Figure 3.26(b). It appears that the radii of most HPD images have little change in the magnetic field. The parameters are demonstrated to be stable over time as shown in Figure 3.27.

(a)   (b)
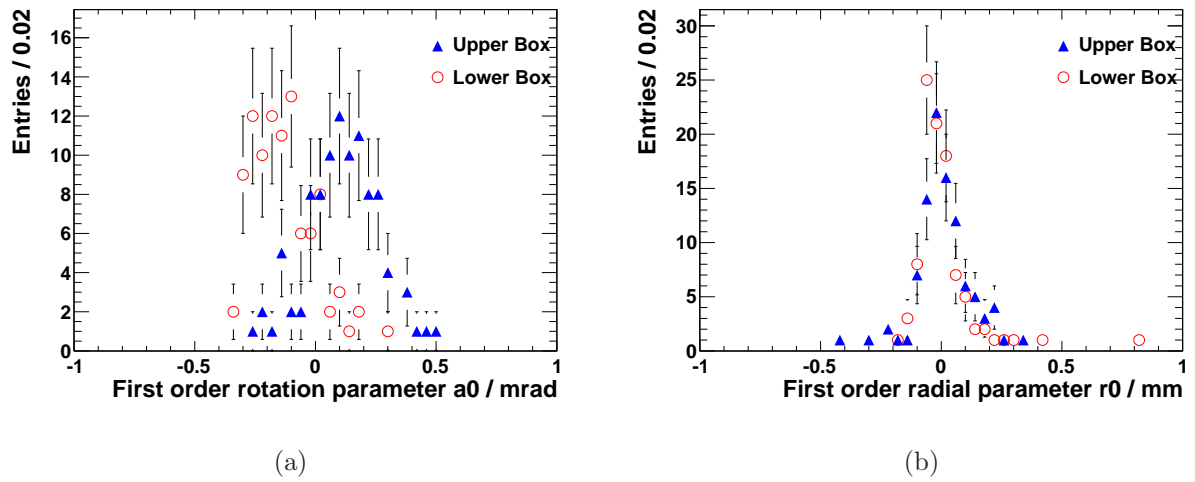
Figure 3.26: The distributions of calibration parameter (a) a0 and (b) r0. The circles show results from the HPDs in the lower system while the triangles show the same from the upper system.
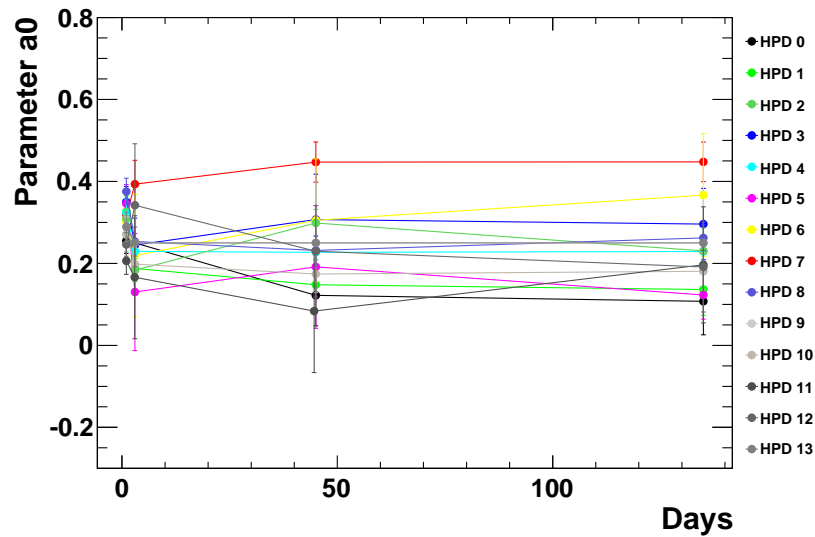
Figure 3.27: The trend of rotational correction parameter a0 for HPDs in Column 4. The horizontal axis shows the amount of time between when different scans were taken. As can be seen from four scans taken over a span of 140 days, the fitted parameters are reasonably stable.

Since the parameter a_0 is found to be the dominant factor from the fit, its distribution is used as an indication of the longitudinal field map within the volumes of each HPD box, as shown in Figure 3.28. The columns are numbered 0 to 7 as it gets further downstream from the interaction point. It can be seen that the $B_\parallel$ component of the field is strongest from HPD Column 2-6, around the centres of the columns. This is as expected from the simulated field distribution in Figure 3.2(b). The amount of distortions on these HPDs are found to be less significant compared with that from the expected 3 mT field in the simulation. This indicates an excellent performance from the magnetic shieldings.

If the magnetic distortion effect is uncalibrated, the residual distances from the field-on LED light-spots to the corresponding field-off LED light-spots is shown in Figure 3.29, where the distribution exhibits a two-peak shoulder structure. This resolution is significantly worse than the intrinsic pixel resolution of the HPDs of 0.72 mm. When the corrections are applied, the resolution improves to 0.51 mm. This value is 25% smaller than the HPD pixel resolution, therefore its contribution to the Cherenkov angle measurement error is very small.

At the end of a magnetic field calibration analysis, all the nine correction parameters (four for rotation and three for radial expansion in longitudinal field, plus two for the shift of rotation centre in the axial field) for each HPD are written to an xml file. The xml file is uploaded to the LHCb Conditions Database. The new database slice can then be used for the reconstruction of the collisions data.

3.4.6   Performance of the Parametrisation on Collision Data

The MDCS correction parameters stored in the Conditions Database were applied in the reconstruction of the 2009 LHC collisions data which was taken with a negative magnetic field configuration. The result is shown in Figure 3.30. The circles show Cherenkov angle resolution after mirror alignment but before the magnetic distortion corrections have been applied. After both mirror alignments and magnetic distortion corrections, the resolution improves from 5.5 mrad to 2.7 mrad, i.e. the MDCS corrections improve the Cherenkov angle resolution by a factor of two.
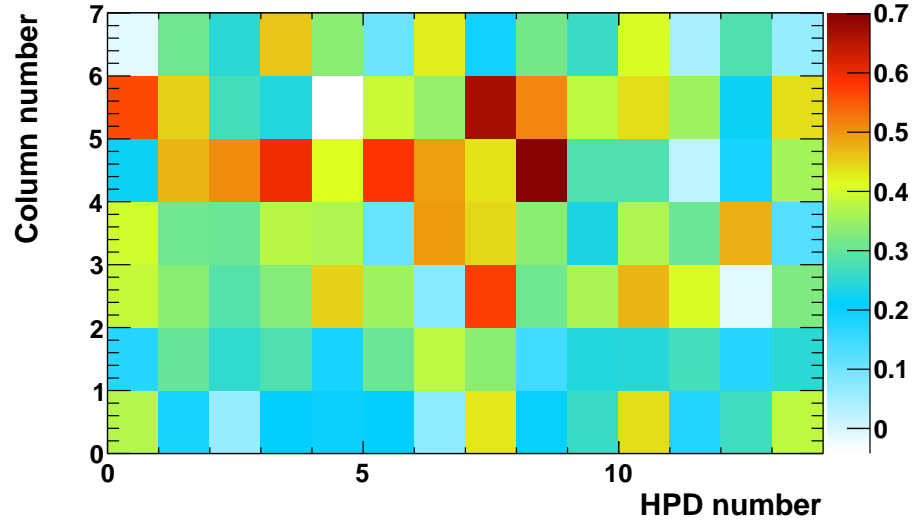
(a)
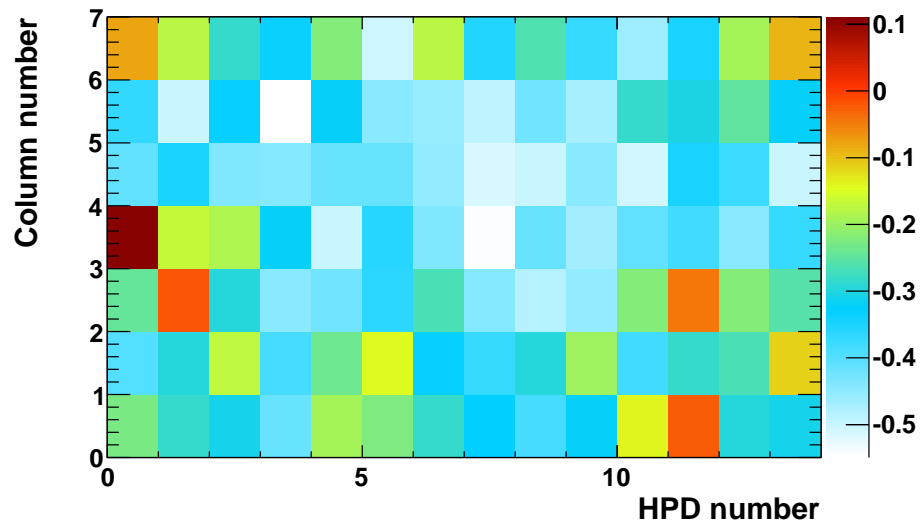
(b)

Figure 3.28: The distribution of calibration parameter a_0 (unit: mrad) provides an indication of the longitudinal field strength for (a) the upper and (b) the lower system. The columns are aligned such that Column 7 is the one located furthest downstream from the interaction point.
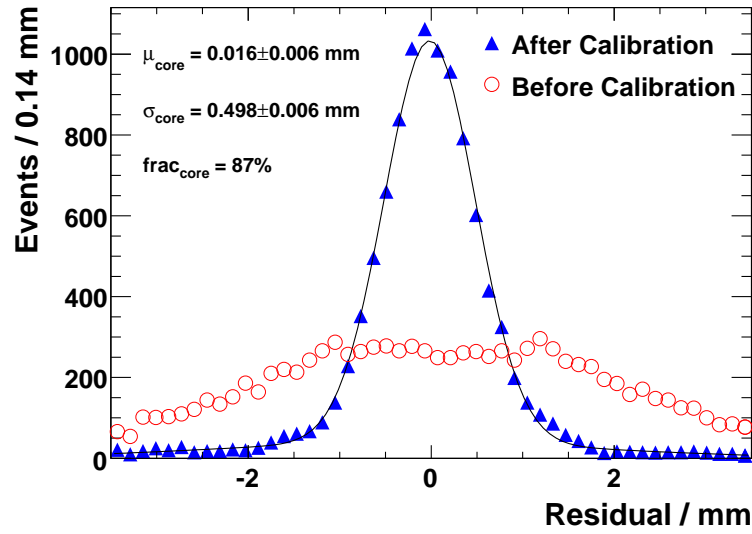
Figure 3.29: The resolution of hit points from the MDCS. Red: before calibration. Blue with fit: after calibration.

In comparison, the benchmark performance from Monte Carlo simulation is 1.55 mrad. The current resolution is still not yet at the Monte Carlo level, but with more data being collected and the understanding of the detector getting better, there is steady progress in improving the resolution. For example, the current mirror alignment procedure only considers the two flat mirrors, one in the upper system and the other in the lower system. As is evident from Figure 3.31(a), after this alignment the resolutions of photons coming from each flat mirror are in good agreement. The four spherical mirrors however, have yet to be individually aligned. In Figure 3.31(b) the data are split into subsets corresponding to light reflected from each of the 4 spherical mirrors. Clear differences are seen, which have not yet been addressed in the alignment. When these spherical mirrors are aligned the Cherenkov angle resolution is expected to improve by at least 0.3 mrad.

The RICH MDCS systems, along with the magnetic shieldings, are already providing significant improvements to the Cherenkov angle resolution in the LHC collisions data. Regular magnetic calibration runs will continue to be performed during the course of LHCb data taking, to provide updated parameters for the data reconstruction.
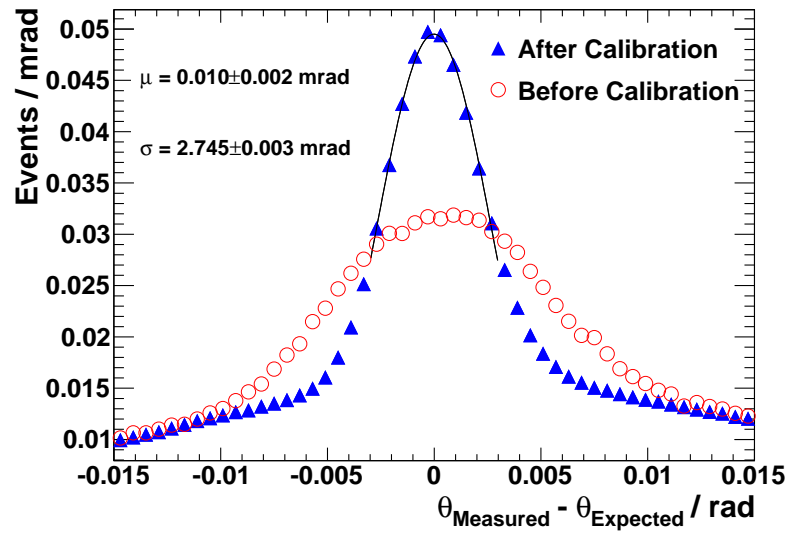
Figure 3.30: A comparison of Cherenkov angle resolution from RICH-1 gas radiator, with and without MDCS corrections.

(a)

(b)
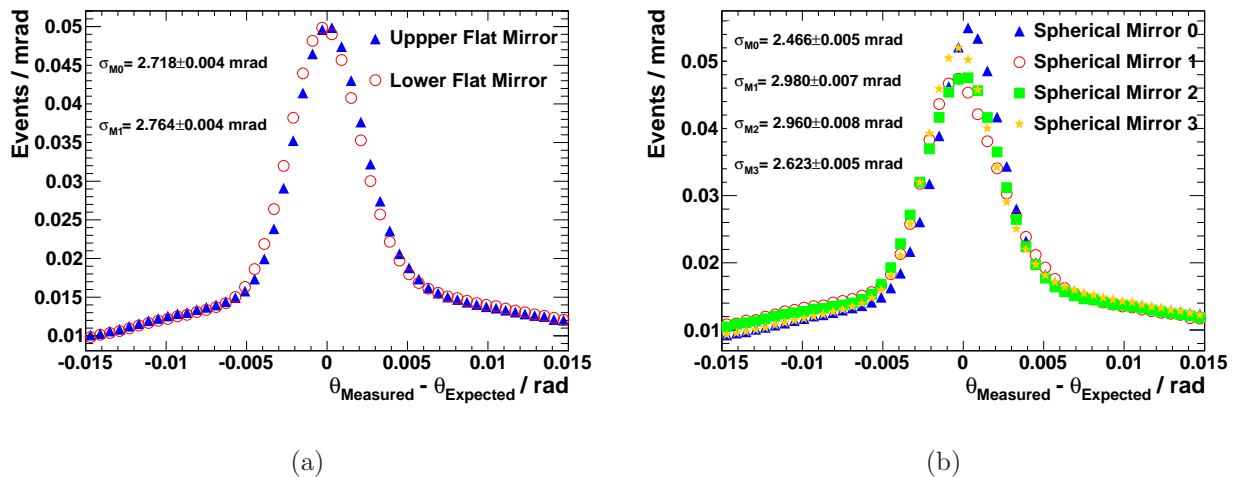
Figure 3.31: Cherenkov angle resolution with 2009 collision data, for hits which have been reflected from specific mirrors: (a) distribution for each flat mirror; (b) distribution for each of the four spherical mirrors.

Chapter 4

$\mathcal{CP}$-Violation in Heavy Flavour Physics

4.1 Introduction

The Standard Model (SM) has been the cornerstone of particle physics for the past forty years. Its account of the physics of subatomic particles and the fundamental interactions has withstood considerable experimental scrutiny, accurately predicting the existence and properties of the Z and W bosons among other successes. One of its biggest triumphs is the prediction of the Higgs Boson, which was first observed recently by ATLAS [35] and CMS [36] experiments at the LHC. Nonetheless, various aspects of the Standard Model remain relatively poorly constrained by experiment, prominent among which is the precise nature of $\mathcal{CP}$ violation.

Although the Standard Model is compatible with $\mathcal{CP}$ violation in all observed hadron transitions, there are reasons to believe that there may exist new physics effects associated with $\mathcal{CP}$ violation in the decays of B, D mesons which are incompatible with the Standard Model that might be observed at a previously inaccessible energy scale. As noted by Sakharov [37], $\mathcal{CP}$ violation is required for baryogenesis under the Big Bang model of the universe, yet the $\mathcal{CP}$ violation allowed under the Standard Model is not sufficient to explain the matter-

antimatter asymmetry observed in the universe today. Another motivation for new physics is the hierarchy problem, in particular the fact that the quantum corrections to the mass of the Higgs boson are divergent at high energies in the Standard Model, whereas the Standard Model Higgs is measured to have a mass of 125 GeV [35] [36]. Therefore, if the Standard Model is valid even at high energies, a "fine tuned" cancellation of these divergent corrections would be needed to keep the mass of the Higgs boson low. Since such a solution is quite unnatural, there is good reason to expect new physics effects (e.g. Super Symmetry) to appear at TeV energy scales, which would remove the need this "fine-tuning". Such physics need not be $\mathcal{CP}$ conserving, or transform under $\mathcal{CP}$ in the same manner as the Standard Model. By the same argument, failing to observe any new physics at the TeV scale could be indicative of a new fundamental symmetry responsible for the low Higgs mass.

Charm, after strange and beauty, is the last system of heavy flavoured mesons where $\mathcal{CP}$ violation remains to be discovered. Neutral B mesons are characterised by their splitting in mass between the mass eigenstates, leading to fast oscillations; while the neutral kaon's splitting in width between the mass eigenstates results in a short-lived and long-lived state. These splittings will be explained in details in Section 4.3. In comparison, neutral charm mesons have very small splittings in both mass and width. For charm, compared to the beauty sector, this leads to rather subtle mixing-related effects in time-dependent as well as time-integrated charm measurements.

Since this thesis is concerned with studying the decays of D mesons, an overview of the theory of D meson propagation, mixing, and decay will lay the groundwork for the subsequent analysis. Natural units ($h = c = 1$) are used throughout this chapter.

4.2   Symmetries in Particle Physics

One of the most fundamental principles in physics is the connection between conservation laws and symmetries of nature. Noether's theorem [38] shows that if a physical system is invariant under a continuous transformation, there exists an associated conserved quantity;

the conservation of energy follows from the invariance of physical laws under translations in time, the conservation of momentum follows from invariance under translations in space, and angular momentum is conserved because the laws of physics are invariant under spatial rotations. Unlike continuous symmetries, discrete symmetries, such as parity transformation, are found to be broken in certain physical interactions. For particle physics, the relevant discrete symmetries are:

- $\mathcal{C}$: charge conjugation changes the sign of all additive quantum numbers. With specific reference to the decay of a sub-atomic particle, charge conjugation consists of swapping every particle in the decay for its antiparticle.

- $\mathcal{P}$: parity is the operation of reflection in the three spatial axes, i.e. (x, y, z) → (-x, -y, -z).

- $\mathcal{T}$: the time reversal operator reverses the direction of motion by reflection in the time axis.

Although each of these three discrete symmetries is broken in weak interactions, the combined symmetry $\mathcal{CPT}$ is an exact symmetry in any local Lagrangian field theory.

4.2.1   Observations of Symmetry Violation

Although most interactions are invariant under each of the $\mathcal{C}$, $\mathcal{P}$, and $\mathcal{T}$ symmetry transformations, it has long been known that weak interactions violate both $\mathcal{C}$ and $\mathcal{P}$ symmetry [39]. $\mathcal{CP}$ violation was first observed in the neutral kaon system [40], and has more recently been seen in the B system as well [41][42]. Invariance under CPT is a requirement of all relativistic field theories, and is constrained to $< 10^{-18}$ from measurements of the $K^0\overline{K^0}$ mass difference [43].

Both $\mathcal{C}$ and $\mathcal{P}$ are conserved by the electromagnetic and strong interactions but not by the weak interaction. Parity violation in the weak interaction was demonstrated by Wu *et al* in 1956 [44] in nuclear beta decay and in pion decays [45], after the suggestion by Lee

and Yang [39]. Non conservation of $\mathcal{C}$ is a direct consequence of $\mathcal{P}$ violation as argued by Lee, Oehme and Yang [46]. After the establishment of $\mathcal{P}$ and $\mathcal{C}$ violation, the combined symmetry $\mathcal{CP}$ was considered to be conserved in nature [47], until another experiment found otherwise. In 1964, Cronin and Fitch demonstrated $\mathcal{CP}$ violation in weak interactions, by studying the decays of neutral kaons into pions [48]. The K_L^0 meson was thought to be $\mathcal{CP}$ odd and therefore should not decay to two pion final states if $\mathcal{CP}$ is conserved. Cronin and Fitch observed the decay $K_L^0 \to \pi^+\pi^-$, which is a $\mathcal{CP}$ even final state, providing evidence for $\mathcal{CP}$ violation. Nevertheless, this $\mathcal{CP}$ violation is small, and only about 1 in 500 K_L^0 will decay into two pions. $\mathcal{CP}$ violation in the decays of neutral kaons is enabled by a phenomenon called "mixing", which will be explained in more detail below.

Since the original measurement of Cronin and Fitch, $\mathcal{CP}$ violation has also been observed in B mesons, particles containing b quarks, and extensive experimental and theoretical work has taken place to qualify and quantify this effect. While $\mathcal{CP}$ violation in the kaon system led to many insights into this entirely new phenomenon, B mesons offer a richer ground due to their larger mass. Many more interesting final states are possible in B meson decays as compared to kaons, and therefore, have been the focus of not only the "e^-e^+" B factories but also the Tevatron experiments. The LHCb experiment is built specifically to study the decays of B and D mesons. In the rest of this chapter, the $\mathcal{CP}$ violation formalism will be described in some detail.

4.3 Neutral Meson Oscillation (Mixing) Formalism

For a generic neutral meson M^0, the $\mathcal{CP}$ operator is related to the flavour eigenstates as follows:

$$CP|M^0\rangle = |\overline{M^0}\rangle, \qquad CP|\overline{M^0}\rangle = |M^0\rangle, \tag{4.1}$$

so the $\mathcal{CP}$ eigenstates can be constructed as

$$M_+ = |M^0\rangle + |\overline{M^0}\rangle, \qquad M_- = |M^0\rangle - |\overline{M^0}\rangle. \tag{4.2}$$

Then the flavour eigenstates can be written in terms of $\mathcal{CP}$ eigenstates as

$$M^0 = \frac{1}{\sqrt{2}}(|M_+\rangle + |M_-\rangle), \qquad \overline{M^0} = \frac{1}{\sqrt{2}}(|M_+\rangle - |M_-\rangle) \qquad (4.3)$$

where the factor $\frac{1}{\sqrt{2}}$ is for normalisation. Now consider the time evolution of the flavour eigenstates

$$i\frac{d}{dt}\psi = \mathcal{H}\psi, \qquad \mathcal{H}\psi = \begin{pmatrix} M^0 \\ \overline{M^0} \end{pmatrix} \qquad (4.4)$$

where $\mathcal{H}$ is the Hamiltonian, and can be written as the combination of two hermitian matrices $\mathcal{M}$ and Γ as

$$\mathcal{H} = \mathcal{M} - \frac{i}{2}\Gamma = \begin{pmatrix} M_{11} - \frac{i}{2}\Gamma_{11} & M_{12} - \frac{i}{2}\Gamma_{12} \\ M_{21} - \frac{i}{2}\Gamma_{21} & M_{22} - \frac{i}{2}\Gamma_{22} \end{pmatrix}. \qquad (4.5)$$

$\mathcal{CPT}$ invariance requires the masses and the decay rate of particles and anti-particles to be equal. For this to be true, the diagonal elements of $\mathcal{H}$ should be equal, i.e. $\mathcal{H}_{11} = \mathcal{H}_{22}$, and the hermiticity of $\mathcal{M}$ and Γ implies $\mathcal{H}_{21} = \mathcal{M}_{12}^* - \frac{i}{2}\Gamma_{12}^*$. The ψ is not an eigenstate of the above Hamiltonian, but its eigenstates can be constructed by combining the two flavour eigenstates M^0 and $\overline{M^0}$. The physical states, which are denoted by H and L for "heavy" and "light", can then be written as

$$\mathcal{H}|M_{H,L}\rangle = \left(m_{H,L} - \frac{i}{2}\Gamma_{H,L} \right) |M_{H,L}\rangle, \qquad (4.6)$$

where the states H and L have distinct masses and decay widths. The mass and decay width difference between them, and the average decay width Γ are defined as

$$\Delta m \equiv m_H - m_L, \qquad \Delta\Gamma \equiv \Gamma_H - \Gamma_L, \qquad \Gamma \equiv \frac{1}{2}(\Gamma_H + \Gamma_L). \qquad (4.7)$$

The mixing parameters x, y are defined as

$$x \equiv \frac{\Delta m}{\Gamma}, \qquad y \equiv \frac{\Delta\Gamma}{2\Gamma}. \qquad (4.8)$$
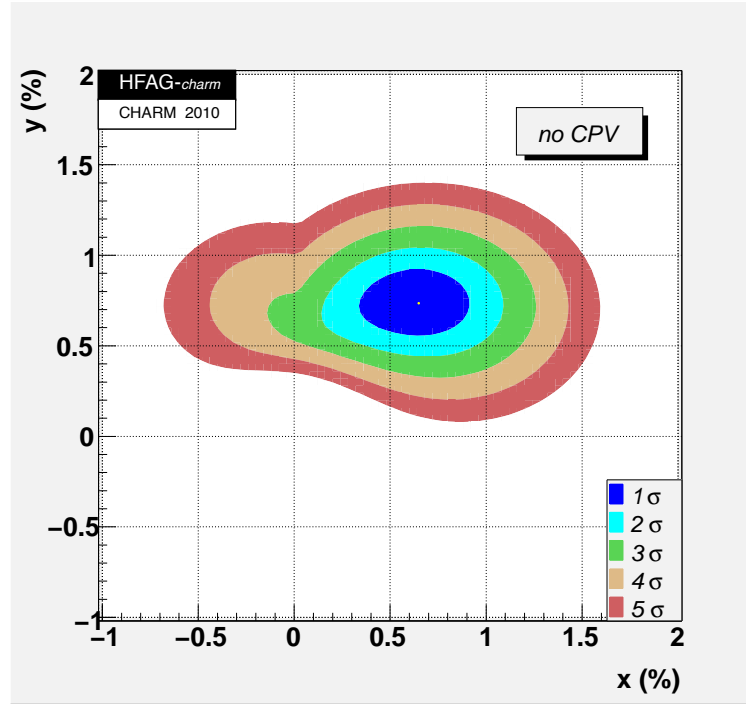
Figure 4.1: World average values of mixing parameters x and y.

The world average values of x, y in the neutral D meson system are combined by the Heavy Flavour Averaging Group (HFAG) [49]:

$$x = (0.65 \pm 0.18)\% \tag{4.9}$$

$$y = (0.74 \pm 0.12)\%, \tag{4.10}$$

with the contour plot shown in Fig 4.1. The no-mixing point at $(0, 0)$ is excluded at 10.2σ. This shows mixing has been observed in the neutral D system, albeit at a much slower rate than that in the neutral B system.

The time evolution of the physical states is given by

$$|M_{H,L}(t)\rangle = e^{-im_{H,L}t} \cdot e^{-\frac{\Gamma_{H,L}}{2}t}|M_{H,L}(0)\rangle \tag{4.11}$$

and their expressions in terms of the flavour eigenstates is

$$|M_H\rangle = p|M^0\rangle + q|\overline{M^0}\rangle, \qquad |M_L\rangle = p|M^0\rangle - q|\overline{M^0}\rangle. \tag{4.12}$$

which in the neutral D system correspond to

$$
\begin{aligned}
|D_H\rangle &= p|D^0\rangle + q|\overline{D}^0\rangle, \\
|D_L\rangle &= p|D^0\rangle - q|\overline{D}^0\rangle.
\end{aligned} \tag{4.13}
$$

Note here that while the flavour and $\mathcal{CP}$ eigenstates are orthogonal:

$$
\langle M^0|\overline{M^0}\rangle = 0, \qquad \langle M_+|M_-\rangle = 0, \tag{4.14}
$$

the physical states are in general not orthogonal:

$$
\langle M_H|M_L\rangle = p*q - q*p = \varepsilon. \tag{4.15}
$$

Therefore, if $\mathcal{CP}$ symmetry is to hold, it is required that $|p/q| = 1$, i.e. the physical mass eigenstates coincide with the $\mathcal{CP}$ eigenstates. $\mathcal{CP}$ violations are possible even in the case $|p/q| = 1$ and this will be discussed in Section 4.4.2 and 4.4.3.

4.4 Types of $\mathcal{CP}$-Violation

4.4.1 Indirect $\mathcal{CP}$-Violation

Indirect $\mathcal{CP}$ violation, or $\mathcal{CP}$ violation in mixing, occurs when $|p/q| \neq 1$ and the mass eigenstates become mixtures of the $\mathcal{CP}$ eigenstates. It was historically the first type of $\mathcal{CP}$ violation to be discovered by Cronin and Fitch in neutral kaons and in this system is at the level of $|p/q| - 1 = 3 \times 10^{-3}$ [48]. Indirect $\mathcal{CP}$ violation in the D system is a difficult observation to make due to the very small mixing as shown by the measured x, y values, and the small lifetime difference between the states. The Standard Model also predicts this to be very small. In the B system, indirect $\mathcal{CP}$ violation is also negligibly small since Γ_{12}/M_{12} is approximately real and $|q/p| \approx 1$.

4.4.2 Direct $\mathcal{CP}$-Violation

Direct $\mathcal{CP}$ violation, or $\mathcal{CP}$ violation in decay, occurs when the decay amplitude for a meson M to a final state f differs from the $\mathcal{CP}$-conjugate decay amplitude. Neglecting the phase, then a set of intermediate amplitudes contributing to a final state f each enter with a $\mathcal{CP}$-conserving strong phase and a weak phase. Since the weak phases change sign under $\mathcal{CP}$ conjugation, then if at least two amplitudes with differing weak phases enter into the total decay amplitude, the interference between them leads to $\mathcal{CP}$ violation. In the neutral kaon sector, direct $\mathcal{CP}$ violation is an even smaller effect than indirect $\mathcal{CP}$ violation, and is at the level of 10^{-5}. Direct $\mathcal{CP}$ violation is also the only way for $\mathcal{CP}$ violation to occur in charged hadron decays.

As this analysis does not involve direct CP violation search, this type of violation will not be discussed further in this thesis.

4.4.3 $\mathcal{CP}$-Violation in the Interference of Mixing and Decay

For final states that can be reached by both M^0 and $\overline{M^0}$, $\mathcal{CP}$ violation can occur in the interference between mixing and decay amplitudes. It occurs due to the fact that such a meson can either decay directly to a final state or can oscillate to its conjugate state which then decays to the same final state. Even with vanishing direct and indirect $\mathcal{CP}$ violation, an interfering phase between mixing and decay can lead to observations, i.e. when

$$\Im\left(\frac{q}{p}\frac{\overline{A_f}}{A_f}\right) \neq 0, \tag{4.16}$$

where A_f is the decay amplitude of final state f. This type of $\mathcal{CP}$ violation has been measured by BaBar [50], BELLE [51], CDF [52] and LHCb [53].

4.5 $\mathcal{CP}$-Violation in the Standard Model

The $\mathcal{C}$ and $\mathcal{P}$ symmetries are preserved naturally in many gauge theories, notably massless Quantum Chromodynamics (QCD) and Quantum Electrodynamics (QED), and even theories that are explicitly designed to violate parity are still $\mathcal{CP}$ invariant. For example the chiral gauge theory whose Lagrangian

$$\mathcal{L} = -\frac{1}{4}F_{\mu v}F^{\mu v} + \overline{\psi_L}i\sigma D\psi_L \tag{4.17}$$

only allows left-handed Weyl fermions, ψ_L, to interact with the gauge bosons, as the right-handed Weyl fermions are sterile, is $\mathcal{CP}$ invariant. This implies that $\mathcal{CP}$ is a natural symmetry of massless gauge theories and it is only possible to introduce $\mathcal{CP}$-violation into theories where mass has been introduced [54].

The Higgs mechanism of the Standard Model introduces a scalar field which couples to the fermion fields and gauge boson fields. The scalar (Higgs) sector generates a non-zero vacuum expectation value which spontaneously breaks gauge invariance producing the mass terms. The Lagrangian of the Standard Model is then written as

$$\mathcal{L} = \mathcal{L}_{gauge}(\psi_L, \psi_R, W, \phi) + \mathcal{L}_{Higgs}(\phi) + \mathcal{L}_{Yukawa}(\psi_L, \psi_R, \phi) \tag{4.18}$$

where the first term, $\mathcal{L}_{gauge}$, is the kinetic term of the fields involved, i.e. the left- and right-handed fermion fields ψ_L and ψ_R, the gauge bosons W, and the scalar Higgs field ϕ, as well as their gauge interactions. The second term, $\mathcal{L}_{Higgs}$, is the potential felt by the scalar fields, it is responsible for the non-zero value of the vacuum expectation value and gives rise to spontaneous symmetry breaking. The third and final term $\mathcal{L}_{Yukawa}$, describes the interaction between the fermoinic and scalar fields, which after spontaneous symmetry breaking generates the fermion mass terms. In the Standard Model the gauge and Higgs terms are automatically $\mathcal{CP}$-invariant and it is therefore the Yukawa sector which must be

the source of $\mathcal{CP}$-violation. The Yukawa term is

$$\mathcal{L}_{Yukawa} = -\lambda_{ij}^d \overline{Q_L^i} \cdot \Phi d_R^j - (\lambda_{ij}^d)^* \overline{d_R^j} \Phi^\dagger \cdot Q_L^i + \ldots \tag{4.19}$$

where the i, j indices are generation labels, Q_L^i is the SU(2)$_L$ quark doublet, (u_L^i, d_L^i), Φ represents the Higgs doublet, (ϕ^+, ϕ^0) and the ... represents the up-type quarks. After a $\mathcal{CP}$ transformation the left (L) and right (R) indices, and the particle and anti-particle indices, are exchanged, resulting in

$$\mathcal{CP} : \overline{Q_L^i} \cdot \Phi d_R^j \rightarrow \overline{d_R^j} \Phi^\dagger \cdot Q_L^i. \tag{4.20}$$

Therefore, for $\mathcal{L}_{Yukawa}$ to be $\mathcal{CP}$ invariant it is necessary that $\lambda_{ij}^d = (\lambda_{ij}^d)^*$, i.e. that lambda is real. If lambda is complex then there is $\mathcal{CP}$ violation. $\mathcal{CP}$-violation takes place in the scalar sector of the Standard Model and is introduced through complex Yukawa couplings.

In the SM, with three generations, the Yukawa couplings form a 3×3 mass matrix for the up and down type quarks, u_i^{weak} and d_i^{weak} respectively, which are eigenstates of the weak interaction. By diagonalising these matrices into the basis of the mass eigenstates rotating matrices U^{u,d} are defined as

$$u_i^{weak} = U_{ij}^u u_j^{mass} \qquad and \qquad d_i^{weak} = U_{ij}^d d_j^{mass}. \tag{4.21}$$

Neutral weak interactions are unaffected as the transformation is unitary, but charged weak iterations are:

$$\text{Neutral}: \quad \overline{u}_i^{weak} u_i^{weak} \quad \equiv \quad \overline{u}_i^{mass} u_i^{mass} \tag{4.22}$$

$$\text{Charged}: \quad \overline{u}_i^{weak} d_i^{weak} \quad \rightarrow \quad \overline{u}_i^{mass} (U^u)^\dagger U^d d_i^{mass}. \tag{4.23}$$

The unitary matrix, V$_{\text{CKM}} \equiv (\text{U}^u)^\dagger \text{U}^d$, provides the strength of the couplings between the up and down type quarks. This matrix is known as the Cabibbo-Kobayashi-Maskawa (CKM) matrix and it provides a complex phase which is the source of $\mathcal{CP}$-violation in the Standard Model [55].

4.6   The CKM Matrix

The CKM matrix V_{CKM} is a 3×3 $\mathcal{CP}$-violating matrix. The elements of the matrix, V_{ij}, represent the strength of the coupling between an up and a down type quark under the charged weak interaction. The CKM matrix is defined as

$$V_{\text{CKM}} = \begin{pmatrix} V_{ud} & V_{us} & V_{ub} \\ V_{cd} & V_{cs} & V_{cb} \\ V_{td} & V_{ts} & V_{tb} \end{pmatrix}, \tag{4.24}$$

and the equivalent matrix for the anti-quark couplings is defined by the complex conjugate of the CKM matrix elements, V_{ij}^*.

The CKM matrix can be parametrised by three Euler angles of rotation and six complex phases, as it is a 3×3 unitary matrix. The quark fields of the Standard Model Lagrangian are invariant under rotations of the form $q \to qe^{i\phi}$ and five of the complex phases are "rotated away" by a redefinition the quark fields [54]. The remaining physical phase is the source of $\mathcal{CP}$-violation in the Standard Model and is an inevitable consequence of there being three generations of quarks. The three Euler angles and the complex phase must be measured by experiment and are fundamental constants of nature. The Chau-Keung mixing angle representation [56] has become the convention for the expression of the CKM matrix in terms of the three mixing angles $\theta_{12}, \theta_{13}, \theta_{23}$, and the complex phase δ,

$$\begin{aligned} V_{\text{CKM}} &= \begin{pmatrix} 1 & 0 & 0 \\ 0 & c_{23} & s_{23} \\ 0 & -s_{23} & c_{23} \end{pmatrix} \begin{pmatrix} c_{13} & 0 & s_{13}e^{-i\delta} \\ 0 & 1 & 0 \\ -s_{13}e^{-i\delta} & 0 & c_{13} \end{pmatrix} \begin{pmatrix} c_{12} & s_{12} & 0 \\ -s_{12} & c_{12} & 0 \\ 0 & 0 & 1 \end{pmatrix} \tag{4.25} \\[2mm] &= \begin{pmatrix} c_{12}c_{13} & s_{12}c_{13}s_{13}e^{-i\delta} & 0 \\ -s_{12}c_{23} - c_{12}s_{23}s_{13}e^{i\delta} & c_{12}c_{23} - s_{12}s_{23}s_{13}e^{i\delta} & s_{23}c_{13} \\ s_{12}c_{23} - c_{12}s_{23}s_{13}e^{i\delta} & -c_{12}c_{23} - s_{12}s_{23}s_{13}e^{i\delta} & c_{23}c_{13} \end{pmatrix} \tag{4.26} \end{aligned}$$

where $c_{ij} = cos(\theta_{ij})$ and $s_{ij} = sin(\theta_{ij})$. The Chau-Keung formalisation shows the extension from two generations to three.

A popular approximate parametrisation of the CKM matrix is the Wolfenstein parametrisation [57] which is based on the strength of the couplings. This allows the hierarchy of the quark strengths to be clearly expressed. The Wolfenstein parametrisation defines four independent parameters

$$\lambda \equiv s_{12} \equiv sin(\theta_c), \qquad A \equiv \frac{s_{23}}{s_{12}^2}, \qquad \rho \equiv \frac{s_{13}cos(\delta)}{s_{12}s_{23}} \qquad \text{and} \qquad \eta \equiv \frac{s_{13}sin(\delta)}{s_{12}s_{23}} \tag{4.27}$$

where θ_c is the Cabibbo angle. The CKM matrix expressed in terms of λ is given by

$$\mathrm{V}_{\mathrm{CKM}}^{(3)} = \begin{pmatrix} 1 - \frac{1}{2}\lambda^2 & \lambda & A\lambda^3(\rho - i\eta) \\ -\lambda & 1 - \frac{1}{2}\lambda^2 & A\lambda^2 \\ A\lambda^3(1 - \rho - i\eta) & -A\lambda^2 & 1 \end{pmatrix} + \mathcal{O}(\lambda^4) \tag{4.28}$$

to order λ^3. The four parameters of the CKM matrix are free parameters in the SM and have been determined experimentally [58] to be:

$$\lambda \simeq 0.22, \qquad A \simeq 0.81, \qquad \rho \simeq 0.14 \qquad \text{and} \qquad \eta \simeq 0.35. \tag{4.29}$$

4.7   Experimental Measurements of $\mathcal{CP}$-Violation in the Neutral D System

The possible $\mathcal{CP}$-violating tree-level two-body D^0 decays into two charged pseudoscalar mesons can be split in three categories:

- **Cabibbo-Favoured** (CF): $D^0 \rightarrow K^-\pi^+$, whose decay amplitude only involves couplings within a generation;

- **Singly Cabibbo-Suppressed** (SCS): $D^0 \to K^+K^-$ and $D^0 \to \pi^+\pi^-$, where a factor of λ is present in the decay amplitude;

- **Doubly Cabibbo-Suppressed** (DCS): $D^0 \to K^+\pi^-$, where a factor of λ^2 is present in the decay amplitude.

The same applies to the charge conjugate decays.

The tree level graphs for the three decays are shown in Fig. 4.2. Besides the direct tree level decay, the DCS final state can also be reached by oscillation of the D^0 into a $\overline{D}^0$ followed by a CF decay. The final states of the SCS modes are $\mathcal{CP}$ eigenstates with eigenvalues 1.This is exploited in the search for mixing and $\mathcal{CP}$ violation.

The SM predicts very small $\mathcal{CP}$ asymmetries in charm transitions. Observing a level of $\mathcal{CP}$ violation that significantly deviate from the SM prediction would establish the intervention of New Physics. Due to $\mathcal{CPT}$ invariance, $\mathcal{CP}$ violation can be implemented only through a complex phase in some effective couplings. For it to become observable two different, yet coherent amplitudes have to contribute to an observable. One way to probe the observables is to look for decays to final states that are $\mathcal{CP}$ eigenstates, e.g. $D^0 \to K^+K^-, \pi^+\pi^-$.

The Wolfenstein representation of the CKM matrix reveals one of the best pieces of evidence that the SM is incomplete [59]. On a practical level it shows that up to higher order in λ, mixing with the third family induces only an imaginary part for the charged current couplings of charm with light quarks. The most relevant source for $\mathcal{CP}$ violation is the phase in V_{cs}, where

$$V_{cs} \simeq \eta A^2 \lambda^4 \simeq \eta |V_{cb}|^2 \sim 10^{-3} \tag{4.30}$$

which provides a very rough benchmark number for the level of $\mathcal{CP}$ asymmetry for charm transitions in the SM.

New physics effects can manifest themselves in two ways in the SCS decays. The short range process of $D^0 - \overline{D}^0$ mixing is governed by the box-diagrams as shown in Figure 4.3. The SCS decay can also proceed through a penguin diagram, as illustrated in Figure 4.4. In
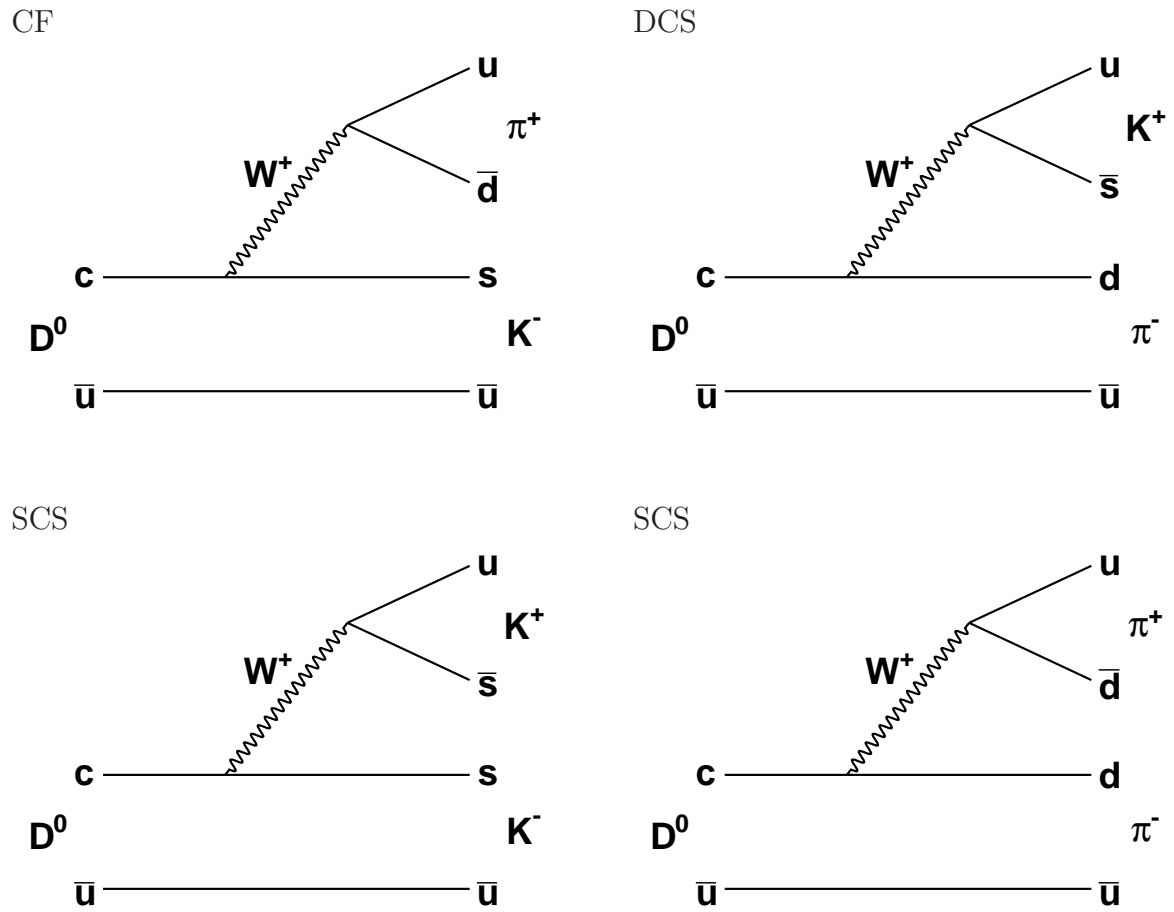
Figure 4.2: Tree level Feynman graphs of $D \to hh$ decays. The two decays into $K\,\pi$ are shown on top and the two decays into $\mathcal{CP}$ eigenstates are shown below.
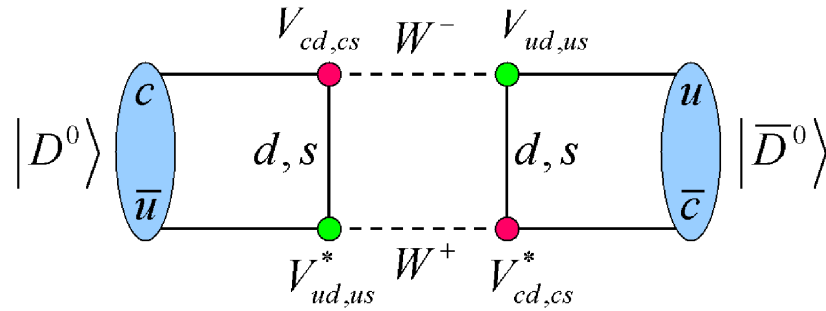
Figure 4.3: Box diagram of D^0-$\bar{D}^0$ mixing. It governs the short range process of D^0-$\bar{D}^0$ mixing.
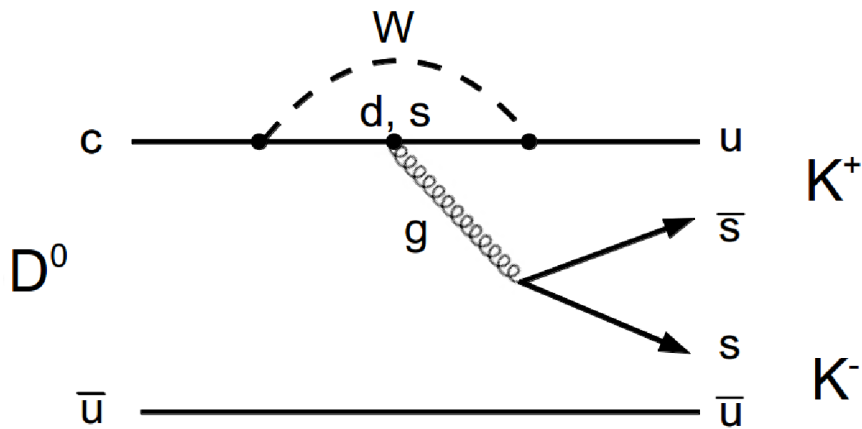
Figure 4.4: Penguin diagram of a D^0 SCS decay. The virtual loops allows for contribution from new physics particles.

both cases, new physics particles can enter the virtual loops, which results in couplings that is different from the SM's. These contributions can lead to levels of mixing and $\mathcal{CP}$ violation that are significantly different from the SM benchmark.

Using the experimental information on the smallness of x and y one can expand the time evolution of charm decays in these variables. With the assumption of no direct $\mathcal{CP}$ violation

in D^0 to two-body decays, the time evolution of these decays can be written [60] as

$$\Gamma[D^0(t) \rightarrow K^+K^-] = e^{-\Gamma t}|A_{K^-K^+}|^2[1 - R_m(y\cos\phi - x\sin\phi)\Gamma t], \tag{4.31}$$

$$\Gamma[\overline{D}^0(t) \rightarrow K^+K^-] = e^{-\Gamma t}|A_{K^-K^+}|^2[1 - R_m^{-1}(y\cos\phi + x\sin\phi)\Gamma t], \tag{4.32}$$

$$\Gamma[D^0(t) \rightarrow K^-\pi^+] = \Gamma\left[\overline{D}^0(t) \rightarrow K^+\pi^-\right] = e^{-\Gamma t}|A_{K^-\pi^+}|^2, \tag{4.33}$$

$$\Gamma[D^0(t) \rightarrow K^+\pi^-] = e^{-\Gamma t}|A_{K^-\pi^+}|^2$$
$$\times \left[R_D + \sqrt{R_D}R_m(y'\cos\phi - x'\sin\phi)\Gamma t + \frac{R_m^2}{4}(y'^2 + x'^2)(\Gamma t)^2\right], \tag{4.34}$$

$$\Gamma[\overline{D}^0(t) \rightarrow K^-\pi^+] = e^{-\Gamma t}|A_{K^-\pi^+}|^2$$
$$\times \left[R_D + \sqrt{R_D}R_m^{-1}(y'\cos\phi + x'\sin\phi)\Gamma t + \frac{R_m^{-2}}{4}(y'^2 + x'^2)(\Gamma t)^2\right], \tag{4.35}$$

which uses the following parametrisations

$$|q/p| = R_m, \tag{4.36}$$

$$\lambda_{K^+\pi^-}^{-1} = \sqrt{R_D}R_m^{-1}e^{-i(\delta+\phi)}, \tag{4.37}$$

$$\lambda_{K^-\pi^+} = \sqrt{R_D}R_m e^{-i(\delta-\phi)}, \tag{4.38}$$

$$\lambda_{K^-K^+} = -R_m e^{-i\phi}, \tag{4.39}$$

where $\lambda_f \equiv \frac{q}{p}\frac{\overline{A}_f}{A_f}$, $A_f \equiv \langle f|\mathcal{H}_d|D^0\rangle$ and $\overline{A}_f \equiv \langle f|\mathcal{H}_d|\overline{D}^0\rangle$. R_D is the ratio of the rates of the DCS to the CF decay. The mixing parameters x', and y' are related to x, y through the strong phase difference δ between the CF and the DCS decay amplitudes:

$$x' \equiv x\cos\delta + y\sin\delta, \tag{4.40}$$

$$y' \equiv y\cos\delta - x\sin\delta. \tag{4.41}$$

The measurement by CLEO [61] indicates a small strong phase difference of

$$\cos(\delta) = 1.03^{+0.31}_{-0.17}(\text{stat}) \pm 0.06(\text{sys}). \tag{4.42}$$

ϕ is the $\mathcal{CP}$ violating relative phase between q/p and $\overline{A}_f/A_f$. The phase convention of ϕ is chosen such that, in the limit of no $\mathcal{CP}$ violation, $\mathcal{CP}|D^0\rangle = -|\overline{D}^0\rangle$. In this convention $\mathcal{CP}$ conservation leads to $\phi = 0$.

Indirect $\mathcal{CP}$ violation comprises $\mathcal{CP}$ violation through a non-zero phase ϕ and a non-zero $\mathcal{CP}$ asymmetry A_m, where

$$A_m = \frac{|q/p|^2 - |p/q|^2}{|q/p|^2 + |p/q|^2}. \tag{4.43}$$

If one further defines the production asymmetry A_{prod}, which applies to a measurement where the D production flavour is not measured:

$$A_{prod} \equiv \frac{N(D^0) - N(\overline{D}^0)}{N(D^0) + N(\overline{D}^0)}, \tag{4.44}$$

and assumes that R_m is close to unity which allows the parametrisation

$$R_m^{\pm 2} = 1 \pm A_m, \tag{4.45}$$

one can define the following observable mixing quantity

$$\begin{aligned} y_{CP} &= \frac{\hat{\Gamma}(D \to K^+K^-)}{\hat{\Gamma}(D \to K^-\pi^+)} - 1 \\ &= y\cos\phi - x\sin\phi \left(\frac{A_m}{2} + A_{prod} \right), \end{aligned} \tag{4.46}$$

which, in the limit of no $\mathcal{CP}$ violation, is equal to the mixing parameter y. As the LHCb is a single-armed spectrometer, the number of D^0 and $\overline{D}^0$ produced in the acceptance of LHCb are not necessarily equal. An unknown production asymmetry would obscure the extraction of A_m but any significant difference from y still indicates $\mathcal{CP}$ violation as it requires a non-zero value of ϕ.
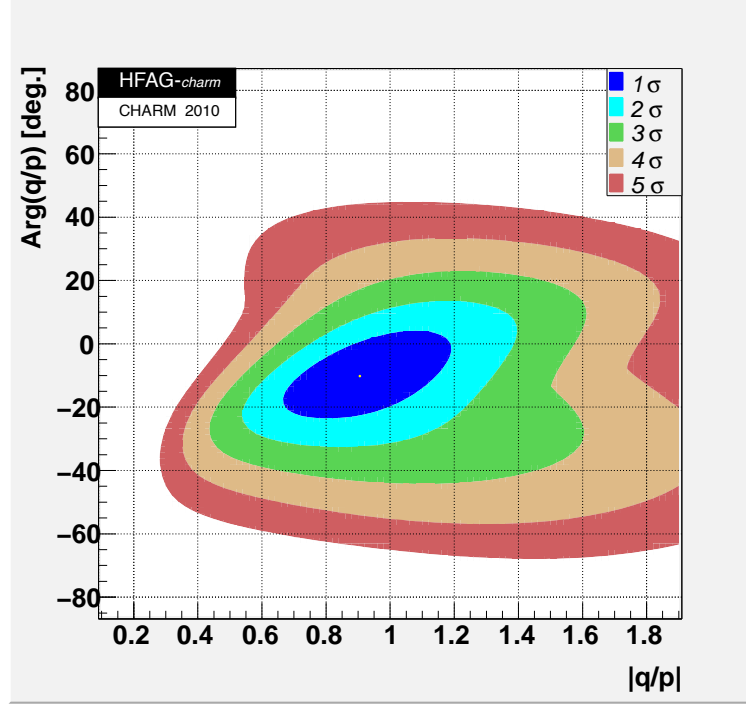
Figure 4.5:   World average values of $\mathcal{CP}$ violation parameter $|q/p|$.

Distinguishing the D flavours at production, i.e. through flavour tagging, one can then define the following related observable $\mathcal{CP}$ violation quantity

$$
\begin{aligned}
A_\Gamma &= \frac{\hat{\Gamma}(D^0 \to K^+K^-) - \hat{\Gamma}(\overline{D}^0 \to K^+K^-)}{\hat{\Gamma}(D^0 \to K^+K^-) + \hat{\Gamma}(\overline{D}^0 \to K^+K^-)} \\
&= \left(\frac{A_m}{2} y \cos\phi - x \sin\phi \right) \frac{1}{1 + y_{CP}} \\
&\approx \frac{A_m}{2} y \cos\phi - x \sin\phi.
\end{aligned}
\tag{4.47}
$$

A_Γ is sensitive to both the $\mathcal{CP}$ violation parameters $|q/p| - 1$ and ϕ, as it is only non-zero if $A_m \neq 0$ or $\phi \neq 0$, i.e. when there is $\mathcal{CP}$ violation.

The world average values of $|q/p|$ and ϕ [49] are

$$
|q/p| = 0.91^{+0.18}_{-0.16},
\tag{4.48}
$$

$$
\phi = (-10.2^{+9.4}_{-8.9})\ \%,
\tag{4.49}
$$

with a contour plot of $|q/p|$ shown in Figure 4.5. Both values are consistent with there being no $\mathcal{CP}$ violation.

A measurement of $\mathcal{CP}$ violation is obtained through the observable A_Γ which has been introduced in Equ. 4.47. It is defined as the asymmetry of the measured lifetimes of $D^0 \to K^+ K^-$ and $\overline{D}^0 \to K^+ K^-$ decays (or the corresponding decays into $\pi^+\pi^-$). This measurement requires tagging the flavour of the D^0 at production by reconstruction of the $D^{*+} \to D^0 \pi^+$ decay chain.

BaBar and BELLE have measured A_Γ together with y_{CP} in their analyses involving tagged D^0 decays. The technique used by both experiments is based on lifetime measurements of the individual modes. Their results are summarised in Tab. 4.1, where the errors quoted are statistical and systematic uncertainties, respectively. Both results are consistent with zero, i.e. with the absence of $\mathcal{CP}$ violation.

Table 4.1: Recent results for A_Γ extracted from $D^0 \to hh$ decays. The errors quoted are statistical and systematic uncertainties, respectively.

Experiment	$A_\Gamma(10^{-3})$
BELLE[62]	$0.1 \pm 3.0 \pm 1.5$
BaBar[63]	$2.6 \pm 3.6 \pm 0.8$

Chapter 5

Measurement of A_Γ in Tagged $D^0 \to K^+K^-$ Decays

5.1 Analysis Overview

This chapter presents a measurement of the D^0 $\mathcal{CP}$ violation parameter A_Γ. The mathematics principles behind the binned ratio method are explained in Section 5.2. The trigger and offline selections are described in Sections 5.4 and 5.5. The various sources of background that are expected to be present in the data after all selection criteria are categorised in Section 5.3. The method of measurement of A_Γ, based on the binned lifetime ratio, is detailed in Section 5.7. This includes the distinction of signal and background events and extraction of the signal yield, and the separation of prompt charm decays from those originating from secondary decays. Sections 5.8 and 5.9 present the cross-checks and final results, and studies of systematic uncertainties, respectively.

The advantages of using the decay chain $D^{*+} \to D^0\pi^+$ (Figure 5.1) are that it provides flavour tagging for the D^0, via the sign of the pion and that the difference in the invariant mass of D^* and D^0, due to very little kinetic energy being available for the lone pion (therefore labelled as "slow pion") in the decay, is a valuable background discriminating variable.
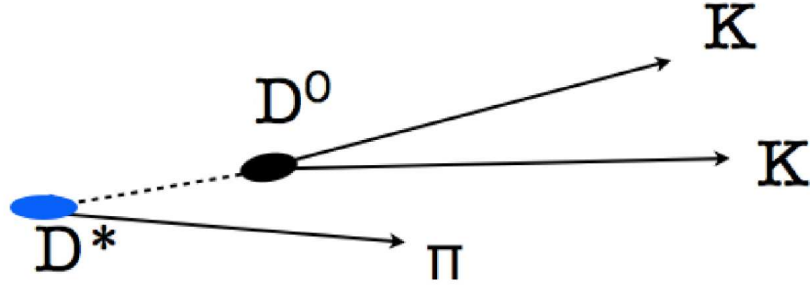
Figure 5.1: The decay chain of $D^{*+} \to D^0(KK)\pi^+$.

The total data sample recorded in 2010 by LHCb corresponds to an integrated luminosity of 37.7 pb^{-1}. Trigger configurations were changed during the 2010 data taking to adapt to the running scenarios from the LHC. The LHC's increase in luminosity was achieved only with a limited number of bunches in the machine, which led to significant pileup different from the $n = 1$ scenario that was envisaged. It was decided that LHCb would record all the luminosity available, and this meant continual changes needed to be implemented into the trigger, in response to changing luminosity and beam configurations of the LHC. For this reason, the physics analysis presented in this thesis spans several trigger configurations. Each group of data taken under different trigger configurations was analysed individually.

5.2   Ratio Fit to Extract A_Γ

The probability density function of D^0 decays to K^+K^-, ignoring detector acceptance and resolution effects, is

$$P_{D^0}(t) = N_{D^0}\frac{1}{\tau_{D^0}}e^{-t/\tau_{D^0}}, \tag{5.1}$$

where N_{D^0} is the total number of D^0 decaying to K^+K^- and τ_{D^0} is the lifetime of D^0 reconstructed in a $\mathcal{CP}$-even eigenstate, such as K^+K^-.

This analysis uses a binned likelihood fit. In the fit it is crucial to choose proper time bins which are significantly smaller than the lifetime of the process under study. The number

of KK signal decays in each proper time bin of interval $(t, t + \Delta t)$ is:

$$
\begin{aligned}
n_{D^0}(t, t + \Delta t) &= \int_t^{t+\Delta t} P_{D^0}(t') dt' \\
&= \frac{N_{D^0}}{\tau_{D^0}} \int_t^{t+\Delta t} e^{-t'/\tau_{D^0}} dt' \\
&= N_{D^0} e^{-t/\tau_{D^0}} \{1 - e^{-\Delta t/\tau_{D^0}}\}.
\end{aligned}
\tag{5.2}
$$

The formalism is identical for $\bar{D}^0$ decays, therefore the ratio between D^0 and $\bar{D}^0$ decays in the same bin is:

$$
\begin{aligned}
R(t, t + \Delta t) &= \frac{n_{D^0}(t, t + \Delta t)}{n_{\bar{D}^0}(t, t + \Delta t)} \\
&= \frac{N_{D^0}}{N_{\bar{D}^0}} \exp\{-(\frac{1}{\tau_{D^0}} - \frac{1}{\tau_{\bar{D}^0}})t\} \frac{\{1 - e^{-\Delta t/\tau_{D^0}}\}}{\{1 - e^{-\Delta t/\tau_{\bar{D}^0}}\}}.
\end{aligned}
\tag{5.3}
$$

As we recall the definition of A_Γ is

$$
A_\Gamma = \frac{\tau_{\bar{D}^0} - \tau_{D^0}}{\tau_{\bar{D}^0} + \tau_{D^0}},
\tag{5.4}
$$

so the equation above can be rewritten as

$$
\begin{aligned}
R(t, t + \Delta t) &= \frac{N_{D^0}}{N_{\bar{D}^0}} \exp\{-A_\Gamma(\frac{1}{\tau_{D^0}} + \frac{1}{\tau_{\bar{D}^0}})t\} \frac{\{1 - e^{-\Delta t/\tau_{D^0}}\}}{\{1 - e^{-\Delta t/\tau_{\bar{D}^0}}\}} \\
&\approx \frac{N_{D^0}}{N_{\bar{D}^0}} \{1 - A_\Gamma(\frac{\tau_{D^0} + \tau_{\bar{D}^0}}{\tau_{D^0}\tau_{\bar{D}^0}})t\} \frac{\{1 - e^{-\Delta t/\tau_{D^0}}\}}{\{1 - e^{-\Delta t/\tau_{\bar{D}^0}}\}} \\
&= \frac{N_{D^0}}{N_{\bar{D}^0}} \{1 - \frac{2A_\Gamma}{\tau_{KK}}t\} \frac{\{1 - e^{-\Delta t/\tau_{D^0}}\}}{\{1 - e^{-\Delta t/\tau_{\bar{D}^0}}\}}
\end{aligned}
\tag{5.5}
$$

where it is assumed that A_Γ is small and that in the last step

$$
\tau_{D^0} \approx \tau_{\bar{D}^0} \approx \tau_{KK} \equiv \frac{\tau_{D^0} + \tau_{\bar{D}^0}}{2}.
\tag{5.6}
$$

If a straight line is fitted to a plot of $R(t, t + \Delta t)$ against t, the gradient a and intercept

b will be equal to

$$a \;=\; -\frac{2N_{D^0}}{N_{\bar{D}^0}\tau_{KK}}\frac{\left\{1 - e^{-\Delta t/\tau_{D^0}}\right\}}{\left\{1 - e^{-\Delta t/\tau_{\bar{D}^0}}\right\}}A_\Gamma, \tag{5.7}$$

$$b \;=\; \frac{N_{D^0}}{N_{\bar{D}^0}}\frac{\left\{1 - e^{-\Delta t/\tau_{D^0}}\right\}}{\left\{1 - e^{-\Delta t/\tau_{\bar{D}^0}}\right\}}. \tag{5.8}$$

As can be seen, the ratio is a linear function of the proper time with a gradient related to A_Γ. The first term in Eqn. 5.7 can be estimated from the constant term in a straight line fit, thus this method does not depend on individual measurements of τ_{D^0} and $\tau_{\bar{D}^0}$. Therefore A_Γ can be determined from the gradient a and intercept b as follows:

$$A_\Gamma = \frac{-a}{2b}\tau_{KK}. \tag{5.9}$$

The value of τ_{KK} is determined using the world-average value of y_{CP}:

$$\tau_{KK} = \frac{\tau_{K\pi}}{1 + y_{CP}} \tag{5.10}$$

where $\tau_{K\pi}$ is the lifetime of the D^0 as measured in the $D^0 \to K\pi$ mode.

The main advantage of using this ratio method is that most acceptance and detector resolution effects factor out in the ratio. A similar method was used in the wrong sign mixing analysis by CDF [64]. Although, in principle, this method is affected by the relative uncertainty on the absolute lifetime measurements involved, using the current world average of $\tau_{K\pi} = 0.4101 \pm 0.0015\,\mathrm{ps}$ [65] results in a negligible relative uncertainty on A_Γ of 0.021%. A measurement of a non-zero value of the gradient in Eqn. 5.8 would be an unambiguous sign of CP violation in D^0 decays.

A toy Monte-Carlo study on A_Γ was performed to understand the optimum binning strategy for this ratio method. In the toy simulation models, the input value for A_Γ is zero and $\tau_{K\pi}$ is taken as the world average of 0.41 ps while τ_{KK} is taken as 0.4074 ps, with the latter calculated assuming $y_{CP} = 0.64\%$. The toy simulation samples were generated

including acceptance and detector resolution effects, both determined from the 2010 LHCb full Monte-Carlo simulation samples. Each toy simulation sample contains $9 \times 10^5 D^0$ and $\overline{D}^0$ events.

Using these parameters the expected value for the gradient of the ratio is zero. The ratio fits were performed with equally time-spaced bins of 3, 10, 30 and 50 between a proper time range of 0 to 2.5 ps. For a straight line fit, the results on the gradient parameter were consistent with input and the mean uncertainties were found to be 9.0×10^{-3} with 3 bins, 8.7×10^{-3} with 10 bins, 8.9×10^{-3} with 30 bins and 8.9×10^{-3} with 50 bins. No significant improvement was found with more bins. This shows that the sensitivities are stable across a wide range of bin choice and the ratio method does not have strong dependence on the choice of binning.

5.3 Background Sources and Discriminating Variables

This section describes the various categories of background that are expected to be present in the analysis. The origin of each type of background is explained together with the discriminating variables to separate them from signal. These variables, that are used both in the trigger and the offline selections, are as follows:

- m, D^0 invariant mass,

- Δm, the mass difference between D^* and D^0. This cut is valuable because very little kinetic energy is available for the slow pion in the D^* decay;

- kinematic quantities: momentum p, and transverse momentum p_T;

- spatial quantities: track χ^2, vertex χ^2, flight distance s, impact parameter IP;

- $\ln \chi^2(IP_{D^0})$, the χ^2 value of the D^0 impact parameter;

- particle ID variables $\mathrm{DLL}_{K\pi}$ and $\mathrm{DLL}_{\pi K}$.
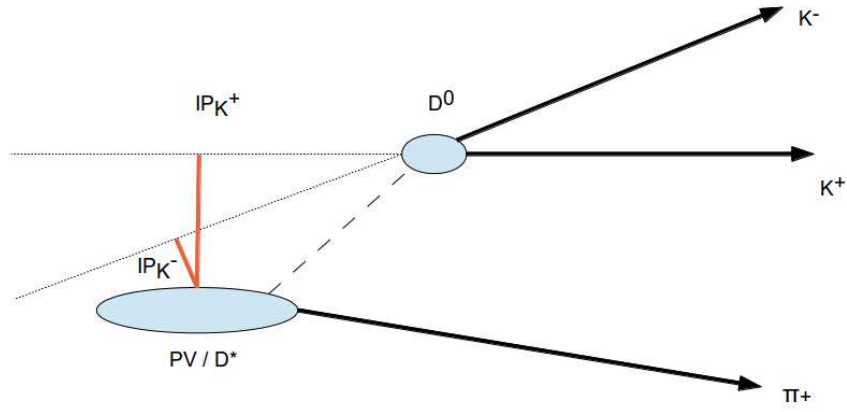
Figure 5.2: The impact parameter (IP) of true D^0 daughters. In the case of D^* decays, the position of the PV is taken as the decay vertex of D^* since the latter decays immediately as it is created, and that the position error on the PV is smaller than that of the D^* decay vertex reconstructed by combining the D^0 and slow pion.

5.3.1 Combinatorial Background

There can be two possible components leading to a near flat distribution in the reconstructed D^0 mass.

The majority of the combinatorial backgrounds results from combinations of random particles produced at the primary interaction vertex. Combinatorial background from the primary vertex is expected to have a short apparent lifetime and to have a falling distribution in D^0 mass. It is suppressed by lifetime-biasing selections such as placing daughter impact parameter IP requirements. As shown in Figure 5.2, true daughters from a D^0 decay tend to have a non-zero IP, which is calculated as the distance of the closest approach of a particle to the primary vertex.

Another source of combinatorial background is from partially-reconstructed B decays. In comparison, the component from B decays have longer effective lifetime and are expected to have a flat or rising distribution in D^0 mass. These decays are suppressed by requirements on the momentum direction of the two-body system as these are partially reconstructed decays which do not necessarily point back to the primary vertex. As shown in Figure 5.3, D^0 mesons from a true D^* decay tend to have a small angle θ, where θ is the angle between
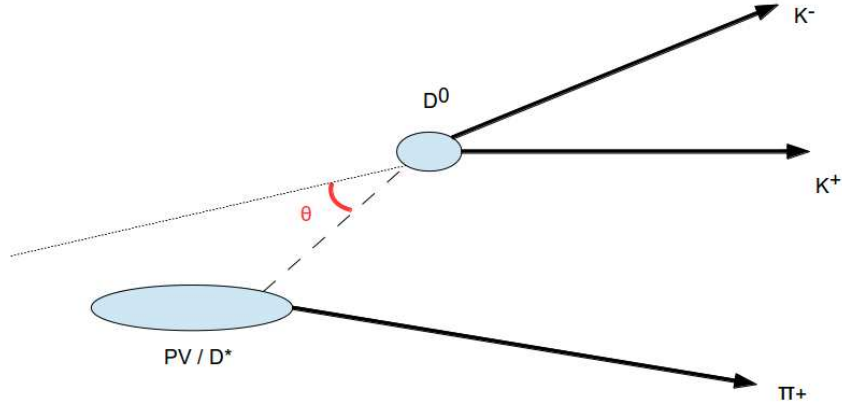
Figure 5.3: The theta angle of true D^0 candidates.

the momentum vector of the D^0 meson and the displacement vector between the primary interaction vertex and the decay vertex of the D^0.

None of the combinatorial background components exhibit a peaking distribution in Δm.

5.3.2   Random Slow Pion Background

Due to the abundance of low energy pions originating from the primary vertex, it is possible for a D^* candidate to be formed by combining a true D^0 meson and a random track that is incorrectly designated as the slow pion.

With the presence of a true D^0, such events have a peaking distribution in the D^0 mass distribution, the same as in signal. However, since this type of events do not correlate to the mass difference between D^* and D^0, they do not peak in Δm. Instead, they have a smoothly increasing shape from a threshold close to the mass of the pion.

This class of background is mainly suppressed by placing a threshold for the slow pion momentum component that is transverse to the beam pipe, p_T, and the χ^2 value of the reconstructed D^* vertices.

5.3.3 D^0 Reconstruction Background

Wrongly reconstructed D^0 candidates can lead to backgrounds in the form of reflections, where the daughters of true two-body D^0 decays are reconstructed under the wrong mass hypothesis (mis-identifications). For example, it is 10 times more likely that a D^0 decays into a Cabibbo favoured $K\pi$ mode than into a singly Cabibbo suppressed KK mode. If the pion in the $D^0 \to K\pi$ decay is mis-identified as a kaon, the decay can be mistaken as a $D^0 \to KK$ candidate at a wrong invariant mass. They may also come in the form of partially reconstructed decays, where in multi-body charm decays, two of the daughters have been identified as D^0 daughters with the others missing in the reconstruction. Mis-identification may also exist for this class of background. For example, a $D^0 \to K^+\pi^-\pi^0$ decay may be selected as a signal candidate if the π^0 is not reconstructed and if the pion is mis-identified as a kaon. This example is particularly dangerous since its invariant mass can lie under the true D^0 invariant mass peak.

Due to the missing particles and momentum, the partially reconstructed decays generally appear in the lower range of the D^0 invariant mass plot. They are thus also referred to as "low mass backgrounds". When these poorly reconstructed D^0 decays are associated with a correct slow pion, they appear as a peaking component in the Δm distribution.

The reflection backgrounds can be rejected by imposing tighter requirements on the PID selection criteria. As in the case for combinatorial background from B decays, partially reconstructed charm decays are expected to be suppressed by requirements on the momentum direction.

5.3.4 Secondary D^0 Background

One of the significant remaining backgrounds after the full offline selection are the secondary D^* decays originating from B hadrons, even though the D^0 candidate is genuine. It is particularly important to discriminate between prompt and secondary candidates because the latter can introduce significant biases in the measured D^0 lifetime, due to the
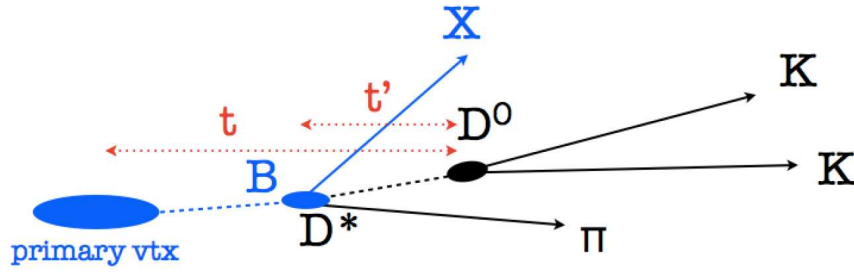
Figure 5.4: The decay chain of a secondary D^0. The measured life time t, calculated using the distance between the D^0 decay vertex and the primary vertex, differ from the true life time t'.

incorrectly measured flight distance, as shown in Figure 5.4, and thus physical parameters that are extracted using the lifetime information. These secondary charm decays cannot be distinguished using the D^0 invariant mass and Δm as they involve genuine D^* decays and thus appear to be identical to the prompt signal, and they form a significant background particularly at higher values of D^0 decay time.

The main difference between prompt and secondary charm decays lies in the direction of flight of the D^0 meson. For prompt decays the D^0 meson always points back to the primary interaction vertex as its point of origin. In a measurement this is only altered by resolution effects. In contrast, D^0 mesons from secondary decays point back to the decay vertex of their mother particle. If the D^0 direction of flight differs from that of its mother particle and the mother flies for a significant distance, the D^0 will not point back to the primary interaction vertex. There are two observables which exploit this difference. One is the impact parameter of the D^0 meson with respect to the primary interaction vertex, IP_D. The second is the angle θ, already introduced in Section 5.3.1.

A more direct way of identifying secondary charm interactions would be by fully reconstructing the decay in which the D^0 is produced. However, there is a vast range of possible decay modes, many involving neutrinos. Daughter particles leaving the acceptance would further reduce the success rate of a direct identification. Therefore, this approach is not practical.

Secondary D^0 decays can never be fully suppressed as they become indistinguishable

from prompt decays if their mother particle decays close to the primary interaction vertex. Therefore, a method has to be devised for statistically separating prompt and secondary D^0 decays.

Due to the non-zero flight distance of the B mesons, one of the most powerful discriminating variables between prompt and secondary candidates is $\ln \chi^2(IP_{D^0})$, the logarithm of the impact parameter χ^2 of the reconstructed D^0 candidate with respect to the primary vertex. Whereas the $\ln \chi^2(IP_{D^0})$ distribution of genuine prompt events is expected to be independent of D^0 decay time (as measured with respect to the primary vertex), the distribution for secondary events is expected to be dependent on the decay time. In general, the values of $\ln \chi^2(IP_{D^0})$ will be larger for longer decay times. The further away a secondary D^0 decays from the primary vertex, the more influence the flight of the B meson has upon its trajectory, therefore it is more likely to be pointing further away from the primary vertex. Figure 5.5 shows the $\ln \chi^2(IP_{D^0})$ distributions of all D^0 candidates, including prompt signal and secondary background. As can be seen the shape of the centre peak remains constant across the whole proper time range, and is dominated by prompt decays. The secondary decays contribute primarily to the "shoulder" peak on the right and its shape shifts towards higher value with increasing proper time.

5.4   Trigger Selection

The selection of D^0 decays in the trigger is inherently more challenging than selecting b-hadron decays, on account of the significantly lower mass and the shorter lifetime of D^0 mesons. Furthermore, there is a direct contradiction between the quantity of charm produced in 7 TeV pp collisions and the requirement to trigger only 2 kHz of events with high efficiency for B meson decays. The LHCb trigger therefore unavoidably biases the final sample of D^0 mesons available for analysis, specifically by using selection criteria (cuts) which bias the lifetime distributions of the D^0 mesons.
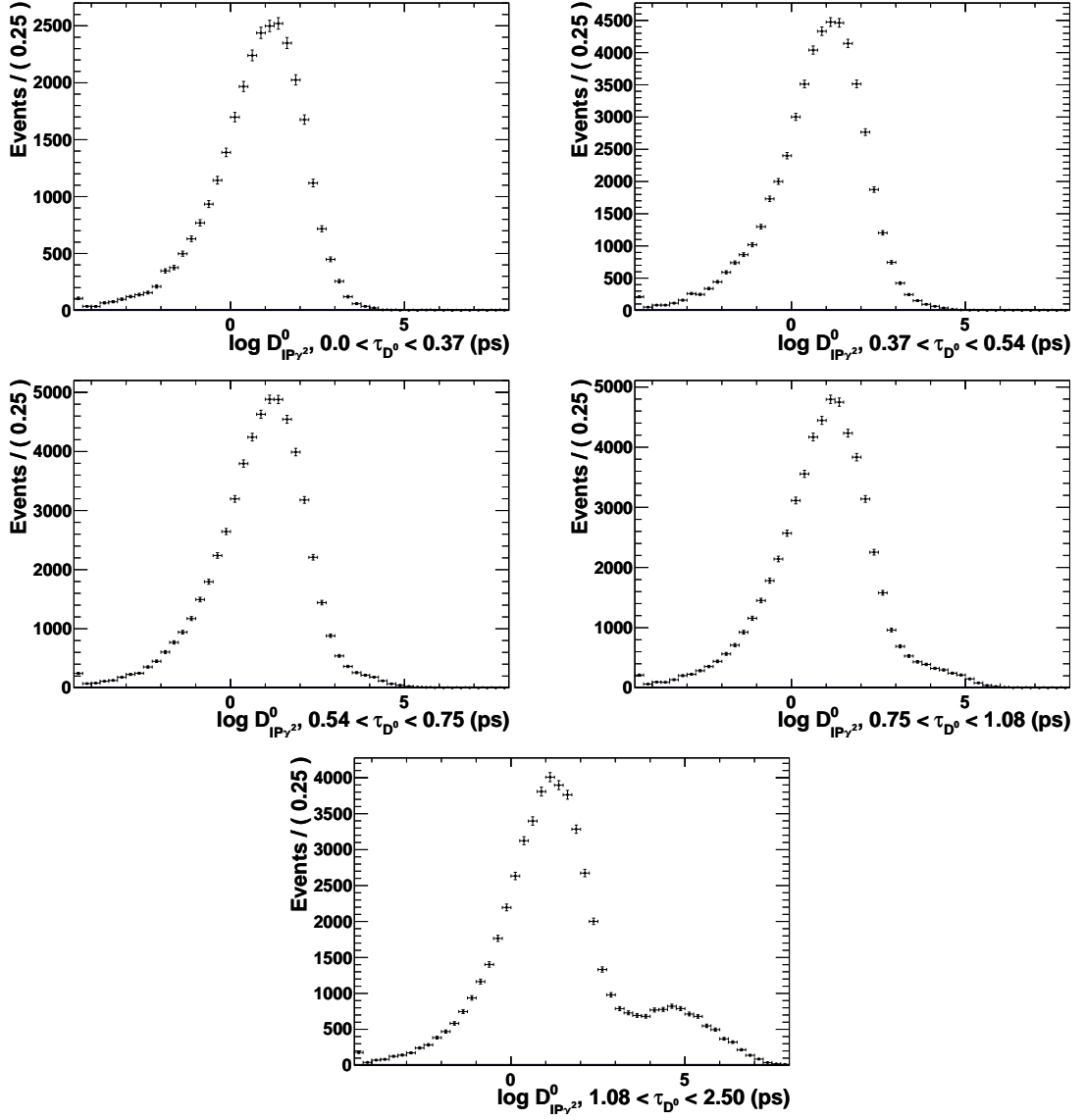
Figure 5.5: $\ln \chi^2(IP_{D^0})$ distributions for $D^0 \to K\pi$ candidates, starting from low proper time at the top-left corner to the high proper time at the bottom. The contribution from the secondary decays becomes increasingly apparent in the shoulder at higher values of $\ln \chi^2(IP_{D^0})$.

5.4.1 Lifetime Biases in HLT1 Trigger

The HLT1 runs on events selected by the L0 trigger. It has information from all of LHCb's sub detectors available. For two-body hadronic D^0 decays, the main selection criteria are:

- Impact parameter: at the start of the HLT1 decision making chain, VELO tracks are selected according to their impact parameter with respect to the primary interactions in the event. Only tracks with a high impact parameter with respect to all primary interactions are kept for further processing. This selection favours events with higher lifetime over those with lower lifetime, thus biasing the propertime distribution of D^0 candidates.

- Minimum number of hits on VELO track: in order to reduce further the number of VELO tracks being considered in the trigger decision, a cut is placed on the minimum number of hits on the VELO track. This potentially is a source of lifetime bias, since a D^0 which flies far transverse to the beam line will have decay tracks which tend to pass through fewer VELO sensors before leaving the VELO.

- Impact parameter χ^2: Once the VELO tracks have been sufficiently reduced in number, they are upgraded to forward tracks, and their momentum and track covariance matrices are established from a Kalman fit to the track. At this point a cut is placed on the χ^2 of the track impact parameter with respect to the primary vertex. This cut has the same proper time biasing nature as the cut on the raw impact parameter.

5.4.2 Lifetime Biases in HLT2 Trigger

The HLT2 D^0 triggers are based on an exclusive selection of two body decay vertices with an invariant mass near the D^0 mass. The following lifetime biasing variables are used to distinguish D^0 events from the background in HLT2:

- Flight distance χ^2 of the D^0: the flight distance χ^2 of the D^0 is directly correlated with the D^0 proper time and the D^0 momentum, and a cut is applied on this quantity in

the exclusive HLT2 D^0 selections.

- Pointing cut: a cut is placed on the angle between the D^0 momentum vector and the displacement vector connecting the D^0 decay vertex to the primary interaction vertex, i.e. θ. This cut potentially introduces a second order proper time bias since shorter lived D^0 meson may have a bigger pointing angle due to resolution effects.

The precise values of the lifetime biasing cuts used in HLT1 and HLT2 can be seen in Table 5.1.

Table 5.1: Cut values for HLT1 and HLT2 triggers used during the final phase the 2010 data taking.

Trigger	Cut Type	Cut
HLT1	Impact parameters	$\lvert IP \rvert > 110 \ \mu\text{m}$
		$IP \ \chi^2 < 34$
	VELO track cuts	Num VELO hits > 9
HLT2	Impact parameters	$IP \ \chi^2 > 2$
	Flight distance	$FD \ \chi^2 > 25$
	Pointing	$\cos\theta > 0.99985$

5.4.3   Impact of HLT2 Lines on the D^0 Mass Distribution

There are some further complications from HLT2 which affect the D^0 sample. The largest part of the available data was acquired using triggers which tightly cut off the events present outside of the D^0 mass window (i.e. in the D^0 mass side-bands). As the side-bands were not available, the data acquired with these triggers alone do not allow for accurate estimation of the amount of combinatorial background under the mass peak.

5.5   Offline Selection

This section describes the selection criteria applied on the events which passed the trigger selections described in the previous section. These offline selections are performed in two

stages - the stripping, which is applied centrally using a looser selection to prepare preselected data sets for the working groups; then a final tighter offline selection applied in the individual analysis. Due to the abundance of charm decays, even the stripping selections have to be designed to achieve a maximal purity, to meet the restrictions of the offline storage. Consequently, only a few additional offline cuts need to be applied after the stripping stage.

5.5.1 Stripping Selections

The stripping selection criteria for flavour tagged D^0 decays are the same for KK, $K\pi$ and $\pi\pi$ decay modes and are independent of the trigger conditions. The selection criteria were first developed with the LHCb Monte-Carlo samples produced in 2009 and then fine-tuned with 2010 LHCb Monte-Carlo samples, where the same selections were applied to a dedicated signal sample as well as the "minimum-bias" background sample, in order to maximise the statistical significance of the selection. A selection threshold is defined at the value where it gives the highest value of $S^2/(S+B)$, where S and B are the yield of signal and background, respectively.

The kaon and pion daughters of the D^0 candidates are required to have momentum above 5 GeV/c, and transverse momentum above 900 MeV/c. The daughter tracks are only accepted if the track fit has a χ^2 per number of degrees of freedom of less than 5. This particular quantity is useful in discriminating backgrounds coming from ghost tracks created by the extra possible track segments in high multiplicity events. A kaon candidate is selected if the logarithm of its kaon hypothesis likelihood with respect to that of the pion is greater than 8 (i.e. $\text{DLL}_{\text{K}\pi} > 8$). Similarly, a pion candidate is required to have $\text{DLL}_{\pi\text{K}}$ > 5, reflecting a lower pion mis-identification rate.

For the D^0 candidates, its vertex fit χ^2 has to be less than 13 with one degree of freedom. Since real D^0 mesons travel before decaying, its flight distance, which is defined as the distance between the primary vertex and D^0 decay vertex, is required to be greater than 0.9 mm. The minimum transverse momentum of the D^0 is 3.3 GeV/c.

The D^{*+} candidates are reconstructed by combining the D^0 and a slow pion candidate, as shown in as shown in Figure 5.1. The slow pion candidates are required to have a transverse momentum greater than 260 MeV/c. To reduce backgrounds coming from the same primary vertex, the vertex fit χ^2 of the D^{*+} is required to be less than 13 per degree of freedom. The minimum transverse momentum of the D^{*+} is 3.6 GeV/c.

The full selection criteria are listed in Table 5.2.

Table 5.2: Tagged stripping selections

Cut Type	Cut Value
Daughter Cuts	$p > 5.0$ GeV/c
	$p_T > 0.9$ GeV/c
	Track χ^2 / nDoF < 5
	kaon DLL$_{K\pi} > 8$
	pion DLL$_{\pi K} > 5$
D^0 Cuts	Vertex χ^2 / nDoF < 13
	$p_T > 3.3$ GeV/c
	Flight distance $s > 0.9$ mm
D^{*+} Cuts	Vertex χ^2 / nDoF < 13
	$p_T > 3.6$ GeV/c
	Slow pion $p_T > 260$ MeV/c

5.5.2 Additional Selections

The stripping lines have been designed to produce samples of high purity, but some additional criteria are applied to remove any residual backgrounds and biases.

The high number of pp interactions per bunch encountered during 2010 data taking results in a number of events with multiple D^* candidates. The additional candidates can be genuine signal events, or in the case when the decay chain is poorly reconstructed, it may happen that the same D^0 candidate is used multiple times if it is associated with different slow pion candidates. The latter background will unavoidably bias the physics parameters to be measured. To remove this bias, only events with a single candidate are considered. This corresponds to a data reduction of about 15%.

The D^0 decay time is required to lie in the range 0 - 2.5 ps. At higher decay times
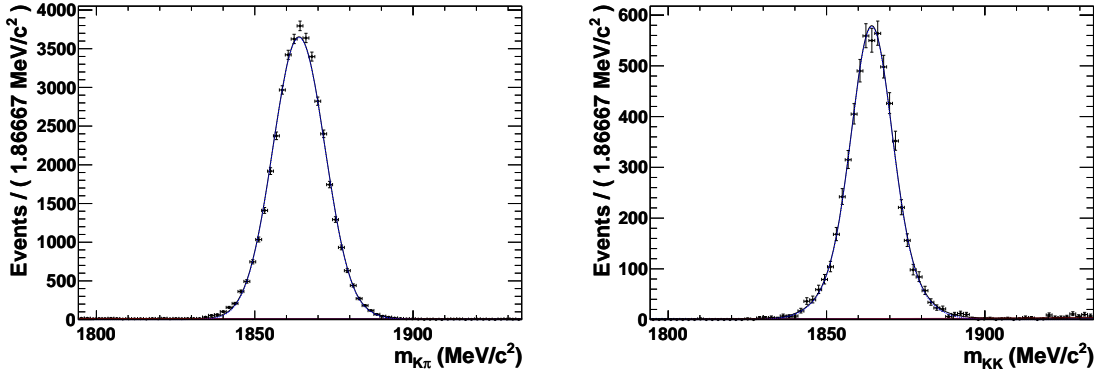
Figure 5.6: D^0 invariant mass distributions of $K\pi$ (left) and KK (right) data samples, with width of 7.28 MeV/c^2 and 7.5 MeV/c^2, respectively.

secondary decays become dominant and little useful information can be gained from using the candidates in this regime.

5.6   Grouping of Data Sample

The total data sample recorded in 2010 by LHCb corresponds to an integrated luminosity of 37.7 pb^{-1}. The distributions of $D^0 \to K\pi$ and $D^0 \to KK$ invariant mass with the full sample size, after trigger and offline selections, are shown in Figure 5.6.

The LHCb trigger evolved a lot throughout 2010, in response to changing LHC luminosity and beam configurations. During the very early data taking period, the HLT2 was not needed due to the low instantaneous luminosity. It gradually came into play when the LHC luminosity increased. In the analysis the data are divided into 3 sub-groups, taking into account the different trigger settings:

- Group 1, early stage data with no HLT2, corresponding to 23.3 pb^{-1};

- Group 2, with HLT2, corresponding to 6.4 pb^{-1};

- Group 3, with HLT2 and with down-scaling on D^0 mass side-band, corresponding to 8.0 pb^{-1}.

Each data sub-group is then further separated into sub-samples of either magnet polarity,

Table 5.3: The number of KK candidates, in each data sub-group. Numbers in parentheses indicate the number of propertime bins in each sub-group.

		Group 1	Group 2	Group 3
Magnet Down	D^0	119365 (10)	0	29308 (3)
	$\overline{D}^0$	122712 (10)	0	30769 (3)
Magnet Up	D^0	73969 (7)	53164 (5)	37140 (3)
	$\overline{D}^0$	77668 (7)	55432 (5)	38300 (3)

Magnet Up or Magnet Down, except for Group 2 where only Magnet Up data are recorded. The motivation for these divisions is to ensure that reconstruction differences between these sub-groups are not obscured by combining them into one large sample. For example, it is conceivable that the reconstructed D^0 mass shape is different before and after changes are made to the detector. The division of the data is shown in Table 5.3.

A measurement of A_Γ is performed for each of the sub-samples. The final value of A_Γ is obtained by taking a weighted mean of the individual measurements.

5.7   Extraction of A_Γ Parameter

5.7.1   Overview

The strategy used in this analysis to determine A_Γ is to partition each sub-group of D^0 decays into bins of proper decay time. In order to calculate A_Γ, the ratio of D^0 to $\overline{D}^0$ signal decays in each bin is determined. Therefore this analysis is based on a binned likelihood fit. Although the statistical precision on A_Γ is in principle reduced by the partitioning of the data into bins, there are certain advantages in this method. The most important feature of the binned strategy is that taking a ratio measurement ensures many of the systematic uncertainties common in both D^0 and $\overline{D}^0$ cancel out. In particular, this removes the lifetime biases introduced by the selection criteria. The main procedures of the binned fit include:

1. Binning of candidates into D^0 proper decay time, as described in Section 5.7.2;

2. Separation of signal candidates from backgrounds using mass fits, as described in Section 5.7.3;

3. Separation of prompt D and secondary D decays from B, as described in Section 5.7.4;

4. In each bin i, plotting the ratio $R_i = N_{D^0,i}/N_{\bar{D}^0,i}$ for A_Γ,

5. Finally, A_Γ is determined from the gradient of the ratio plot, using the formalism presented in Section 5.2.

5.7.2   Binning

The samples of D^0 and $\bar{D}^0$ decays are divided into bins of D^0 decay time such that each bin contains an approximately equal number of candidates. The fits in each time bin are entirely independent of each other. The number of candidates present in each D^0 decay time bin is chosen after considering two principal factors:

1. There must be enough candidates in each bin to permit a stable fit,

2. The width of the time bin must be sufficiently narrow to ensure that any time-varying fit components can be accurately modelled.

The number of time bins for each data sub-group are shown in Table 5.3.

5.7.3   Methods for Background Separation

Yield Extraction for D^0 Decays

The selection of two body D^0 decays is sufficiently pure to allow precise extraction of yields from fits to the reconstructed D^0 invariant mass m alone. A double Gaussian shape is found to be the optimum model for the signal peak. The combinatorial background is modelled as

a first order polynomial. This combined probability density functions (PDF) is thus:

$$f(m) = \sum_{\substack{class \\ =sig,bkg}} f(m|class)P(class), \tag{5.11}$$

with $P(class)$ being the signal and background fractions and

$$f(m|sig) = f_{G1} \cdot Gauss(m, \mu, \sigma_1) + (1 - f_{G1}) \cdot Gauss(m, \mu, \sigma_2), \tag{5.12}$$

and

$$f(m|bkg) = a \cdot m + b. \tag{5.13}$$

Due to the trigger complications discussed in Section 5.4.3, the low side-band statistics does not allow for a good 2-dimensional (Δm vs. m_{D^0}) mass fit. However, the level of combinatorial and D^0 reconstruction background under the signal peak is found to be very low. A one dimensional fit on D^0 mass with requirement that all events fall in the Δm signal box shows a background fraction of 0.019. Therefore, in the fits below the combinatorial background is not entered as a fit component, instead, its existence is taken as a source of systematic uncertainty.

Yield Extraction for Tagged D^0 Decays

To extract the yields of tagged D^0 decays requires in addition a fit to the reconstructed mass difference between D^0 and D^*, Δm. The distributions in Δm and m_{D^0} are assumed to be uncorrelated as there is no physical reason for any correlation.

The PDF for Δm consists of two parts, one describing true D^* decays and one related to randomly associated slow pions, π_s

$$f(\Delta m) = \sum_{\substack{class \\ =sig,bkg}} f(\Delta m|class)P(class). \tag{5.14}$$

The Δm distribution of signal candidates peaks at the PDG difference between the D^* and D^0 masses, i.e. 145.4 MeV/c^2. The peak from true D^* decays is described by three Gaussians. Two have a common mean ($\mu_1 = \mu_2$), however, the third has a slightly higher mean:

$$
\begin{aligned}
f(\Delta m|sig) \quad = \quad & f_{G1} \cdot Gauss(\Delta m, \mu_1, \sigma_1) \\
& + (1 - f_{G1} - f_{G3}) \cdot Gauss(\Delta m, \mu_2, \sigma_2) \\
& + f_{G3} \cdot Gauss(\Delta m, \mu_3, \sigma_3).
\end{aligned} \tag{5.15}
$$

The true D^* decays also cover partially reconstructed or mis-reconstructed D^0 decays as any shift in the reconstructed D^0 mass drops out in the Δm calculation.

The random π_s background PDF in the Δm distribution is given by the special function *RooDstD0BG* PDF defined in the ROOFIT toolkit [66]. This function is defined as

$$
f(\Delta m|bkg) = \left(\frac{\Delta m}{A}\right)^2 \left(1 - e^{-\frac{\Delta m - D}{C}}\right) \; + \; B\left(\frac{\Delta m}{D} - 1\right), \tag{5.16}
$$

where A and B define the slope at high values of Δm, C defines the curvature at low values of Δm and $\Delta m = D$ defines the position where the function is equal to zero.

An example of the Δm fit to data is illustrated in Figure 5.7.

5.7.4 Separation of Prompt and Secondary Charm Decays

An additional method has to be derived to distinguish promptly produced D^0 mesons from those originating in the decay of long-lived particles, as these two classes of decays cannot be distinguished in either the D^0 invariant mass or the Δm signal fraction fit.

It is possible to exploit the fact that IP_{D^0} is zero apart from resolution effects for prompt D decays while it can take larger values for secondary decays. Therefore, the method is to fit the unsigned IP_{D^0} distribution and measure the relative fractions of a narrow distribution
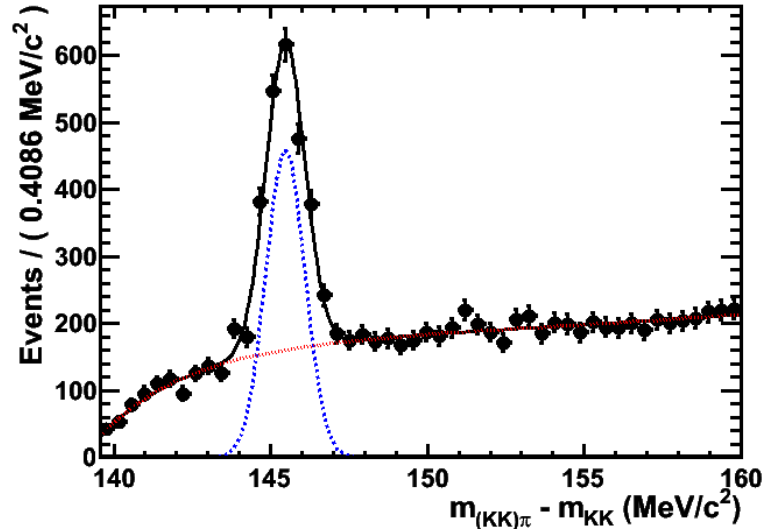
Figure 5.7: A fit to the Δm distribution of a $D^0 \to KK$ data sub-sample. The red dashed line shows the background component, while the blue starred line shows the signal component.

close to zero, representing prompt decays, and a wider distribution representing secondary decays.

An additional challenge arises from the fact that the distributions, particularly that of secondary decays, change with the measured lifetime. The change in the secondary IP_{D^0} distribution is because the longer the measured D lifetime, the larger is the potential contribution due to a B lifetime. In addition, the IP_{D^0} resolution varies as a function of proper time. Therefore, the fits are performed in slices of proper time which coincide with the binning used in the actual measurement.

At LHCb, the χ^2 value of IP_{D^0} is used instead of IP_{D^0}. This makes use of the knowledge of the uncertainty of the IP_{D^0} measurement as described above. Furthermore, it removes any dependence on the time-dependence of the IP_{D^0} resolution.

For prompt D^0 decays the $\chi^2(IP_{D^0})$ distribution does not change with time as the true value is zero at all times and the resolution of $\chi^2(IP_{D^0})$ can be assumed to be independent of the measured lifetime. It is found that the natural logarithm of $\chi^2(IP_{D^0})$ results in distributions which are easier to model. The optimum model for the prompt D^0 in the $\ln \chi^2(IP_{D^0})$ distribution is found to be a composition of two bifurcated Gaussians with common mean, i.e. Gaussians with different widths on each side of the mean, plus a third,
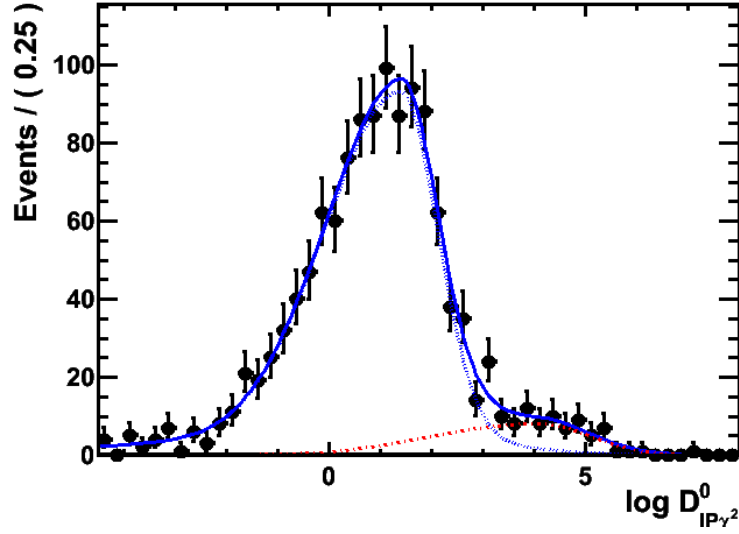
Figure 5.8: A fit to the $\ln \chi^2(IP_{D^0})$ distribution of a $D^0 \rightarrow KK$ data sub-sample. The blue solid line shows the combined distribution from prompt and secondary decays, while the red dashed line shows the secondary component.

symmetric Gaussian. This leads to the PDF

$$
\begin{aligned}
f(\chi^2(IP_{D^0})|t, A, subclass) \quad = \quad & f_{G1} \frac{1}{\sqrt{\pi/2}(\sigma_1^l + \sigma_1^u)} \exp\left\{ -\frac{(\ln \chi^2(IP_{D^0}) - \mu(t))^2}{2(\sigma_1^x)^2} \right\} \\
& + f_{G2} \frac{1}{\sqrt{\pi/2}(\sigma_2^l + \sigma_2^u)} \exp\left\{ -\frac{(\ln \chi^2(IP_{D^0}) - \mu(t))^2}{2(\sigma_2^x)^2} \right\} \quad (5.17) \\
& + (1 - f_{G1} - f_{G2}) \frac{1}{\sqrt{\pi/2}\sigma_3} \exp\left\{ -\frac{(\ln \chi^2(IP_{D^0}) - \mu(t))^2}{2\sigma_3^2} \right\},
\end{aligned}
$$

where $\sigma_i^x = \sigma_i^l (\sigma_i^u)$ if $\ln \chi^2(IP_{D^0}) < \mu(t)$ $(\ln \chi^2(IP_{D^0}) \geq \mu(t))$ for $i = 1, 2$. The parameter f_{G1} (f_{G2}) describes the fraction of the first (second) bifurcated Gaussian.

For secondary D^0 decays the width of the $\ln \chi^2(IP_{D^0})$ distribution is constant and independent of time. The mean, however, increases which reflects the fact that D^0 mesons coming from long-lived decays do not necessarily point back to the primary vertex and that they may point further away the further they fly. The model chosen for the secondary D^0 decays is identical to the one for prompt decays, but with a different values of width σ_i^x and a higher mean value of $\mu(t)$.

Figure 5.8 shows an example of the $\ln \chi^2(IP_{D^0})$ fit on the KK data sample.

5.8   Results

5.8.1   Results for $D \to K\pi$

Since no $\mathcal{CP}$ violation is expected to present between $D^0 \to K^-\pi^+$ and $\overline{D}^0 \to K^-\pi^+$ modes, the $D \to K\pi$ decays can be used as a control channel for validation of the fit model, where the measured pseudo-A_Γ is expected to be consistent with being zero.

The strategy of the binning for the $D^0 \to K^-\pi^+$ is such that the number of candidates in each proper time bin is roughly the same as those in a proper time bin in the $D^0 \to K^-K^+$ analysis. Since the Cabibbo-favoured $K^-\pi^+$ mode has a branching ratio about 10 times larger than K^-K^+, this mean the proper time binning in $D^0 \to K^-\pi^+$ analysis is 10 times finer.

The signal window is defined as $145.433 \pm 2.000\,\mathrm{MeV}/c^2$ in Δm and $1864 \pm 20\,\mathrm{MeV}/c^2$ in m_{D^0}. The random slow pion component is determined in a fit to the Δm distribution while applying the m_D window.

Example Δm fits to a $D^0 \to K^-\pi^+$ sub-group are shown in Figure 5.9. As can be seen the PDF presented in Section 5.7.3 describes the Δm distribution very well across the entire proper time range in the fit.

Example $\ln \chi^2 (IP_{D^0})$ fits to the same data sub-group are shown in Figure 5.10. As can be seen the the shape of the prompt D^0 component remains constant across different proper time bins, while both the yields and the means of secondary D^0 component increase along with the increase of D^0 proper time. Across all parameters there is good agreement between D^0 and $\overline{D}^0$.

The straight line fit is constructed such that $A_\Gamma = \frac{-a}{2b}\tau_{KK}$ is a fit parameter and the fit result return value and uncertainty on A_Γ directly. Table 5.4 shows the results for the pseudo-A_Γ measurement with Cabibbo-favoured decays into the $K^-\pi^+$ final state. This measurement is expected to be in agreement with zero and thus provides a high-precision test of the stability of the method. As can be seen the fit results from all 5 sub-group of

Figure 5.9: Δm fit results for $D^0 \to K^-\pi^+$ candidates (sub-sample Group3+4, Magnet Down). Each plot shows the fit in a propertime slice, starting from low propertime on the top-left corner to the high propertime at the bottom-right corner. The red dashed lines show the slow pion background component.
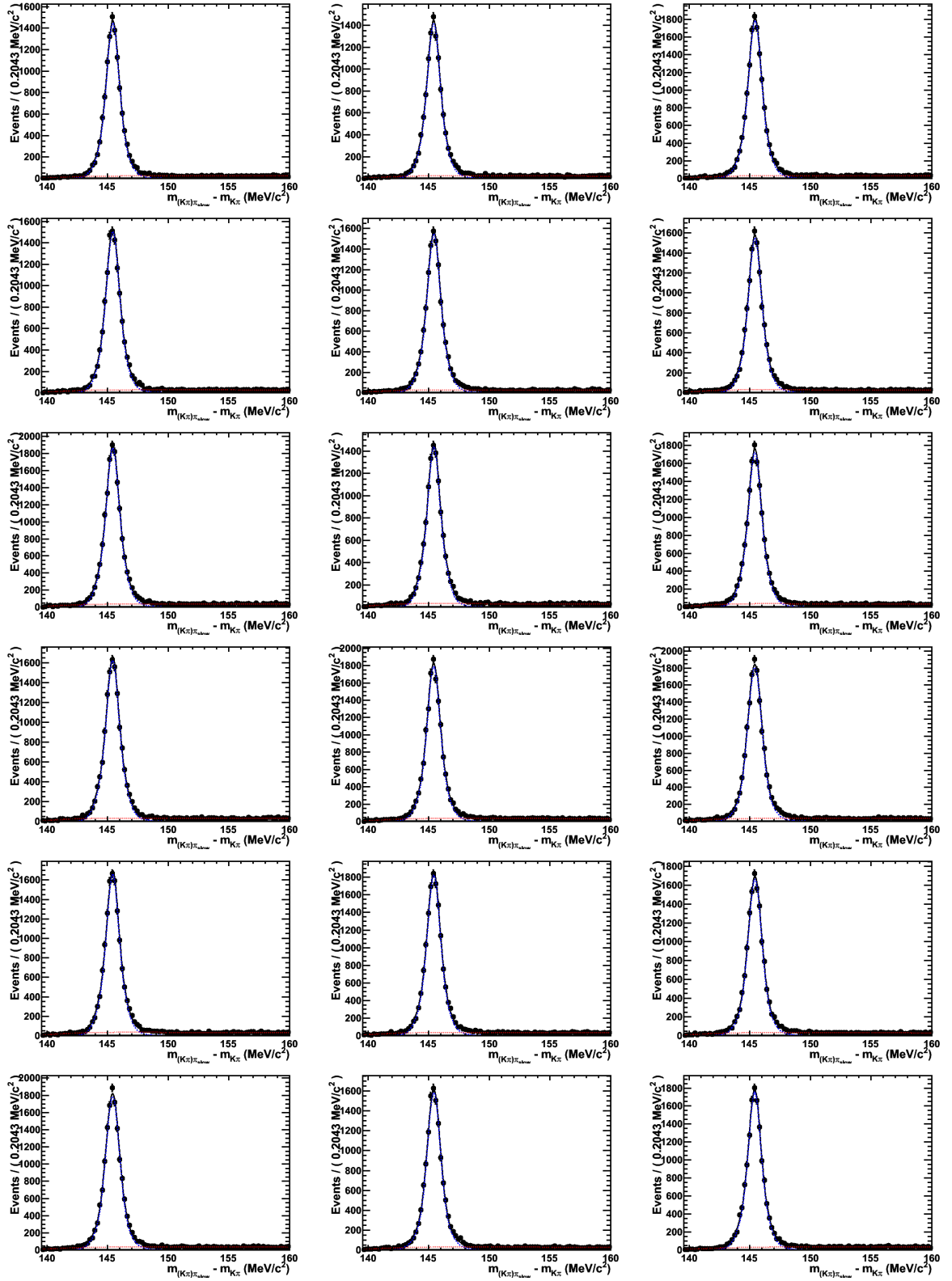
Figure 5.10: $\ln \chi^2(IP_{D^0})$ fit results for $D^0 \to K^-\pi^+$ candidates (sub-sample Group3+4, Magnet Down). Each plot shows the fit in a propertime slice, starting from low propertime on the top-left corner to the high propertime at the left-bottom corner. The red dashed lines show the secondary background component.

Table 5.4: The value of pseudo-A_Γ from straight line fits

Sub-group	Pseudo-A_Γ
1, Mag D	$(-0.12 \pm 0.26)\%$
1, Mag U	$(0.29 \pm 0.34)\%$
2, Mag U	$(0.31 \pm 0.35)\%$
3, Mag D	$(-0.24 \pm 0.47)\%$
3, Mag U	$(-0.01 \pm 0.39)\%$
Weighted Average	$(0.05 \pm 0.16)\%$
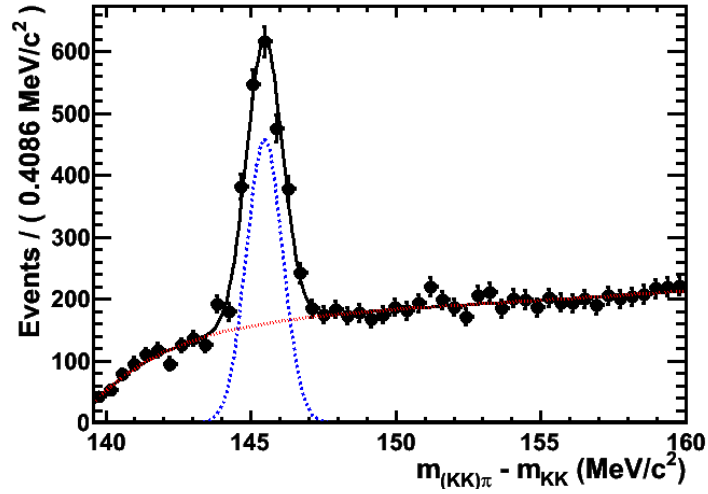
Figure 5.11: Δm fit results for $D^0 \to K^-K^+$ candidates. The red dashed lines show the slow pion background component.

data are consistent with pseudo-A_Γ being zero.

5.8.2   Results for $D \to KK$

The true-A_Γ results based on decays into a pair of oppositely-charged kaons is presented in this section.

As can be seen in Figure 5.11, the random slow pion background level is higher in the K^+K^- mode, compared with the Cabibbo-favoured $K^-\pi^+$ mode. This is as expected, largely due to the latter mode having a branching ratio almost 10 times larger than the former.

Example $\ln \chi^2(IP_{D^0})$ fits to a sub-group of K^+K^- candidates are shown in Figures 5.12. As can be seen the the shape of the prompt D^0 component remains constant across different

Table 5.5: The value of A_Γ from straight line fits to the KK sample

sub-group	A_Γ
1, Mag D	$0.32 \pm 0.77\%$
1, Mag U	$0.89 \pm 1.02\%$
2, Mag U	$0.36 \pm 1.13\%$
3, Mag D	$-0.24 \pm 1.43\%$
3, Mag U	$0.01 \pm 1.15\%$

proper time bins, while both the yields and the means of secondary D^0 component increase along with the increase of D^0 proper time.

The ratio plots from each of the five data sub-group are shown in Figures 5.13. The weighted average intercept on the y axis, b, is 1.02 ± 0.019, with a hint of slightly more D^0 than $\bar{D}^0$ overall. There are two possible reasons for such an asymmetry. The fist is the detection efficiency. As one side of the detector may be more efficient than the other, it can lead to particles of opposite signs having different detection efficiencies. The second reason is that the number of D^{*+} and D^{*-} produced in the acceptance of LHCb may vary. Even with the $D^0 \to K\pi$ decays as control channel, the amount of these asymmetries cannot be estimated. This is because in the $D^0 \to K\pi$ sample there is another source of asymmetry - the nuclear absorption asymmetry for K^+ and K^-, which is significant. It is, however, possible to reduce one type of asymmetry: the detection efficiency effect reverses when the magnet polarity changes, combining data take from both magnet polarity can thus reduce this asymmetry effect.

The values of A_Γ from straight line fits are shown in Table 5.5. As can be seen, the A_Γ value measured using different sets of data are compatible with one another. Taking the weighted average, the combined A_Γ value is
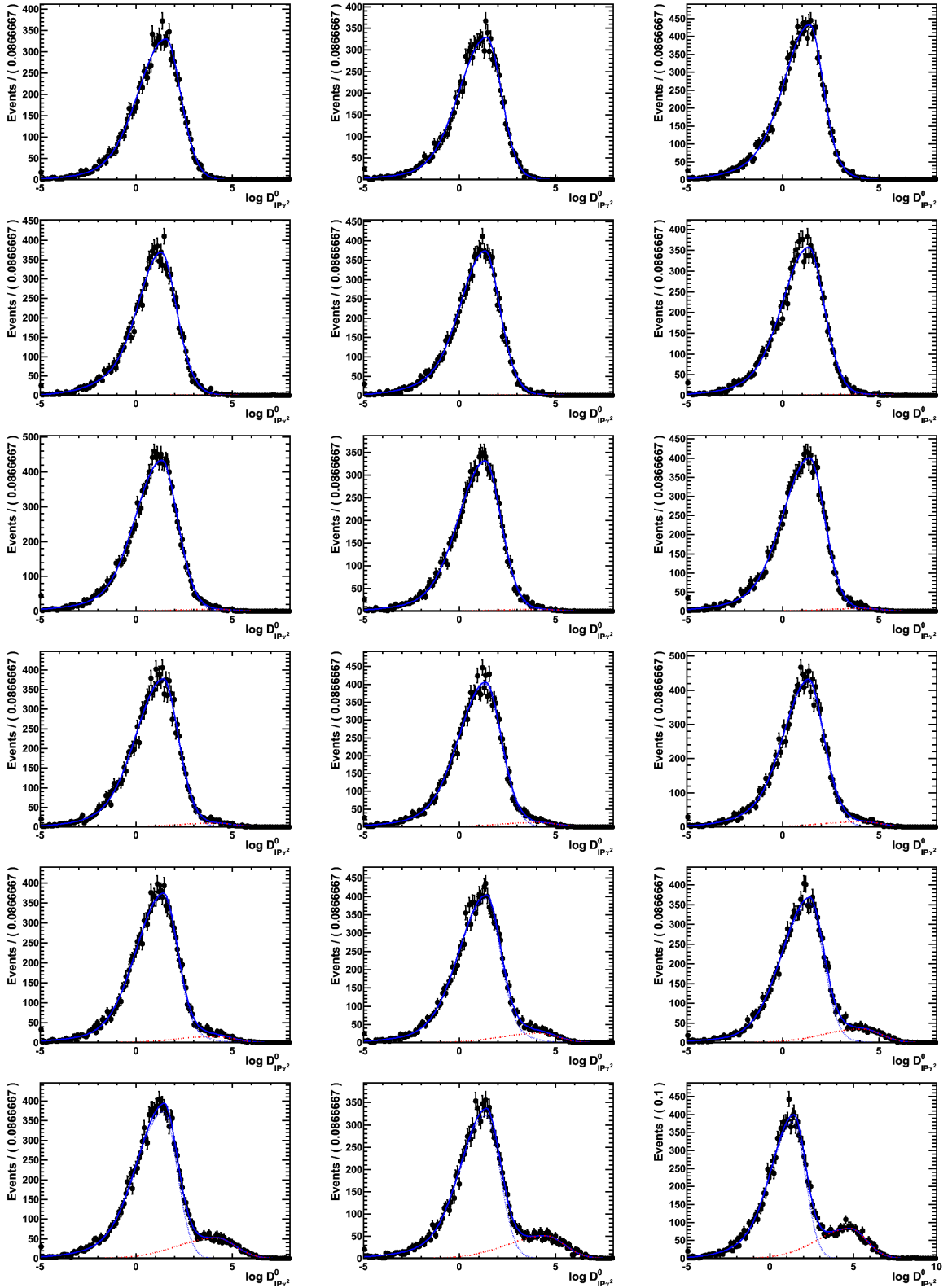
$$A_\Gamma = (0.39 \pm 0.55)\%. \tag{5.18}$$

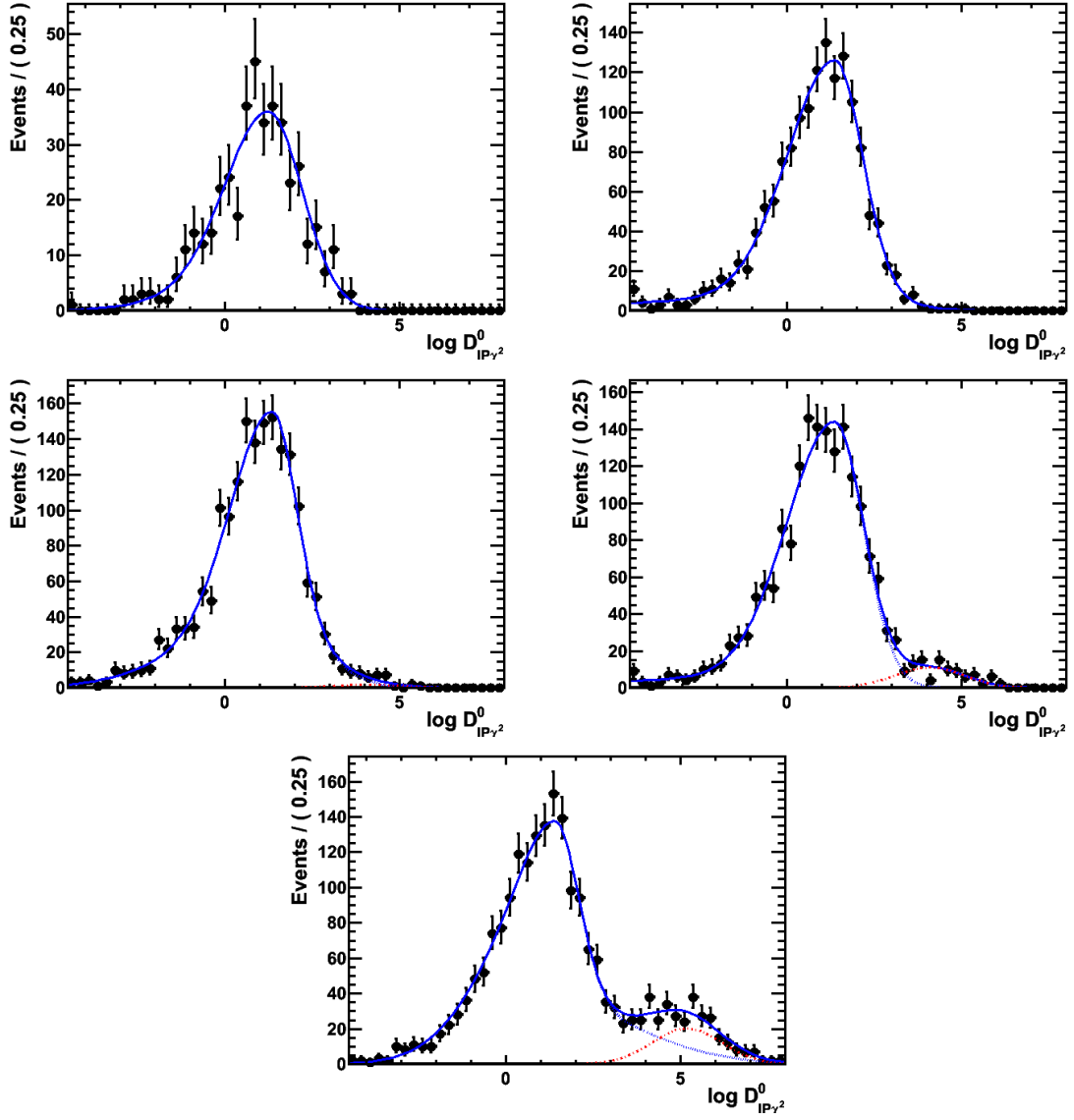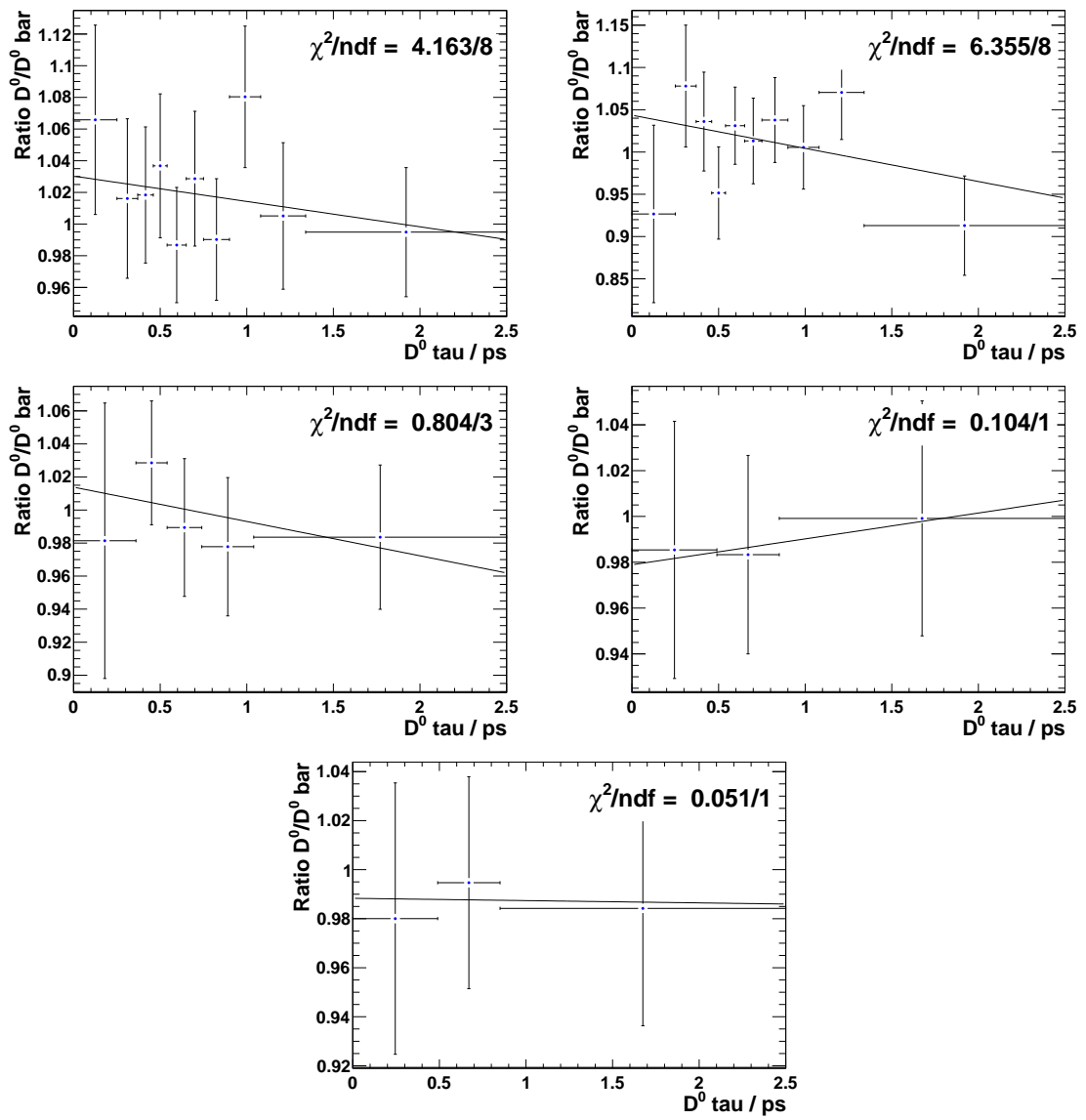Figure 5.12: $\ln \chi^2(IP_{D^0})$ fit results for $D^0 \to KK$ candidates (sub-sample Group2, Magnet Up). Each plot shows the fit in a propertime slice, starting from low propertime on the top-left corner to the high propertime at the bottom. The red dashed lines show the secondary background component.

Figure 5.13: Straight line fits to the ratio of D^0 to $\overline{D}^0$, in each of the five data sub-group.

5.9 Systematic Uncertainties

By measuring the A_Γ parameter with the ratio method, many of the systematic effects cancel due to the similarities in the topologies of the decays. However, there are systematic uncertainties in the measurements that need to be accounted for.

This section describes several means to measure or place an upper limit on an effect which could potentially impact upon the results, in which case an estimated uncertainty is assigned.

5.9.1 Uncertainty from Combinatorial Background

The level of combinatorial and D^0 reconstruction background under the signal peak is found to be very low. A one dimensional fit on D^0 mass with requirement that all events fall in the Δm signal box shows a background fraction of 0.019. This background is not a component in the mass fit, therefore it has to be taken into account as a source of systematic uncertainty. A fraction of 0.019 translates to a maximum uncertainty on A_Γ of 0.08%. There is no reason to believe that this class of background has any time-varying effect on the $\mathcal{CP}$ asymmetry.

5.9.2 Choice of Mass Fit PDFs

The systematic uncertainty associated with the choice of fit PDFs is evaluated using the following procedure. The default fit is run and the central value of each parameter is recorded. The fit is then rerun, fixing the central values of all parameters except those of the relevant PDF under study. The difference between the value of A_Γ obtained using this method and the default value of A_Γ is taken to be the systematic uncertainty in each case.

The signal PDF in the Δm fit, defined in Section 5.7.3, is changed from triple-Gaussian to a double-Gaussian plus a Crystal Ball (CB) distribution, where the CB replaces the Gaussian

with higher mean. The result is

$$A_\Gamma = (0.22 \pm 0.67)\%. \tag{5.19}$$

The systematic uncertainty from the choice of mass fit PDFs is thus taken to be $\pm0.17\%$.

5.9.3   Choice of Secondary Background PDFs

Secondary D^0 mesons from B decays is the major source of background which biases the decay-time reconstruction. As it is the largest background it is potentially the source of the largest systematic uncertainty. To determine the uncertainty from secondary decays in the binned fit, the $\ln \chi^2(IP_{D^0})$ parametrisation is changed. The nominal "2-bifurcated Gaussian + 1 symmetric Gaussian" model is changed to "1-bifurcated Gaussian + 2 symmetric Gaussian", giving a result of

$$A_\Gamma = (0.54 \pm 0.83)\%. \tag{5.20}$$

The systematic uncertainty from the choice of secondary background PDFs is thus taken to be $\pm0.15\%$.

5.9.4   Detection and Production Asymmetries

As one side of the detector may be more efficient than the other, this leads to a detection asymmetry between particles of opposite signs, e.g. K^+, K^-.

The number of D^{*+} and D^{*-} produced in acceptance of LHCb can vary. This effect is referred to as the production asymmetry. The asymmetry $A_P(D^0)$ is defined as

$$A_P(D^0) = \frac{N_P(D^{*+}) - N_P(D^{*-})}{N_P(D^{*+}) + N_P(D^{*-})}, \tag{5.21}$$

Table 5.6: Summary of systematic uncertainties.

Effect	Value (%)
Combinatorial background	0.08
Mass Fit PDFs	0.17
Secondary background PDFs	0.15
D^* production asymmetry	0.03
Total	0.24

and its average value is measured [67] to be

$$A_P = (-1.08 \pm 0.32 \pm 0.12)\%. \tag{5.22}$$

Since the effect of detection asymmetry reverses when the magnet polarity changes, combining data take from both magnet polarity can reduce the asymmetry effects. The dataset used in this analysis contain 11% more magnet Up data compared to magnet Down ones.

These two types of asymmetries affect the value of intercept b in the straight line fit, as A_Γ is a function of b, this accounts for a systematic uncertainty of 0.03% in the sample.

5.9.5   Summary of Systematic Uncertainties

Table 5.6 summarises the systematic uncertainties evaluated as described above. The uncertainties are assumed to be uncorrelated and therefore added in quadrature.

5.10   Cross-Checks

The default binning was described in Section 5.7.2. In order to validate the choice of binning, the analysis was rerun with two different binning strategies, one doubling the number of bins and the other reducing the number of bins by half. With twice the number of bins, the result is $A'_\Gamma = (0.33 \pm 0.53)\%$. Comparing this to the result from using the default binning gives

an uncorrelated statistical uncertainty of 0.14%, while the difference in central values of A_Γ is 0.06%. With half the number of bins, the result is $A_\Gamma'' = (0.24 \pm 0.57)\%$. Comparing this to the result from using the default binning gives an uncorrelated statistical uncertainty of 0.15%, while the difference in central values of A_Γ is 0.15%. This shows the sensitivity does not vary much using different bin choices. The central values of A_Γ from the three binning strategies are all compatible with each others.

5.11   Conclusion

In conclusion, this analysis measures the $\mathcal{CP}$ violation parameter A_Γ in the D^0 meson system, obtained through a binned measurement of the ratio of $D^0 \to KK$ to $\overline{D}^0 \to KK$ decays. The data size corresponds to an integrated luminosity of 37.7 pb^{-1} recorded in 2010 by LHCb. the weighted average of A_Γ, from all sub-groups of data, is

$$A_\Gamma = (0.39 \pm 0.55 \pm 0.24) \ \%, \tag{5.23}$$

where the first error is statistical and the second error is systematic.

The result is compatible with there being no $\mathcal{CP}$ violation.

Chapter 6

Summary and Outlook

This thesis presented the work performed while I was a member of the LHCb collaboration and is comprised of two major components. The first is the design and operation of the magnetic distortion calibration system for the RICH 1 sub-detector, and the algorithms that form part of the calibration package. The second is the analysis on the search for $\mathcal{CP}$ Violation in $D^0 \to K^- K^+$ Decays, through the measurement of parameter A_Γ.

The particle identification provided by the RICH systems is critical to LHCb physics analysis. The RICH 1 HPDs are located at a position where there is upstream fringe field from the LHCb dipole, the presence of which can affect the photo-electron trajectory, leading to distortions in the observed Cherenkov ring image. To ensure high performance, it is necessary to monitor the RICH photon detectors and correct for the distortion. The magnetic distortion calibration systems (MDCS) were designed for such a purpose. The main component of the system is a series of LED boards mounted on a LED bar that traverses the width of the photon funnel.

The principle behind the calibration process is to project a known grid pattern of light directly on the matrix of the HPDs and design an algorithm to reconstruct the pattern. Comparing the patterns recorded with and without magnetic field allows for the analysis of the distortion effects in the reconstruction of the known pattern. It is then possible to parametrise the magnetic distortion correction and apply it in the event reconstruction.

The requirement is that the correction process must obtain a result such that the residual uncertainty due to the magnetic distortion is negligible compared with the intrinsic resolution of an HPD pixel. The MDCS operation software is written with PVSS and a CERN specific framework. It is an integrated part of the LHCb RICH Detector Control.

The RICH MDCS systems, along with the magnetic shieldings, are already providing significant improvements to the Cherenkov angle resolution in the LHC collision data and hence improve the precision of all LHCb physics measurements. The MDCS correction parameters stored in the Conditions Database were applied in the reconstruction of the 2009 LHC collision data which were taken with a negative magnetic field configuration. The result show an improvement of Cherenkov angle resolution from 5.5 mrad to 2.7 mrad, i.e. by a factor of 2. In comparison, the benchmark performance from Monte Carlo simulation is 1.55 mrad. The current resolution is still not yet at the Monte Carlo level, but with more data being collected and the understanding of the detector getting better, there is steady progress in improving the resolution. Regular magnetic calibration runs will continue to be performed during the course of the LHCb data taking, to provide updated parameters for the data reconstruction.

Although the Standard Model is hitherto compatible with all measured $\mathcal{CP}$ violation phenomena in the mixing and decay of heavy flavour hadrons, there are reasons to believe that LHCb could observe effects associated with $\mathcal{CP}$ violation in the decays of B, D mesons which are incompatible with the Standard Model at a previously inaccessible energy scale.

A constraint on $\mathcal{CP}$ violation in the D^0 meson system is obtained through the observable A_Γ. It is defined as the asymmetry of the measured lifetimes of $D^0 \to K^+K^-$ and $\overline{D}^0 \to K^+K^-$ decays (or the corresponding decays into $\pi^+\pi^-$). This measurement requires tagging of the flavour of the D^0 at production by reconstruction of the $D^{*+} \to D^0\pi^+$ decay chain. A_Γ is sensitive to both the $\mathcal{CP}$ violation parameters $|q/p| - 1$ and ϕ, and is only non-zero if there is $\mathcal{CP}$ violation in either D^0 mixing, or in the interference between mixing and decay.

This thesis presents a method for measuring the D^0 $\mathcal{CP}$ violation parameter A_Γ, obtained through a binned measurement the ratio of $D^0 \to KK$ to $\overline{D}^0 \to KK$ decays. The advantage

of the ratio method is that most acceptance and detector resolution effects factor out.

The measurement of the parameter A_Γ is performed with data size corresponds to an integrated luminosity of 37.7 pb^{-1} recorded in 2010 by LHCb. The weighted average of A_Γ, from all sub-groups of data, is

$$A_\Gamma = (0.39 \pm 0.55 \pm 0.24) \ \%, \tag{6.1}$$

where the first error is statistical and the second error is systematic.

The result is compatible with there being no $\mathcal{CP}$ violation, which is compatible with the Standard Model predictions.

It is anticipated that future measurements at LHCb using the data collected in 2011 and 2012 will yield world-leading results. LHCb is therefore close to achieving a measurement of A_Γ that will allow for a sensitive test of the Standard Model.

Bibliography

[1] L. Evans and P. Bryant, "LHC Machine," *Journal of Instrumentation* **3** (2008), no. 08, S08001.

[2] **LHCb** Collaboration, R. Aaij *et al.*, "Measurement of J/ψ production in pp collisions at $\sqrt{s} = 7$ TeV," *The European Physical Journal C* **71** (2011), no. 5, 1–17.

[3] **LHCb** Collaboration, R. Aaij *et al.*, "Prompt charm production in pp collisions at $\sqrt{s} = 7$ TeV," *Nuclear Physics B* **871** (2013), no. 1, 1–20.

[4] **LHCb** Collaboration, "LHCb magnet: Technical Design Report,". CERN-LHCC-2000-007.

[5] **LHCb** Collaboration, "LHCb VELO (VErtex LOcator): Technical Design Report,". CERN-LHCC-2001-011.

[6] **LHCb** Collaboration, "LHCb inner tracker: Technical Design Report,". CERN-LHCC-2002-029.

[7] **LHCb** Collaboration, "LHCb outer tracker: Technical Design Report,". CERN-LHCC-2001-024.

[8] **LHCb** Collaboration, S.Amato *et al.*, "LHCb RICH: Technical Design Report,". LHCb TDR 3.

[9] **LHCb** Collaboration, A. A. Alves *et al.*, "The LHCb Detector at the LHC," *Journal of Instrumentation* **3** (2008), no. 08, S08005.

[10] **LHCb** Collaboration, "LHCb calorimeters: Technical Design Report,". CERN-LHCC-2000-036.

[11] **LHCb** Collaboration, "LHCb muon system: Technical Design Report,". CERN-LHCC-2001-010.

[12] **LHCb** Collaboration, R. A. Nobrega *et al.*, "LHCb Trigger System Technical Design Report,". LHCb TDR 10.

[13] **LHCb** Collaboration, "LHCb online system: Technical Design Report,". CERN-LHCC-2001-040.

[14] A. Daneels and W. Salter, "The LHC experiments Joint COntrols Project, JCOP," *International Conference on Accelerator and Large Experimental Physics Control Systems, Trieste, Italy* (1999).

[15] C. Gaspar and B. Franek, "SMI++ Object-oriented framework for designing control systems for HEP experiments," *Computer Physics Communications* **110** (1998), no. 1-3, 87–90.

[16] **LHCb** Collaboration, "LHCb computing: Technical Design Report,". CERN-LHCC-2005-019.

[17] T. Sjstrand, S. Mrenna, and P. Skands, "PYTHIA 6.4 physics and manual," *Journal of High Energy Physics* (2006), no. 05, 026.

[18] I. Belyaev and others., "Handling of the generation of primary events in Gauss, the LHCb simulation framework," *Nuclear Science Symposium Conference Record* (2010), no. 28, 1155 – 1161.

[19] D. J. Lange, "The EvtGen particle decay simulation package," *Nucl. Instrum. Meth* **462** (2001), no. 12, 152 – 155.

[20] P. Golonka and Z. Was, "PHOTOS Monte Carlo: a precision tool for QED corrections in Z and W decays," *The European Physical Journal C - Particles and Fields* **45** (2006), no. 1, 97–107.

[21] **GEANT4** Collaboration, J. Allison *et al.*, "GEANT4 developments and applications," *Nuclear Science, IEEE Transactions* **53** (2006), no. 1, 270–278.

[22] **LHCb** Collaboration, M. Clemencic, G. Corti, S. Easo, C. R. Jones, S. Miglioranzi, M. Pappagallo, and P. Robbe, "The LHCb simulation application - Gauss: design, evolution and experience," *Journal of Physics: Conference Series* **331** (2011), no. 3, 032023.

[23] T. Gys, "The pixel hybrid photon detectors for the LHCb-RICH project," *Nuclear Instruments and Methods* **A465** (2001) 240–246.

[24] M. Moritz *et al.*, "Performance study of new pixel hybrid photon detector prototypes for the LHCb RICH counters," *IEEE Trans.Nucl.Sci.* **51** (2004) 10601066.

[25] **LHCb** Collaboration, T.Gys, "Electron-optics studies of the LHCb-RICH pixel Hybrid Photon Detector,". LHCb RICH 2007-134.

[26] G. A. Rinella *et al.*, "Pixel hybrid photon detector magnetic distortions characterization and compensation," *Nuclear Science Symposium Conference Record* **2** (2004) 12791283.

[27] G. A. Rinella *et al.*, "Characterisation and compensation of magnetic distortions for the pixel Hybrid Photon Detectors of the LHCb RICH," *Nuclear Instruments and Methods* **A553** (2005) 120124.

[28] **LHCb** Collaboration, M. Patel, M.Losasso, and T.Gys, "Magnetic shielding studies for the LHCb RICH photon detectors," *RICH 2004 Proceedings, Nucl. Instr. and Methods A* ((2004)). CERN-LHCb-PROC-2004-042.

[29] **LHCb** Collaboration, N. Brook *et al.*, "LHCb RICH1 Engineering Design Review Report,". EDMS 493831.

[30] **LHCb** Collaboration, C. Gaspar, "LHCb ECS Integration Guidelines,". EDMS 732486.

[31] **LHCb** Collaboration, P. Duval, "Guide for ECS FSM design in LHCb sub-detectors,". EDMS 655828.

[32] **LHCb** Collaboration, T. Gys, "Electron-optics studies of the LHCb-RICH pixel-Hybrid Photon Detector,". LHCb RICH 2007-134.

[33] F. James and M. Roos, "MINUIT - a system for function minimization and analysis of the parameter errors and correlations," *Comput. Phys. Commun* **10** (1975) 343–367.

[34] R. Brun *et al.*, "ROOT User Guide." Available at `http://root.cern.ch`.

[35] **ATLAS** Collaboration, G. Aad *et al.*, "Observation of a new particle in the search for the Standard Model Higgs boson with the ATLAS detector at the LHC," *Physics Letters B* **716** (2012), no. 1, 1 – 29.

[36] **CMS** Collaboration, S. Chatrchyan, V. Khachatryan, A. Sirunyan, A. Tumasyan, *et al.*, "Observation of a new boson at a mass of 125 GeV with the CMS experiment at the LHC," *Physics Letters B* **716** (2012), no. 1, 30 – 61.

[37] A. Sakharov, "Violation of CP invariance, C asymmetry and baryon asymmetry of the universe," *Pisma Zh.Eksp.Teor.Fiz.* **5** (1967) 32–35.

[38] E. Noether, "Invariante variationsprobleme," *Math-phys. Klasse* (1918) 235257.

[39] T. D. Lee and C. N. Yang, "Question of parity conservation in weak interactions," *Phys. Rev.* **104** (1956) 254–258.

[40] H. Christenson, J. W. Cronin, V. L. Fitch, and R. Turlay, "Evidence for the 2π decay of the K_2^0 meson," *Phys. Rev. Lett* **13** (1964) 138–140.

[41] **BaBar** Collaboration, B. Aubert *et al.*, "Observation of CP violation in the B^0 meson system," *Phys. Rev. Lett* **87** (2001) 091801.

[42] **BELLE** Collaboration, K. Abe *et al.*, "Observation of large CP Violation in the neutral B meson system," *Phys. Rev. Lett* **87** (2001) 091802.

[43] W. Yao *et al.*, "CPT invariance tests in neutral kaon decay," *J. Phys. G* **33** (2006).

[44] C. S. Wu, E. Ambler, R. W. Hayward, D. D. Hoppes, and R. P. Hudson, "Experimental test of parity conservation in beta decay," *Phys. Rev.* **105** (1957) 1413–1415.

[45] R. L. Garwin *et al.*, "Observations of the failure of conservation of parity and charge conjugation in meson decays - the magnetic moment of the free muon," *Phys. Rev.* **105** (1957) 1415–1417.

[46] T. D. Lee, R. Oehme, and C. N. Yang, "Remarks on possible noninvariance under time reversal and charge conjugation," *Phys. Rev.* **106** (1957) 340–345.

[47] L. Landau, "On the conservation laws for weak interactions," *Nuclear Physics* **3** (1957) 127–131.

[48] J. H. Christenson *et al.*, "Evidence for the 2π decay of the K_2^0 meson," *Phys. Rev. Lett.* **13** (1964) 138–140.

[49] **HFAG** Collaboration, D. Asner, B. Golob, and A.Schwartz. Available at `http://www.slac.stanford.edu/xorg/hfag/charm/CHARM10/results_mix+cpv.html`.

[50] **BaBar** Collaboration, B. Aubert *et al.*, "Improved measurement of CP asymmetries in $B^0 \to (c\bar{c})K^{0(*)}$ decays," *Phys. Rev. Lett* **94** (2005) 161803.

[51] **BELLE** Collaboration, K. F. C. et al., "Observation of time-Dependent CP violation in $B^0 \to \eta' K^0$ decays and improved measurements of CP asymmetries in $B^0 \to \varphi K^0, K_S^0 K_S^0 K_S^0$ decays," *Phys. Rev. Lett.* **98** (2007) 031802.

[52] **CDF** Collaboration, T. Aaltonen *et al.*, "Measurement of CP violation in $D^0 \to \pi^+\pi^-$ and $D^0 \to K^+K^-$ decays at CDF," 2012. arXiv:1111.5023.

[53] **LHCb** Collaboration, R. Aaij *et al.*, "First measurement of the CP-violating phase in $B_s^0 \to \phi\phi$ decays," *Phys. Rev. Lett.* **110** (2013) 241802.

[54] P. Ball, "The theory of CP-violation - in as much of a nutshell as will fit on 8 Pages,". arXiv:hep-ph/0406326.

[55] M. Kobayashi and T. Maskawa, "CP-violation in the renormalizable theory of weak interaction," *Progress of Theoretical Physics* **49** (1973), no. 2, 652–657.

[56] L. Chau and W.-Y. Keung, "Comments on the Parametrization of the Kobayashi-Maskawa Matrix," *Phys. Rev. Lett.* **53** (1984) 1802.

[57] L. Wolfenstein, "Parametrization of the Kobayashi-Maskawa Matrix," *Physical Review Letters* **51** (1983) 1945–1947.

[58] K. Nakamura *et al.*, "Review of particle physics," *Journal of Physics G* **37** (2010) 075021.

[59] S. Bianco, F. L. Fabbri, D. Benson, and I. Bigi, "A Cicerone for the physics of Charm," *Rivista del Nuovo Cimento* **26** (2003), no. 7, 1–200.

[60] A. L. Kagan and M. D. Sokoloff, "On indirect CP violation and implications for D^0-$\overline{D}^0$ and B_s^0-$\overline{B}_s^0$ mixing," *Phys. Rev* **D80** (2009) 076008.

[61] **CLEO** Collaboration, D. M. Asner *et al.*, "Determination of the $D^0 \to K^+\pi$ relative strong phase using quantum-correlated measurements in $e^+e \to D^0\bar{D}^0$ at CLEO," *Phys. Rev. D* **78** (2008) 012001.

[62] **BELLE** Collaboration, M. Staric *et al.*, "Evidence for D^0 - $\bar{D}^0$ mixing," *Phys. Rev. Lett.* **98** (2007) 211803.

[63] **Babar** Collaboration, B. Aubert *et al.*, "Measurement of D^0 - $\bar{D}^0$ mixing using the ratio of lifetimes for the decays $D^0 \to K^-\pi^+$, K^-K^+, and $\pi^-\pi^+$," *Phys. Rev. D* **78** (2008) 011105.

[64] **CDF** Collaboration, T. Aaltonen *et al.*, "Evidence for D^0 - $\bar{D}^0$ mixing using the CDF II Detector," *Phys. Rev. Lett.* (2008), no. 121802,.

[65] **Particle Data Group** Collaboration, K. Nakamura *et al.*, "Review of Particle Physics," *Phys. Journal G* **37** (2010), no. 075021,.

[66] W.Verkerke and D. Kirkby, "The RooFit toolkit for data modeling," *Proceedings of Conference for Computing in High-Energy and Nuclear Physics (CHEP 03)* (2003). arXiv:physics/0306116.

[67] **LHCb** Collaboration, A. Carbone and M. Charles, "A search for time-integrated CP Violation in $D^0 \rightarrow hh$ and a measurement of the D^0 production asymmetry,". LHCb-CONF-2011-023.